UIC/WEC JOINT RESEARCH PROJECT ON RAIL DEFECT MANAGEMENT

Correlations Between Rail Defect Growth Data and Engineering Analyses, Part I: Laboratory Tests

David Y. Jeong

U.S. Department of Transportation
Research and Special Programs Administration
Volpe National Transportation Systems Center
Cambridge, Massachusetts 02142

Updated
May 2003

EXECUTIVE SUMMARY

This report is the first in a three-part series describing the technical contributions of the Federal Railroad Administration (FRA) and the Volpe National Transportation Systems Center (Vole Center) to the UIC/WEC (International Union of Railways/World Executive Council) joint research project on Rail Defect Management. Specifically, this report describes engineering analyses that are used to examine the growth of internal rail defects that were tested under laboratory conditions. The second report in this series describes similar engineering analyses that were conducted to examine the growth of internal rail defects tested under field conditions. The third report discusses applications of the rail defect modelling efforts.

The laboratory tests described in this report were conducted by the Research Designs and Standards Organization of India Railways and by Spoornet in South Africa. Moreover, correlations between the laboratory test data and results from the engineering fracture mechanics analyses are presented in this report. In general, the correlations between test and analysis are good.

The titles of the other reports in this series are:

- Correlations Between Rail Defect Growth Data and Engineering Analyses, Part II: Field Tests.

- Analytical Modelling of Rail Defects and Its Applications to Rail Defect Management.

TABLE OF CONTENTS

1. INTRODUCTION

Broken rails, or rail failures, generally occur from fatigue defects that form and grow in the rail steel as a result of cyclic forces caused by the repeated passage of trains over the rails. A broken rail may cause a train to derail.

The primary method for controlling the risk of rail failures is rail testing. Rail testing is the continuous search of rail to find defects, in order to allow time for remedial actions to occur ahead of rail failures. Remedial actions may entail protection or repair of discovered defects, removal of defective rails from track, or a temporary restriction on train speed. The search for surface-breaking rail defects can be performed visually, but the search for internal rail defects must be performed with specialized equipment that uses ultrasonic or magnetic induction technology.

The frequencies at which rail tests are conducted tend to vary from one railroad to another, but are usually based on either time (i.e., a certain number of times per year) or traffic tonnage (e.g., every 20 million gross tons). Railroads have evolved their rail testing schedules empirically, based on decades of field experience. Railroads in the United States generally tend to test rail more frequently than is required by the Code of Federal Regulations.

One of the most important factors in determining rail testing frequencies is the rate at which rail defects can be expected to grow. The growth rate of rail defects is relatively slow at first, but increases as the defect becomes larger. As a rail defect enlarges, the chance of detecting it increases, but the load bearing capacity of the rail reduces which increases the risk of rail failure.

Laboratory and field experiments were performed in the United States during the 1980s to examine the growth rate of rail defects. To complement the experimental work, engineering analyses were conducted to model the growth behavior observed in the experiments. One of the main objectives in conducting the experimental and analytical studies is to determine the slow crack-growth life of rail defects. The term "slow crack-growth life" refers to the time or tonnage during which the rate of crack growth under normal conditions is predictable. Moreover, the slow crack-growth life defines the window of opportunity to find a rail defect. Using a validated engineering model, the slow crack-growth life of rail defects can be estimated for varying track, maintenance, and operational conditions.

More recently, field data are being generated to examine the growth rate behavior of defects in modern rails; i.e., rails with head hardening. These experiments are being conducted by the Transportation Technology Center, Inc. (TTCI) at the Facility for Accelerated Service Testing (FAST) under the sponsorship of the Federal Railroad Administration (FRA) and the Association of American Railroads (AAR).

In addition to the FAST data, rail defect growth data for contemporary non-heat treated rail steels are being generated under laboratory conditions through an international research project sponsored by the World Executive Council (WEC) of the Union Internationale des Chemis de fer (UIC, or International Union of Railways). The task of the WEC is to identify projects of common interest that UIC members either have in progress or wish to begin. In 1997, the UIC/WEC began an international research project on Rail Defect Management.[1] In this context, rail defect management refers to the development and implementation of strategies for controlling the risk of rail failures. In 1999, the FRA and the Volpe National Transportation Systems Center (Volpe Center) were invited to participate in this international effort to provide technical support specifically in fracture mechanics analysis of rail defects.

In support of the UIC/WEC joint research project on Rail Defect Management, the Research Designs and Standards Organization (RDSO) of Indian Railways conducted laboratory experiments to study the growth rate of internal rail defects. The experiments were carried out using a test fixture that was designed and built specifically for the UIC/WEC joint research project. Laboratory and field test data for rail defect growth were also generated by Spoornet in South Africa as part of this project.

The purposes of this document are: (1) to provide a brief summary of the laboratory test data obtained from RDSO and Spoornet, (2) to describe engineering analyses to estimate the growth rate of internal transverse rail defects, and (3) to show comparisons between the laboratory test data and results from the engineering analyses.

This report is the first in a three-part series describing the technical contributions of the Federal Railroad Administration and the Volpe Center to the UIC/WEC joint research project on Rail Defect Management. Similar comparisons between results from field tests (i.e., tests conducted under revenue service-type conditions) and analysis are described and presented in a second, separate report (Jeong, 2002a). Some applications of the modelling work to develop and implement strategies to control the risk of rail failures are described in the third report in this series (Jeong, 2002b).

[1] The organizations participating in the UIC/WEC joint research project on Rail Defect Management are: Association of American Railroads – Transportation Technology Center, China Railways – China Academy of Railway Sciences, East Japan Railways, European Rail Research Institute, India Railways – Research Designs and Standards Organization, Queensland Rail (Australia), Railway Technical Research Institute (Japan), Russian Railway Research Institute, Spoornet (South Africa), and US Department of Transportation – Federal Railroad Administration and Volpe National Transportation Systems Center.

2. SUMMARY OF LABORATORY TESTS

Figure 1 shows a schematic diagram of a rail sample in the RDSO test fixture. The vertical force *V* represents wheel loading, and the axial force *P* represents thermal. In the RDSO tests, the vertical force is varied cyclically to drive the growth of the defect while the axial force is held constant. The frequency of the cyclic loading is 5 Hertz. Measurements of the defect size are taken at 50,000-cycle increments using hand-held ultrasonic equipment.

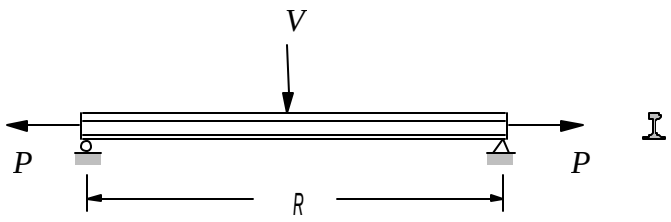

Figure 1. Schematic of vertical and longitudinal loading in RDSO tests.

A total of 19 tests were conducted at the RDSO facility between June 2000 and June 2002 for the UIC/WEC research project. These tests are summarized in Table 1. The table lists the applied loads for each test, as well as the test results in terms of initial and final defect size and the number of cycles to grow the defect from the initial to final size. In most cases, the test was terminated after two million cycles. In five other cases, the test was terminated because the rail fractured during fatigue cycling. In two other cases, the ultrasonic flaw-sizing equipment gave indications of branch cracking. In one other case, a bracket in the test fixture broke after the rail specimen had been fatigued for 350,000 cycles. In this case, only the data collected after repair of the fixture were used in the engineering analyses described here.

The table indicates that five different rail sections were used in the RDSO laboratory tests. The section properties for these different rails are listed in Appendix A. The rail section properties are used in the calculations of rail stresses, which are described in the next section of this report. The two Japanese rail sections (JIS 50 and JIS 60) were assumed to contain squat defects. The 136 RE rail sections were assumed to contain detail fractures. The remaining rail sections (IRS 52 and UIC 60) were assumed to contain tache ovale defects. The fracture mechanics analyses for these defects are also described in the next section.

Table 2 summarizes the laboratory tests conducted by Spoornet. The table lists applied stresses rather than loads. Test results are given in terms of initial and final defect size and the number of cycles to grow the defect from initial to final size. All tests conducted by Spoornet used UIC 60 rail sections.

Table 1. Summary of RDSO Laboratory Tests.

Job Number	*Rail Section*	*Applied Loads*			*Test Results*		
		P (Tonnes)	V_{max} (Tonnes)	V_{min} (Tonnes)	*Flaw Size*		***N*** (cycles)
					Initial (mm)	*Final* (mm)	
TL/2000-10	JIS 60	100	4.5	0.2	6.70	21.44	3.05×10^{6} (a)
TL/2000-11	JIS 60	100	4.5 (b)	0.2	11.29	18.50	3.00×10^{6} (c)
TL/2000-12	JIS 60	100	6.75	0.08	4.10	5.10	2.00×10^{6}
TL/2000-22	IRS 52	79	10.75	0.08	10.26	18.90	1.50×10^{5} (d)
TL/2001-9	IRS 52	61	8.03	0.09	19.00	27.00	1.69×10^{5} (d)
TL/2001-14	UIC 60	63	8.03	0.09	12.30	15.40	2.00×10^{6}
TL/2001-19	IRS 52	67	8.43	0.09	19.49	26.01	1.55×10^{6} (d)
TL/2001-31	JIS 50	87	5.13	0.053	13.26	23.97	1.65×10^{6} (d)
TL/2001-54	JIS 50	80	6.32	0.053	6.12	9.20	2.00×10^{6}
TL/2001-55	JIS 50	60	6.67	0.053	6.12	14.28	2.00×10^{6}
TL/2001-56	JIS 50	64	7.23	0.053	14.36	18.47	2.00×10^{6}
TL/2001-67	JIS 50	62	6.727	0.053	8.20	18.47	2.00×10^{6}
TL/2001-68	136 RE	38	10.05	0.053	2.05	3.08	2.00×10^{6}
TL/2001-103	136 RE	44	10.127	0.053	8.20	16.41	2.00×10^{6}
TL/2001-104	136 RE	42	11.027	0.056	4.10	6.15	2.00×10^{6}
TL/2002-127	UIC 60	52.7	**150.04**	0.051	6.15	10.26	1.65×10^{6} (e)
TL/2002-128	UIC 60	86.27	11.11	0.08	18.5	21.5	8.14×10^{4} (d)
TL/2002-129	UIC 60	54	10.47	0.053	6.15	23.59	2.00×10^{6}
TL/2002-138	UIC 60	57	11.36	0.053	10.26	23.59	2.00×10^{6}

NOTES:

(a) Flaw sizing indicated branch cracking after 2.2 million cycles.

(b) The maximum vertical load was varied during this test, but analysis assumed constant value.

(c) Flaw sizing indicated branch cracking after 1.85 million cycles.

(d) Testing terminated because rail fractured.

(e) This test ran for 2,000,000 cycles, but a bracket in fixture broke after 350,000 cycles. Only data after repair was analyzed.

Table 2. Summary of Spoornet Laboratory Tests.

Defect No.	*Rail Section*	*Applied Stresses*		*Test Results*		
		s_T (MPa) [(a)]	s_B (MPa) [(b)]	*Initial Flaw Size* (mm)	*Final Flaw Size* (mm)	*N* (cycles)
1419	UIC 60	91.94	135	12.5	25.0	2.410×10^5
1432	UIC 60	0	90	13.0	30.0	7.275×10^6
1435	UIC 60	60	90	13.0	28.0	1.825×10^6
1456	UIC 60	90	135	15.0	27.0	3.647×10^5

NOTES:
(a) Magnitude of normal tensile stress representing thermal stress.
(b) Magnitude of maximum tensile bending stress at the rail base.

3. DESCRIPTION OF ENGINEERING ANALYSES

In previous research, an engineering analysis model was developed to estimate the growth of a particular internal rail defect known as a detail fracture (Orringer et al., 1988). This engineering model provides the basis for the present analysis of the RDSO and Spoornet laboratory tests. The previous engineering analysis model was modified to calculate the growth of other internal rail head defects; namely, the squat and the tache ovale defect.

The engineering analyses for the RDSO and Spoornet laboratory test samples are based on the following assumptions:

- The rail behaves as a simply-supported, continuous beam.
- The vertical load is applied at mid-span (i.e., halfway between the supports, see Figure 1).
- The vertical load is applied along the vertical centerline of the rail, which implies no warping or twisting of the rail.
- The axial force creates a uniform normal stress over the rail cross section.
- Internal defects are modelled as transverse flaws in the rail head.
- As the defect enlarges its shape remains constant.
- In each test, the defect is located directly beneath the vertical load.
- The redistribution of rail-head residual stresses as the defect grows is represented by a uniform field that decreases in magnitude with increasing defect size (This assumption is explained further later in this section).

3.1 STRESS ANALYSIS

The stress component corresponding to the opening mode of internal defects in the transverse plane, which is relevant for fatigue crack growth calculations, is the longitudinal component. Moreover, the longitudinal component of stress in the present analysis is assumed to comprise three parts: (1) bending stress due to vertical force, (2) normal stress due to axial force, and (3) residual stress.[2]

The bending stress in the rail at mid-span due to the applied vertical force is

$$s_B = \frac{V\ell V}{4I_{yy}} \tag{1}$$

where V is applied vertical force, ℓ is the span between supports, z is the distance from the neutral axis to the point of interest (i.e., center of the defect), and I_{yy} is the vertical bending inertia of the rail.

[2] Residual stresses are those that remain in an externally unloaded rail.

The normal stress due to the axial force is

$$s_N = \frac{P}{A_R} \tag{2}$$

where P is the axial force and A_R is the cross-sectional area of the entire rail.

Strain gauges were attached to the RDSO rail samples at various locations to calibrate the longitudinal stresses. The measured stresses were generally in good agreement with the theoretical values. Comparisons between the measured and theoretical stresses due to bending are described and shown in Appendix B.

The distribution of residual stresses in the rail head is complex, and varies from one rail to another. A feature observed from measurements is the existence of residual tension in the region where internal defects originate and grow. As a simplifying assumption a uniform residual stress is assumed in place of an actual distribution. Furthermore the uniform residual stress is assumed to decrease in magnitude as the defect enlarges. Figure 2 shows an empirically derived relation between the uniform residual tension and defect size for detail fractures (Clayton and Tang, 1992). The physical interpretation of this relation is that the residual stresses in the rail head are relieved by the creation of fracture surfaces as the defect grows.

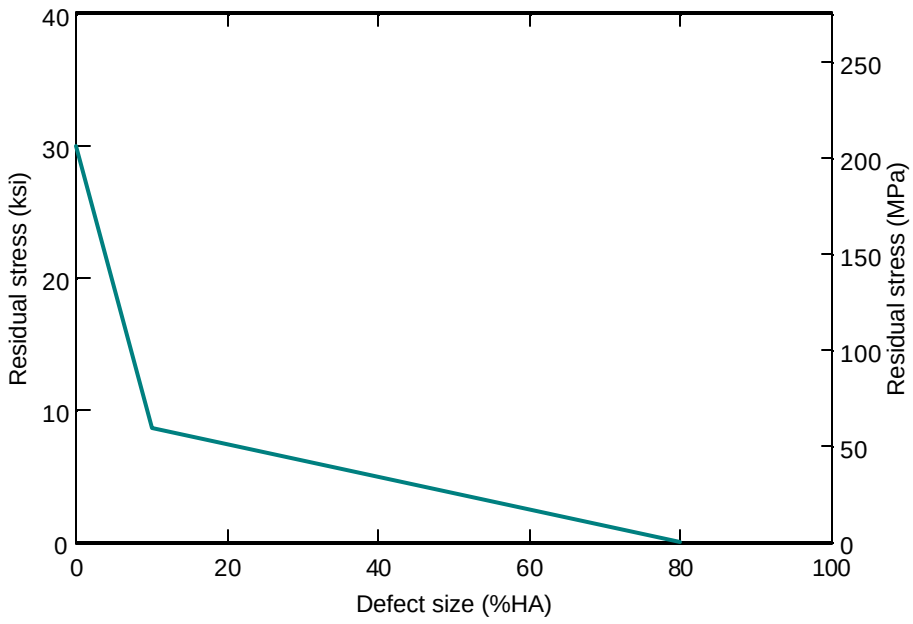

Figure 2. Empirical relation between uniform residual stress and defect size for detail fractures (SF=1).

The empirical relation shown in Figure 2 can be expressed mathematically as:

$$s_R = \begin{cases} SF\left(30 - 2.125A\right) & \text{if } 0\% \le A < 10\% \\ SF\left(10 - 0.125A\right) & \text{if } 10\% \le A \le 80\% \end{cases} \tag{3}$$

where s_R is the longitudinal residual stress in ksi, A is the defect size in percent rail head area (%HA), and SF is referred to as the severity factor. Moreover, the severity factor is a multiplying factor on the residual stress curve shown in Figure 2. Physically the severity factor accounts for the variations in the residual stresses from one rail to another.

The same procedure described above for detail fractures can be repeated for squat defects to determine an empirical relation between uniform residual stress and defect size. The Railway Technical Research Institute (RTRI) performed residual stress measurements on a JIS 50 rail section. Figure 3 shows the distribution of longitudinal residual stresses, as determined from these measurements. The figure shows a common feature observed in other measurements of this type; namely, the presence of a small pocket of residual tension in the interior of the rail head. However, the location of the squat defect relative to the surface is such that the defect propagates through a longitudinal residual stress field that is predominantly compressive.

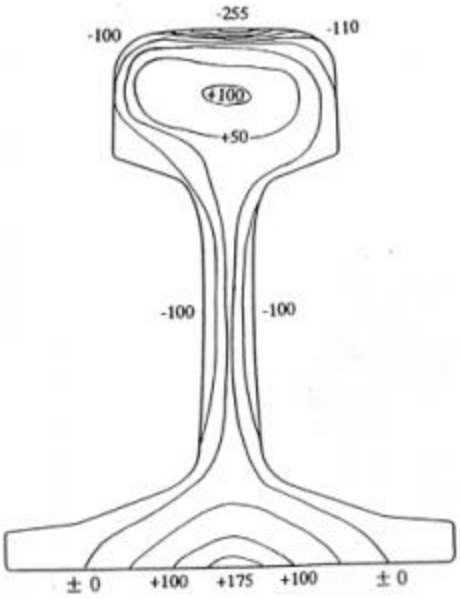

Figure 3. Measured longitudinal residual stress distribution in JIS 50 rail section (Contours in MPa).

Using the stress distribution shown in Figure 3, the numerical procedure that was employed for the detail fracture was applied to derive an empirical relation between uniform longitudinal residual stress and defect size for the squat defect (Figure 4).

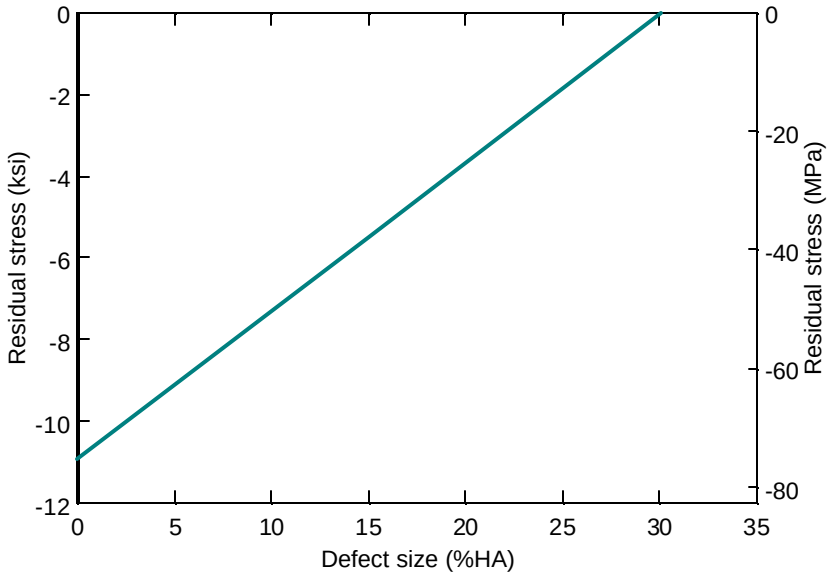

Figure 4. Empirical relation between uniform residual stress and defect size for squats (SF=1).

The mathematical equation for this empirical relation between uniform residual stress and defect size for squats is

$$s_R = SF\left(-10.891 + 0.362A\right) \tag{4}$$

where s_R is the longitudinal residual stress in ksi and A is the size of the squat defect in percent rail head area (%HA). Equation (4) also uses a severity factor, SF which, in this case, is a scaling factor on the residual stress curve shown in Figure 4.

Therefore, the total longitudinal stress in the rail that is used in calculations of defect growth is the superposition of bending, normal, and residual stresses (Figure 5):

$$s = s_B + s_N + s_R \tag{5}$$

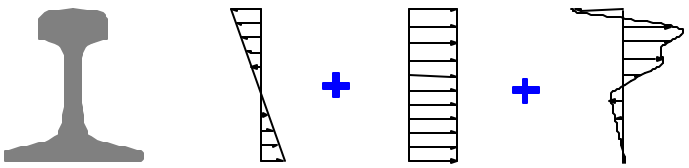

Figure 5. Superposition of bending, normal, and residual stresses.

3.2 FRACTURE MECHANICS ANALYSIS

In engineering fracture mechanics analyses, the state of stress in the vicinity of a crack is characterized by the stress intensity factor or "*K*" formula. Stress intensity factor formulas have been derived for a variety of crack geometries from the classical theory of elasticity (e.g., Sih, 1973). Established stress intensity factors were modified in previous research to develop *K*-formulas for detail fractures (Orringer, et al., 1988), which are used as the basis for the present work. A contribution of the present work is the development of a stress intensity factor formula for squat defects.

3.2.1 Analysis of Detail Fractures and Tache Ovale Defects

A detail fracture is a progressive transverse defect which usually originates from a longitudinal seam or streak near the running surface on the gauge side of the rail head. A tache ovale defect is a progressive transverse type of cracking which usually originates from a manufacturing defect (e.g., hydrogen flakes).[3] Although the origins of detail fractures and tache ovale defects are different, the growth behavior and the fracture mechanics analysis of these two transverse defects are treated similarly.

Figure 6 shows the geometry of a transverse internal rail defect (such as a detail fracture or tache ovale), modelled as an elliptical flaw embedded in the rail head.

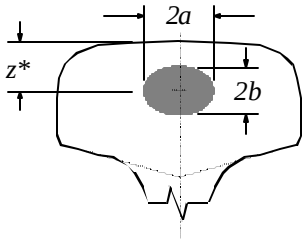

Figure 6. Modelling of internal defect in rail head.

The location of the center of the defect relative to the top of the rail is calculated from an empirical relation derived from previous research

$$z^* = 0.6213 + 1.7580\times10^{-2} A - 1.7933\times10^{-4} A^2 \qquad (6)$$

where A is the defect size in percent rail head area (%HA) and z^* is in inches. A similar equation was also derived in previous research for the location of the center of the defect relative to the vertical centerline of the rail (or y-direction). Since neither lateral bending

[3] This type of transverse cracking may also be referred to as a transverse fissure or a kidney-shaped fatigue crack.

or warping is assumed to occur in the rails tested in the RDSO fixture, the defect center location relative to the rail vertical centerline does not enter into the stress analysis.[4]

The stress intensity factor formula for an elliptical-shaped internal defect in the rail head is assumed to have the following mathematical form:

$$K_I = \frac{2}{p} M_S M_1 s \sqrt{p\, a} \qquad (7)$$

where a is the semi-major axis length of the elliptical crack, M_S is an empirical factor to account for the elliptical shape of the defect, M_1 is an empirical factor to account for the finite dimensions of the rail cross section, and s is the longitudinal stress. The stress intensity factor formula developed for detail fractures includes another empirical factor to account for stress gradients created by the application of lateral loads and off-center vertical loads, but it has been excluded in the present work.

Figure 7 shows that the empirical factor to account for the elliptical shape of the defect varies between 0.9 and 1.0 for aspect ratios between 0.4 and 1.0. The aspect ratio of the elliptical flaw is defined as the ratio of the semi-minor axis length to the semi-major axis length, or *b/a* (see Figure 6). In most of the cases presented in this report, an aspect ratio of 0.7 is assumed, which corresponds to an empirical factor of 0.984. The other cases involve the Spoornet laboratory tests, and assume an aspect ratio of 0.83, corresponding to an empirical factor of 0.996.

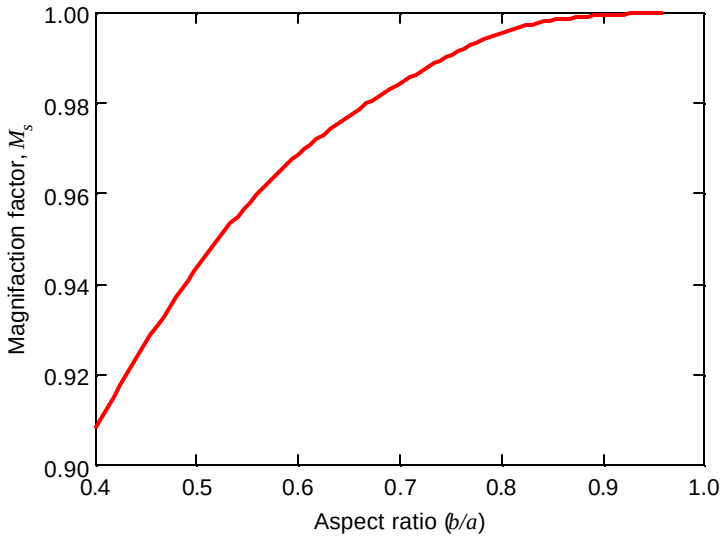

Figure 7. Empirical factor to account for non-circular defect shape.

[4] Lateral and eccentric vertical loads (i.e., vertical loads not applied along the vertical centerline) create warping stresses in rails under service conditions. Lateral bending and warping stress along with head-on-web stresses are taken into account in the analysis of rail defects monitored at FAST.

Figure 8 shows that the empirical factor for finite cross-section increases monotonically as the defect becomes larger. The rise is not only monotonic but it is also rapid.

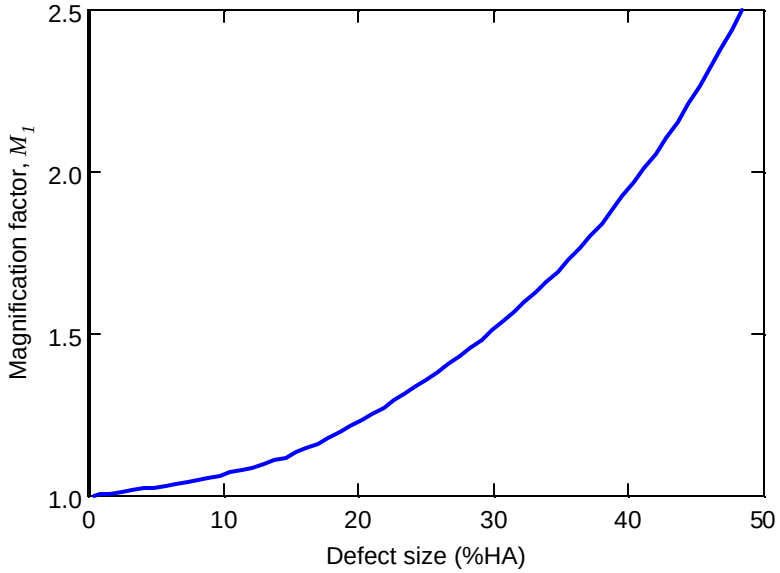

Figure 8. Empirical factor to account for finite boundaries.

3.2.2 Analysis of Squat Defects

A squat defect is a particular form of surface-initiated damage that is caused by rolling contact fatigue. Cracking initially propagates at a shallow angle to the surface. When the shallow angled cracks reach a depth of about 3 to 5 millimeters, they tend to turn toward the transverse plane.

Figure 9 shows an idealization of the squat defect, modelled as a semi-elliptical surface flaw in the transverse plane. In this figure, the aspect ratio is defined as *a/c*.

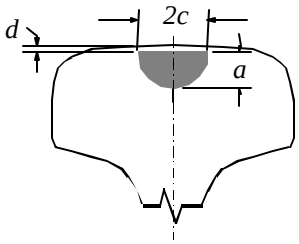

Figure 9. Modelling of squat defect in rail head.

The stress intensity factor formula for a semi-elliptical surface flaw is:

$$K_I = 1.12 M_1 s \frac{\sqrt{p\,a}}{E(k)} \tag{8}$$

where a is the depth of the defect and M_1 is an empirical factor to account for the finite cross section of the rail head. The finite section magnification factor is assumed to be the same as that used in the stress intensity factor formula for detail fractures (Figure 8). Also in equation (8), $E(k)$ is the elliptic integral of the second kind which depends on the aspect ratio of the ellipse:

$$E(k) = \int_0^{\frac{p}{2}} \sqrt{1 - k^2 \sin^2 q}\; dq \tag{9}$$

where

$$k = \sqrt{1 - \left(\frac{a}{c}\right)^2}\,. \tag{10}$$

The factor of 1.12 in equation (8) accounts for the effect of the free surface or the proximity of the flaw to the rail running surface.

RTRI conducted ultrasonic (UT) sizing measurements on five Japanese rails containing squat defects. Table 3 summarizes the results from these UT measurements (refer to Figure 9 for dimensions). Two rails contained two squat defects. The UT measurements suggest that the aspect ratio of the squat defect is approximately 1. In other words, the squat defect may be modelled as a semi-circular surface flaw.

Table 3. Summary of RTRI Ultrasonic Sizing Measurements for JIS 50 Rail Samples.

RTRI No.	*a* (mm)	*2c* (mm)	*d* (mm)	*a/c*
7	20	44	2	0.91
8	11	48	3	0.46
9	20	35	3	1.14
10(a)	12	20	3	1.20
10(b)	19	36	2	1.06
11(a)	20	34	3	1.18
11(b)	12	23	4	1.04
			average	1.00

The stress term in equation (8) is the sum of three parts:

$$s = s_R + s_N + M_G s_B \tag{11}$$

where s_R is the residual stress, s_N is the normal stress due to the axial force, s_B is the bending stress due to the vertical force, and M_G is an empirical factor to account for the stress gradient due to rail bending.

Figure 10 shows the empirical relationship between the stress gradient magnification factor and size of the squat defect. The figure indicates that the stress-gradient effect diminishes as the defect enlarges.

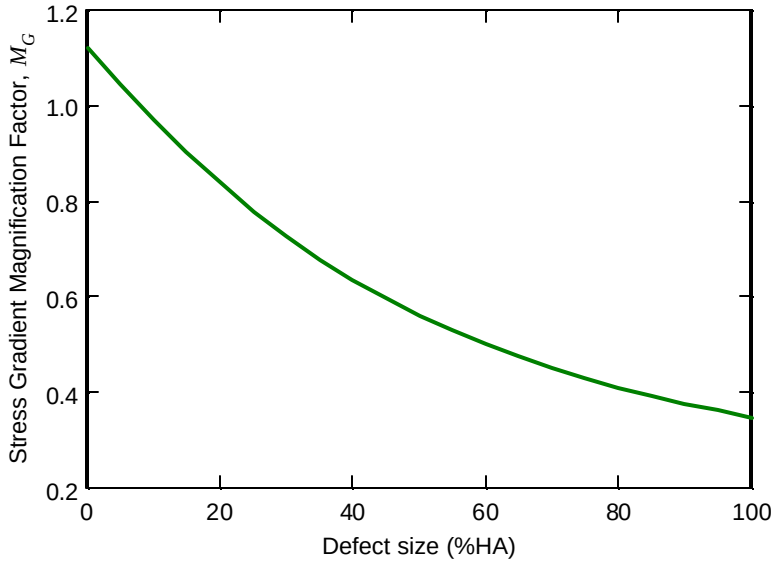

Figure 10. Empirical relation between stress gradient magnification factor and defect size for squats.

3.2.3 Analysis of Crack Growth Rate

The growth of the internal rail defects is calculated using the following equation

$$\frac{da}{dN} = C\frac{\Delta K^p}{(1-R)^q} \tag{12}$$

where a is the characteristic defect size, N is the number of cycles, DK is the stress intensity factor range, and R is the stress ratio (defined as the ratio of minimum to maximum stress in a given stress cycle). Equation (12) also includes material constants C, p, and q that must be determined through laboratory experiments. Table 4 lists the

values of these empirical constants that were derived from experiments conducted for plain carbon rail steel (Scutti et al., 1984).

Table 4. Empirical Constants for Crack Growth Rate Equation.

C (SI units)	C (English units)	p	q
1.74×10^{-13} m-(MPa-m$^{1/2}$)$^{-4}$-cycle^{-1}	1.00×10^{-11} inch-(ksi-inch$^{1/2}$)$^{-4}$-cycle^{-1}	4	1.63

Other fatigue crack growth data for carbon rail steels are available in the open literature. Figure 11 plots the range of fatigue crack growth rates for the standard grade rail steel used throughout Europe and elsewhere (referred to in the figure as UIC 'A'). The figure also shows that equation (12) using the Scutti, et al. data for $R = 0$ is inside the upper and lower limits determined in tests conducted by the Office for Research and Experiments (ORE) of the International Union of Railways (ORE Question D156, 1985).

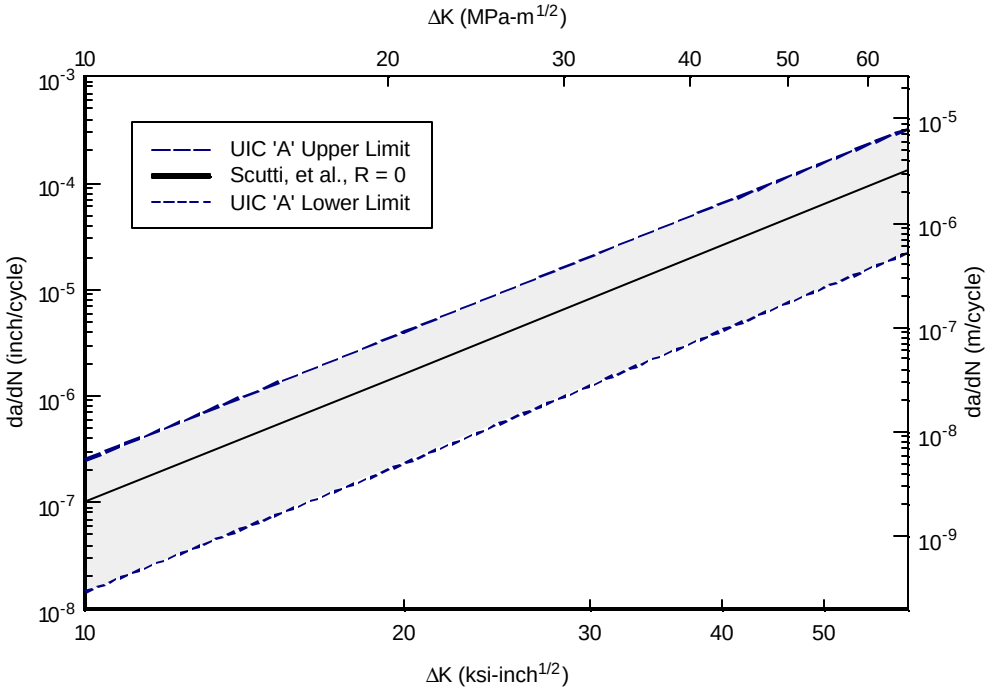

Figure 11. Comparison of fatigue crack growth rates for carbon rail steels.

By treating equation (12) as a separable ordinary differential equation, the number of cycles to grow a crack from an initial size a_i to a larger size a_f can be calculated from

$$N = \frac{1}{C}\int_{a_i}^{a_f} \frac{\left(1-R(a)\right)^q}{\left(G(a)\Delta s\,(a)\sqrt{p\,a}\right)^p} da \tag{13}$$

where *G(a)* refers to a geometry function that depends on the type of defect. In general the stress range Ds, the stress ratio R, and the geometry function depend on the defect size. For the detail fracture and the tache ovale defect, the geometry function is

$$G(a) = \frac{2}{p} M_S\, M_1(a) \tag{14}$$

For the squat defect, the geometry function is

$$G(a) = \frac{2.24}{p} M_1(a) \tag{15}$$

In both equations (14) and (15), M_1 is the empirical factor to account for the finite cross section of the rail head (see Figure 8).

4. CORRELATIONS BETWEEN TEST DATA AND MODEL RESULTS

The size of the internal rail defects was measured in the RDSO fatigue tests using 70-degree ultrasonic probes. The defect growth data collected from these tests were calibrated with the engineering fracture mechanics model by treating the residual stress severity factor as a scaling factor. In some of the cases for squat defects, the calibration involved varying the initial flaw size as well as the residual stress severity factor. In all but three cases, the model correlations used the fatigue crack growth constants listed in Table 4. The other three cases, which involved tache ovale defects in IRS 52 rail sections, used the upper and lower limits of the fatigue crack growth rates shown in Figure 11.

Table 5 lists the residual stress severity factors for which the engineering model provides the best fit for each test conducted at the RDSO facility. The goodness of fit was quantified by Pearson's correlation coefficient[5] which is also listed in the table. The correlation coefficients varied between 0.547 and 1.000. The residual stress severity factors varied between 0.0 and 2.0.

Comparisons between the RDSO test data and results from the engineering analyses are shown in Appendix C for each defect listed in the table.

Table 6 summarizes the correlations between the Spoornet laboratory defect growth data and the results from the engineering analyses. In all of the Spoornet laboratory tests, the rail section was UIC 60 and the defect was assumed to be a tache ovale. The correlation coefficients for these tests, as listed in Table 6, vary between 0.677 and 0.932; the residual stress severity factors vary between 1.0 and 2.0.

Comparisons between the Spoornet test data and results from the engineering analyses are shown in Appendix D.

[5] Pearson's correlation coefficient is a quantitative index of the strength of a linear relationship between two variables. It can take on values between –1 and +1; where –1 is perfect negative correlation, 0 is no correlation, and +1 is perfect positive correlation. A correlation coefficient with no sign at all indicates a positive correlation.

Table 5. Summary of Correlations Between RDSO Test Data and Engineering Model.

Job No.	*Rail Section*	*Defect Type*	*Residual Stress Severity Factor, SF*	*Correlation Coefficient, r*
TL/2000-10	JIS 60	SD	1.5	0.713
TL/2000-11	JIS 60	SD	1.2	0.802
TL/2000-12	JIS 60	SD	0.3	0.547
TL/2000-22	IRS 52	TO	2.0	0.890 [(a)]
TL/2001- 9	IRS 52	TO	1.0	0.913 [(a)]
TL/2001-14	UIC 60	TO	0.6	0.958
TL/2001-19	IRS 52	TO	1.5	0.850 [(b)]
TL/2001-31	JIS 50	SD	1.0	0.984
TL/2001-54	JIS 50	SD	0.3	0.931
TL/2001-55	JIS 50	SD	0.0	0.959
TL/2001-56	JIS 50	SD	1.0	0.870
TL/2001-67	JIS 50	SD	0.3	0.845
TL/2001-68	136 RE	DF	1.8	0.857
TL/2001-103	136 RE	DF	1.4	0.978
TL/2001-104	136 RE	DF	1.0	0.829
TL/2002-127	UIC 60	TO	0.4	0.964
TL/2002-128	UIC 60	TO	1.7	1.000
TL/2002-129	UIC 60	TO	0.4	0.923
TL/2002-138	UIC 60	TO	0.3	0.941

NOTE:
[(a)] Based on UIC-A upper-limit fatigue crack growth data
[(b)] Based on UIC-A lower-limit fatigue crack growth data

Table 6. Summary of Correlations Between Spoornet Test Data and Engineering Model.

Defect No.	*Rail Section*	*Defect Type*	*Residual Stress Severity Factor, SF*	*Correlation Coefficient, r*
1419	UIC 60	TO	2.0	0.903
1432	UIC 60	TO	1.1	0.890
1435	UIC 60	TO	1.0	0.932
1452	UIC 60	TO	1.1	0.677

Defect Types: SD = Squat Defect, TO = Tache Ovale, DF = Detail Fracture

5.0 ADDITIONAL TESTS

Additional tests were conducted by the Research Designs and Standards Organization (RDSO) of India Railways to support the laboratory fatigue test program. Specifically, these additional tests were conducted to determine the chemical composition of various rails, to determine basic mechanical properties of various rail steels, and to measure residual stresses. Residual stress measurements were also conducted by Spoornet.

5.1 CHEMICAL COMPOSITION

Table 7 lists the chemical composition of six different rails. The first two rail samples listed in the table are those from which the fatigue crack growth constants were derived (see Figure 11). The four remaining rail samples are the only rails for which the chemical composition is known among the rails that were tested at the RDSO facility.

Table 7. Chemical Composition of Different Rail Samples.

Sample	*Element (% wt)*					*Ref.*
	C	*Mn*	*P*	*S*	*Si*	
UIC 'A'	0.70	1.11	0.023	0.028	0.09	1
Scutti, et al.	0.89	0.93	0.034	0.022	0.16	2
TL/2000-10	0.82	0.84	0.022	0.022	0.23	3
TL/2000-11	0.83	0.84	0.023	0.020	0.23	3
TL/2000-12	0.70	0.84	0.023	0.024	0.24	3
TL/2000-22	0.77	1.07	0.039	0.026	0.22	3

Ref.
1. ORE Report D156 RP2, September 1985.
2. Scutti, et al., 1984.
3. UIC/WEC Rail Defect Management Project – Metallurgical Testing Memorandum, December 2000.

5.2 MECHANICAL PROPERTIES

Mechanical properties were also determined for the RDSO rail samples that were listed in the previous table. Table 8 lists the Brinell hardness, ultimate tensile strength (UTS), and elongation of these four rail samples. (The first three rails correspond to a JIS 60 section; the last sample is an IRS 52 section.) The Brinell hardness number of the first two rail samples is about 20% lower than that of the last two; the yield strength is roughly 15% lower. It may be reasonable to assume fatigue crack growth properties vary when the mechanical properties are different. Standardized testing to determine the fatigue crack propagation properties of these rails would be useful to confirm such differences.

Table 8. Mechanical Properties of Different Rail Samples.

	Brinell Hardness (BHN)	*Ultimate Tensile Strength (N/mm^2)*	*Elongation (%)*
TL/2000-10	341, 341	1135	13.0
TL/2000-11	321, 331	1122	11.0
TL/2000-12	269, 269	898	16.0
TL/2000-22	269, 269	947	10.9

5.3 RESIDUAL STRESS MEASUREMENTS

Surface residual stress measurements were conducted on 18 of the 19 rail samples tested in the RDSO laboratory fatigue test series. Surface residual stresses were also measured on three other rails of unknown origin by Spoornet. Longitudinal residual stresses around the periphery of the rail were measured using an array of strain gauges and a sectioning technique. The data from these residual stress measurements are given in Appendix E.

A numerical procedure was developed to construct the distribution of the longitudinal residual stresses along the vertical centerline of the rail. This procedure requires the longitudinal residual stress distribution to satisfy static equilibrium since residual stresses are, by definition, self-equilibrating. In other words, the resultant force and moment are stipulated as zero while the residual stress distribution along the vertical centerline of the rail roughly approximates the strain gauge surface measurements. Moreover, residual stresses in the rail head are inferred from measurements taken from the periphery of the entire rail. A description of the numerical procedure and the longitudinal residual stress distributions estimated from applying it are given in Appendix E. The longitudinal residual stress distributions estimated from this numerical procedure have the following common features:

- The shape of the residual stress distribution curve resembles the letter "Z" (see Figure 12). This shape was observed in similar residual stress measurements conducted by the Office for Research and Experiments (ORE Question D156, 1985) and British Rail (Hodgson, 1993).

- The largest magnitude of tension occurs in the rail base, at the bottom of the rail.

- The largest magnitude of compression is in the rail web, generally about two inches from the bottom of the rail.

- The largest magnitude of residual tension generally occurs in the rail head about one inch below the running surface. In one case, the largest residual tension in the head occurred at the top of the rail.

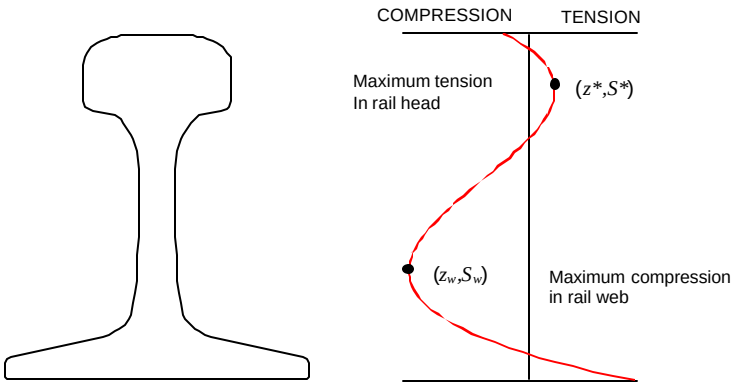

Figure 12. Estimated residual stress distribution.

The engineering fracture mechanics model for defect growth examines rail defects that develop and grow in the rail head. The distribution of residual stresses in the head alone can be complex. Contact stresses can affect internal residual stresses in such a way that the residual stresses on the gauge side of the rail head may be different from those on the field side. Surface measurements may not expose such differences. Therefore, the relationship between residual stresses estimated from strain gauge measurements and the severity factor used in the defect growth analysis is unclear. Additional research is needed to understand the distribution and magnitude of residual stresses, particularly in the rail head.

6.0 DISCUSSION

This report contains laboratory data for growth of internal rail defects obtained from 19 tests conducted by the Research Designs and Standards Organization (RDSO) of India Railways and from four tests conducted by Spoornet in South Africa. The test data were collected for three different types of internal rail defects: detail fractures, tache ovale defects, and squat defects. Engineering fracture mechanics principles were applied to model the growth behavior observed in these two test series. In general, the correlations between the laboratory test data and the results from the engineering analysis are good. For all but two cases (one in the RDSO test series and one in the Spoornet series), Pearson's correlation coefficient is greater than 0.7, indicating a strong association between the test and model results.

In general, the residual stress severity levels appear to be reasonable. The severity factors for the three rails containing detail fractures varied between 1.0 and 1.8. The residual stress severity levels for the rails containing tache ovale defects varied between 0.6 and 2.0; those for squats varied between 0 and 1.5.

The results for the squat defects may require further examination. In four of the eight cases for squat defects, the residual stress severity factor was less than 1. In each of these four cases, the initial defect size was less than 8 mm according to the ultrasonic measurements. In the remaining four cases, the residual stress severity factor was between 1.0 and 1.5. In all but one of those remaining cases, the initial UT flaw size was greater than 10 mm. Figure 13 shows a plot of residual stress severity factor as a function of defect size for squats. The apparent correlation between residual stress severity factor and initial flaw size may suggest an artifact of the model. The assumption that the squat is a transverse defect may be completely valid for relatively large squats. Relatively small squats, however, may be close to the transition between a horizontal crack and a transverse one. For such defects a mixed-mode modelling approach may be more appropriate. Such an approach was not adopted in the present analysis, but may be explored in future work. Moreover, the analyses of squat defects presented in this report are considered preliminary.

Additional tests for chemical composition and mechanical properties should be conducted on the remaining rail samples that were tested at the RDSO facility, for the sake of completeness.

Additional work is needed to complement the laboratory testing and analytical modelling work that has been conducted up to this point. For example, defect sizes were measured in the RDSO tests with hand-held ultrasonic equipment. In two tests, the ultrasonic flaw sizing gave indications of branch cracking, which needs to be confirmed. A confirmation of the actual defect sizes in comparison with the measured defect sizes would be useful Confirmation of the location of the defect in the rail head, the defect type, and growth pattern would also be useful to validate the model. For example, Figure 14 is a photograph of a fractured rail end test number TL/2001-31. In this particular test, fatigue

cycling grew the defect to the point of failure. Moreover, photograph clearly shows that the defect is oriented in the transverse plane. The correlation between the growth rate test data and model results for this case is one of the highest listed in Table 5.

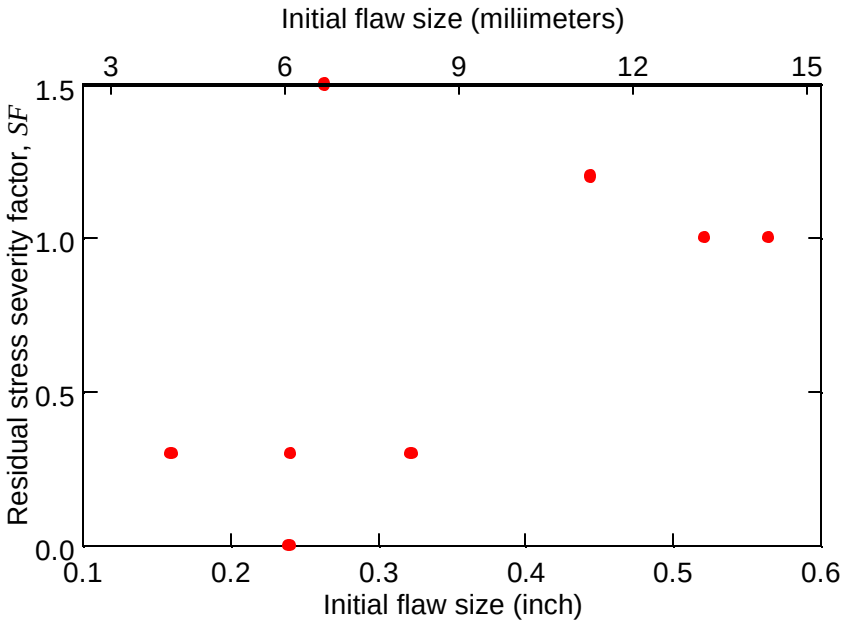

Figure 13. Correlation between residual stress severity factor and initial UT flaw size for squats.

Figure 14. Photograph of broken rail from RDSO Job No. TL/2001-31.

REFERENCES

Clayton, P., and Y.H. Tang, 1992: "Detail fracture growth in curved track at the Facility for Accelerated Service Testing," *Residual Stresses in Rails, Vol. 1,* Kluwer Academic Publishers, The Netherlands, 37-56.

Hodgson, W.H., 1993: "Residual stresses in rail," *Rail Quality and Maintenance for Modern Railway Operation*, Kluwer Academic Publishers, The Netherlands, 61-73.

Jeong, D.Y., 2002a: "Correlations Between Rail Defect Growth Data and Engineering Analyses, Part II: Field Tests," Volpe Center Technical Report for the UIC/WEC Joint Research Project on Rail Defect Management.

Jeong, D.Y., 2002b: "Analytical Modelling of Rail Defects and Its Applications to Rail Defect Management," Volpe Center Technical Report for the UIC/WEC Joint Research Project on Rail Defect Management.

ORE Question D156, "Possibilities of improving the service characteristics of rails by metallurgical means," Report Number 2, Tests on used rails that failed in the track due to brittle fracture, Utrecht, September 1985.

Orringer, O., Y.H. Tang, J.E. Gordon, D.Y. Jeong, J.M. Morris, and A.B. Perlman, 1988: "Crack Propagation Life of Detail Fractures in Rails," Final Report, DOT/FRA/ORD-88/13.

Sih. G.C., 1973: *Handbook of Stress Intensity Factors,* Institute of Fracture and Solid Mechanics, Lehigh University, Bethlehem, PA.

Scutti, J.J., R.M. Pelloux, and R. Fuquen-Moleno, 1984: "Fatigue behavior of a rail steel," *Fatigue & Fracture of Engineering Materials & Structures 7*, 121-135.

APPENDIX A. RAIL SECTION PROPERTIES

Table A.1. Section Properties for RDSO Rail Samples

	JIS 50	IRS 52	UIC 60	JIS 60	136RE
I_{yy}	1950 cm^4 (46.8 in^4)	2158 cm^4 (51.8 in^4)	3055 cm^4 (73.4 in^4)	3083 cm^4 (74.1 in^4)	3950 cm^4 (94.9 in^4)
A_R	64.2 cm^2 (9.95 in^2)	66.15 cm^2 (10.25 in^2)	76.86 cm^2 (11.91 in^2)	77.44 cm^2 (12.0 in^2)	86.13 cm^2 (13.35 in^2)
A_H*	26.65 cm^2 (4.13 in^2)	28.82 cm^2 (4.47 in^2)	30.92 cm^2 (4.79 in^2)	27.95 cm^2 (4.33 in^2)	31.35 cm^2 (4.86 in^2)
h_{tot}	15.3 cm (6.024 in)	15.6 cm (6.142 in)	17.2 cm (6.772 in)	17.4 cm (6.850 in)	18.6 cm (7.313 in)
h_N	7.60 cm (2.99 in)	7.56 cm (2.976 in)	8.10 cm (3.189 in)	7.78 cm (3.063 in)	8.51 cm (3.351 in)

NOTE
* The rail head cross-sectional area was calculated from rail drawings for the JIS 50, IRS 52, UIC 60, and JIS 60 rail sections.

I_{yy} = vertical bending inertia for the entire rail
A_R = cross-sectional area of entire rail
A_H = cross-sectional area of rail head only
h_{tot} = distance between bottom and top of rail
h_N = distance between bottom of rail and neutral axis of entire rail

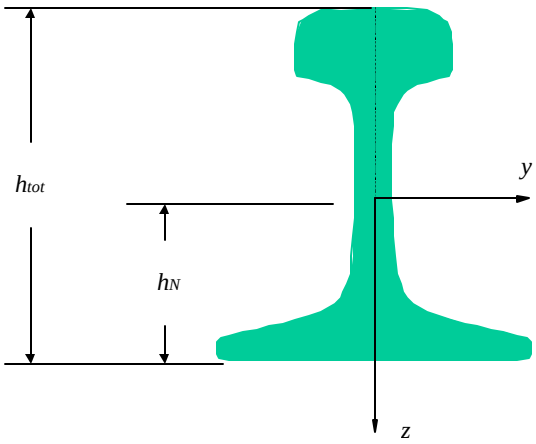

Figure A.1 Rail dimensions.

APPENDIX B. CALIBRATION OF RAIL BENDING STRESS IN RDSO TESTS

Each rail sample that was tested in the RDSO fixture was instrumented with seven strain gauges. The locations of these gauges are shown in Figure B.1. The longitudinal stresses from the applied vertical and axial forces were measured. The measured longitudinal stresses due to axial loads were generally in good agreement with the theoretical values. The normal longitudinal stresses (i.e., longitudinal stresses due to axial force) were calculated using equation (2) in Section 3.1.

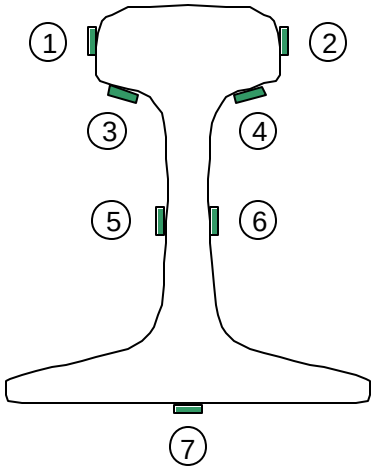

Figure B-1. Strain gauge locations in RDSO rail bending stress measurements.

The longitudinal bending stresses are calculated using equation (1) in Section 3.1. In the present work, the theoretical bending stresses are calibrated to those determined from the strain gauge measurements by treating the distance between supports as a scaling factor. Also, the value for a brand new or unworn rail is assumed for the vertical bending inertia (as listed in Appendix A). The effective distance between supports is determined by finding the value of R that gives the best-fit between the theoretical and measured bending stresses. A least squares regression is used as a criterion for the best fit.

This appendix shows the results of the correlations between the measured stresses (actually average normalized stresses) and the theoretical values based on the best-fit criterion.

Rail Section: JIS 60

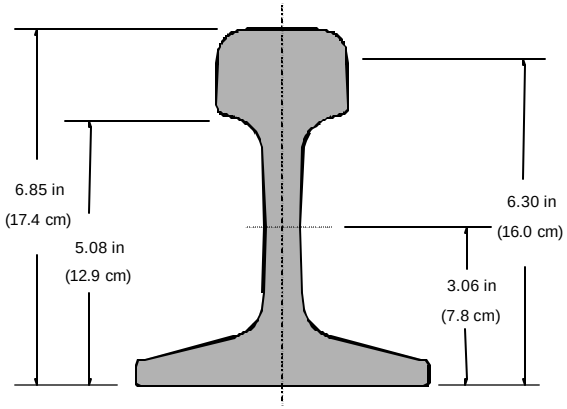

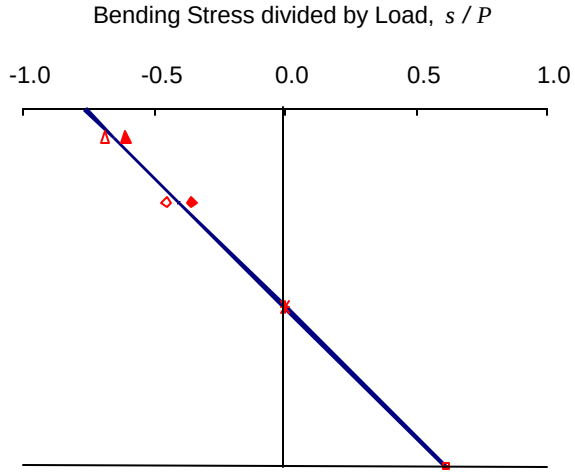

Effective rail length: 59.5 in (151.1 cm)

Correlation coefficient: **0.99668**

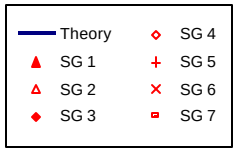

Figure B-2. Vertical bending stress calibration for TL/2000-10.

Rail Section: JIS 60

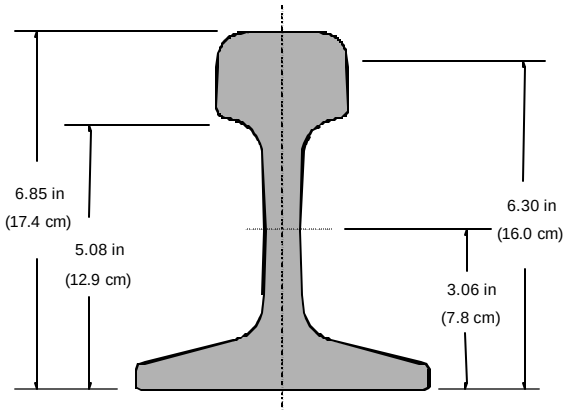

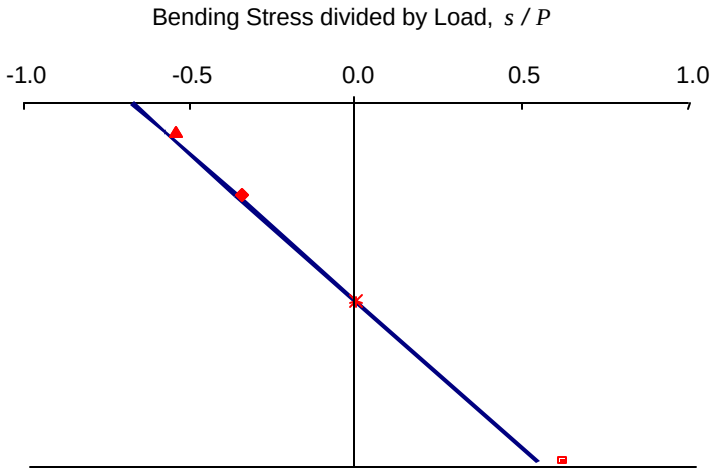

Effective rail length: 52.7 in (133.9 cm)

Correlation coefficient: **0.99708**

Figure B-3. Vertical bending stress calibration for TL/2000-11.

Rail Section: JIS 60

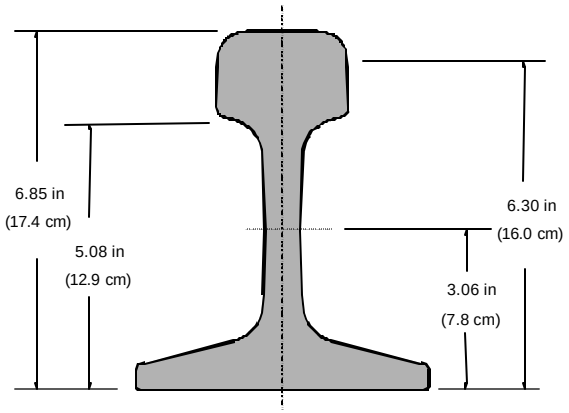

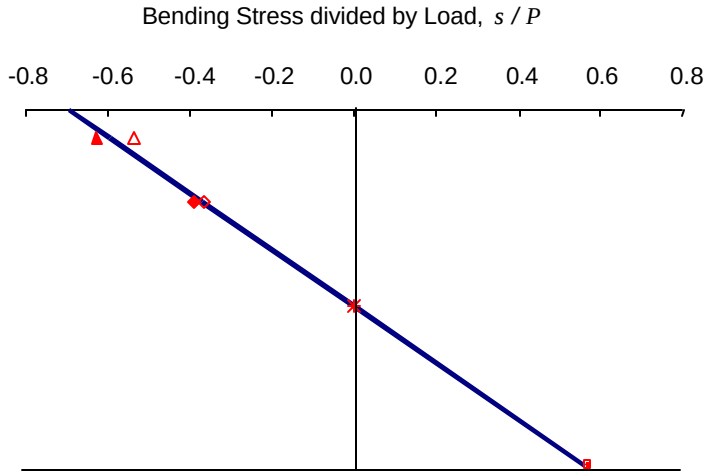

Effective rail length: 54.3 in (137.9 cm)

Correlation coefficient: **0.99762**

Figure B-4. Vertical bending stress calibration for TL/2000-12.

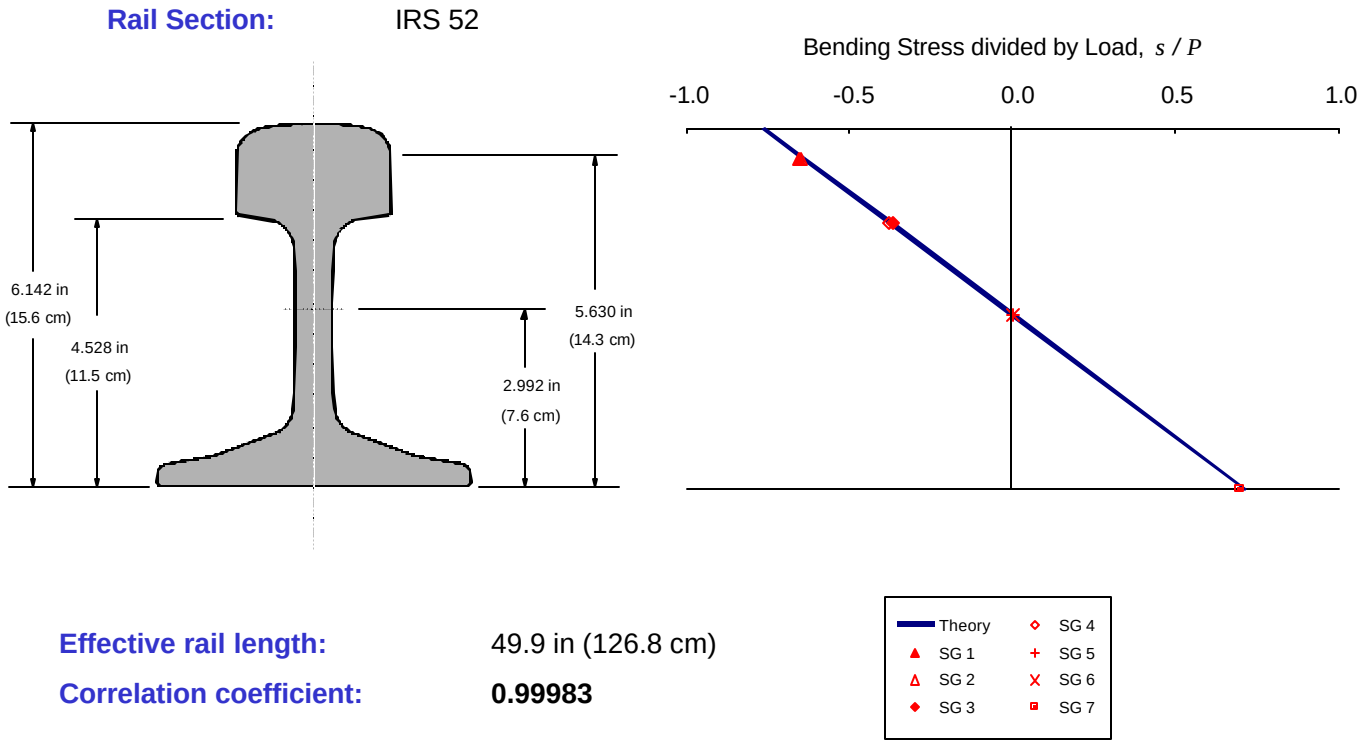

Figure B-5. Vertical bending stress calibration for TL/2000-22.

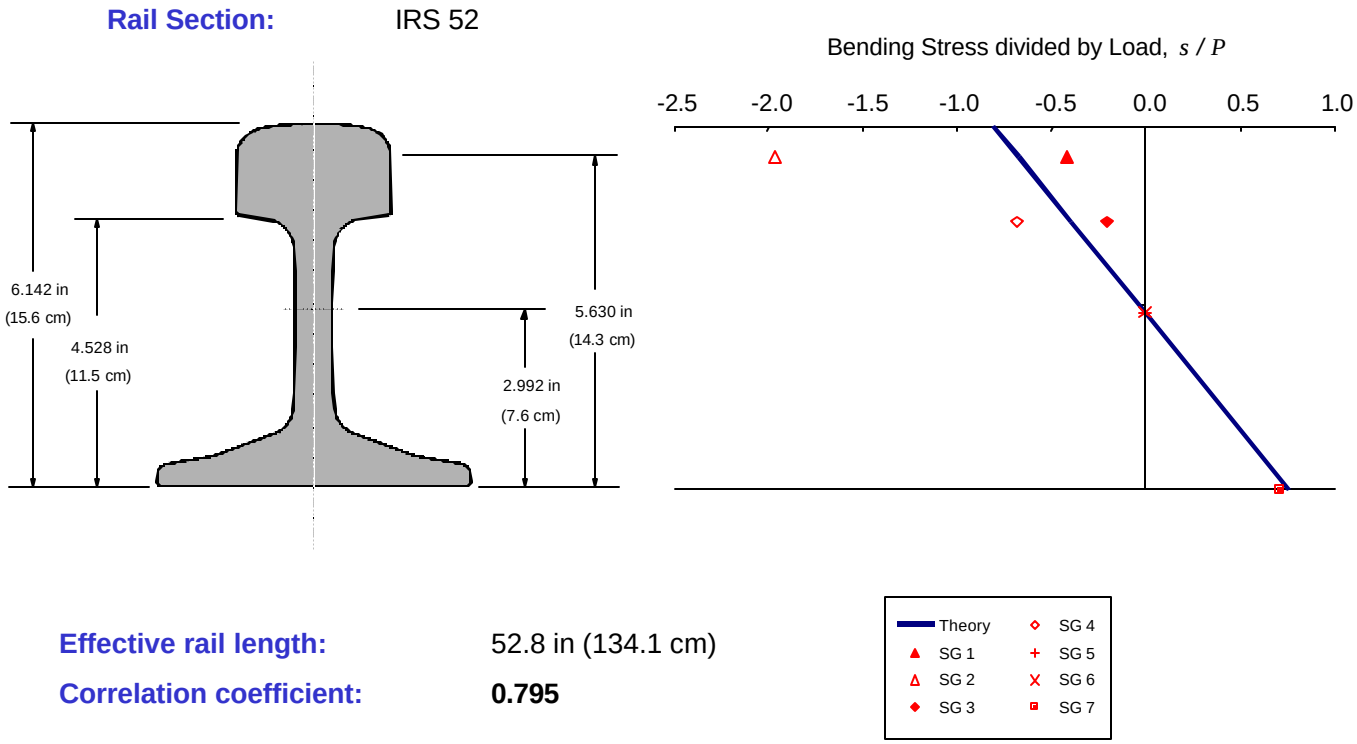

Figure B-6. Vertical bending stress calibration for TL/2001-9.

Rail Section: UIC 60 kg

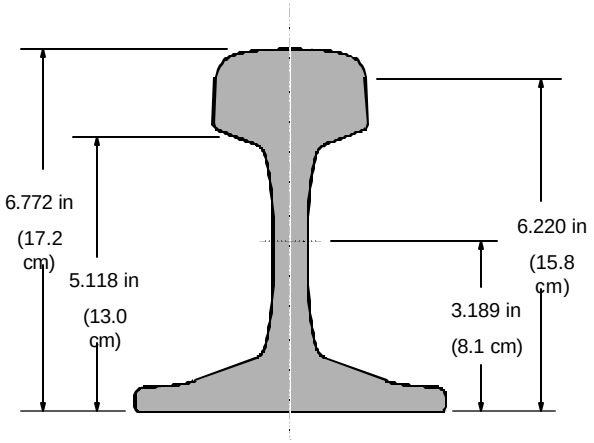

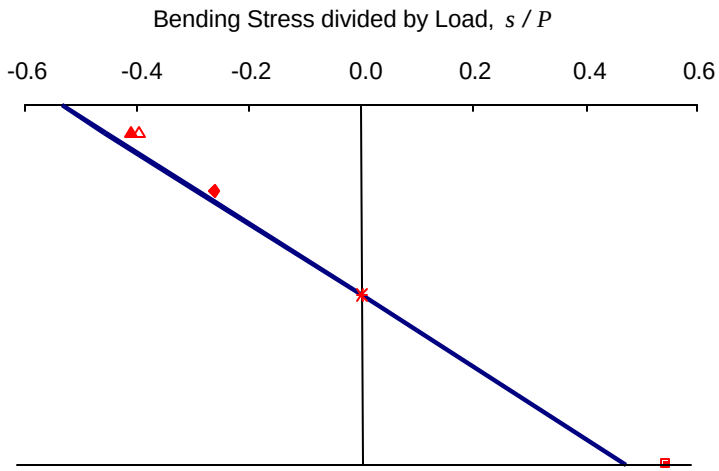

Effective rail length: 43.5 in (110.5 cm)

Correlation coefficient: **0.997**

Figure B-7. Vertical bending stress calibration for TL/2001-14.

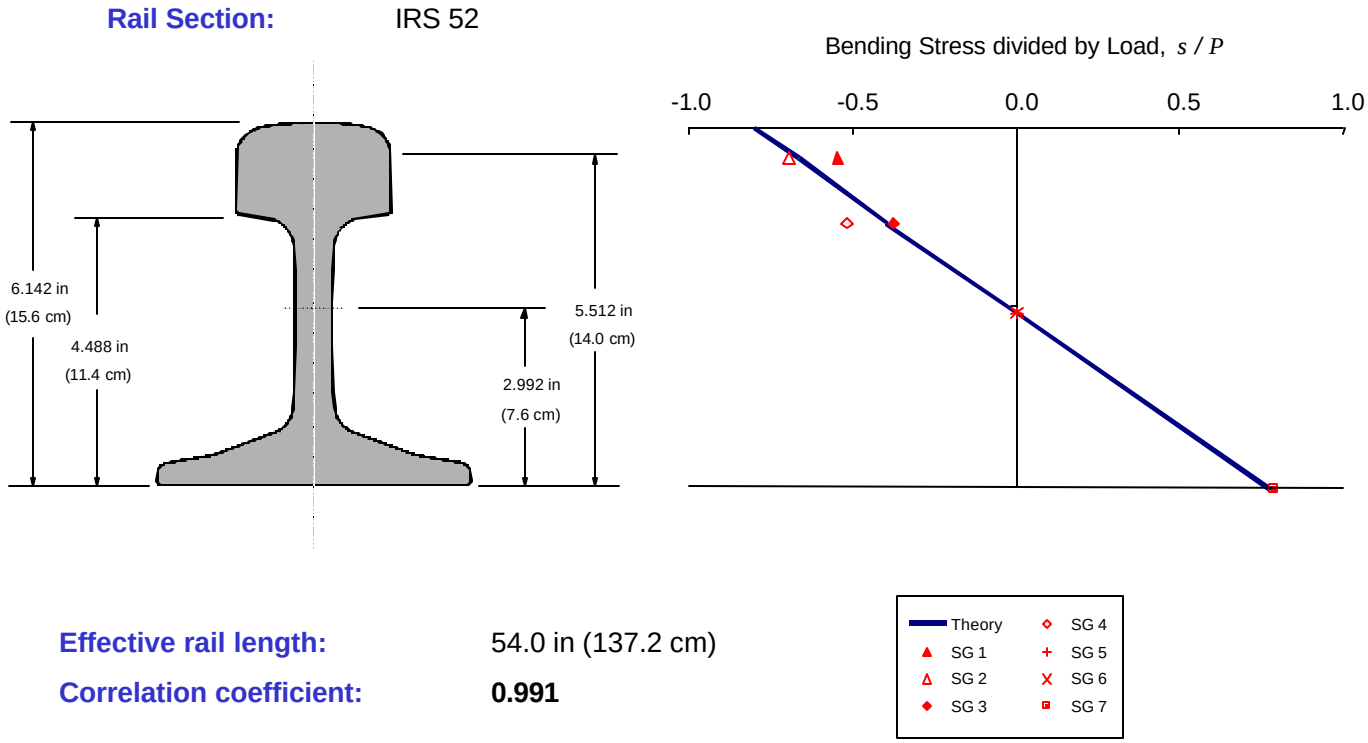

Figure B-8. Vertical bending stress calibration for TL/2001-19.

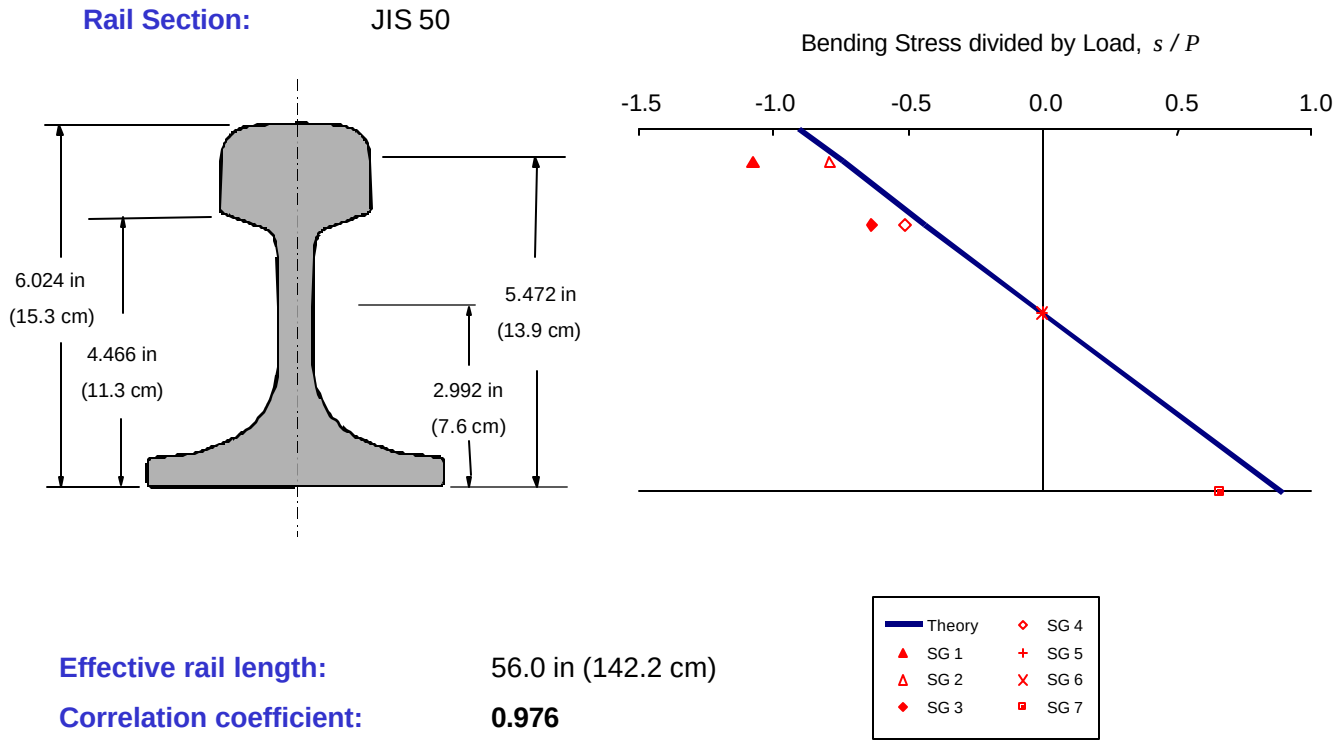

Figure B-9. Vertical bending stress calibration for TL/2001-31.

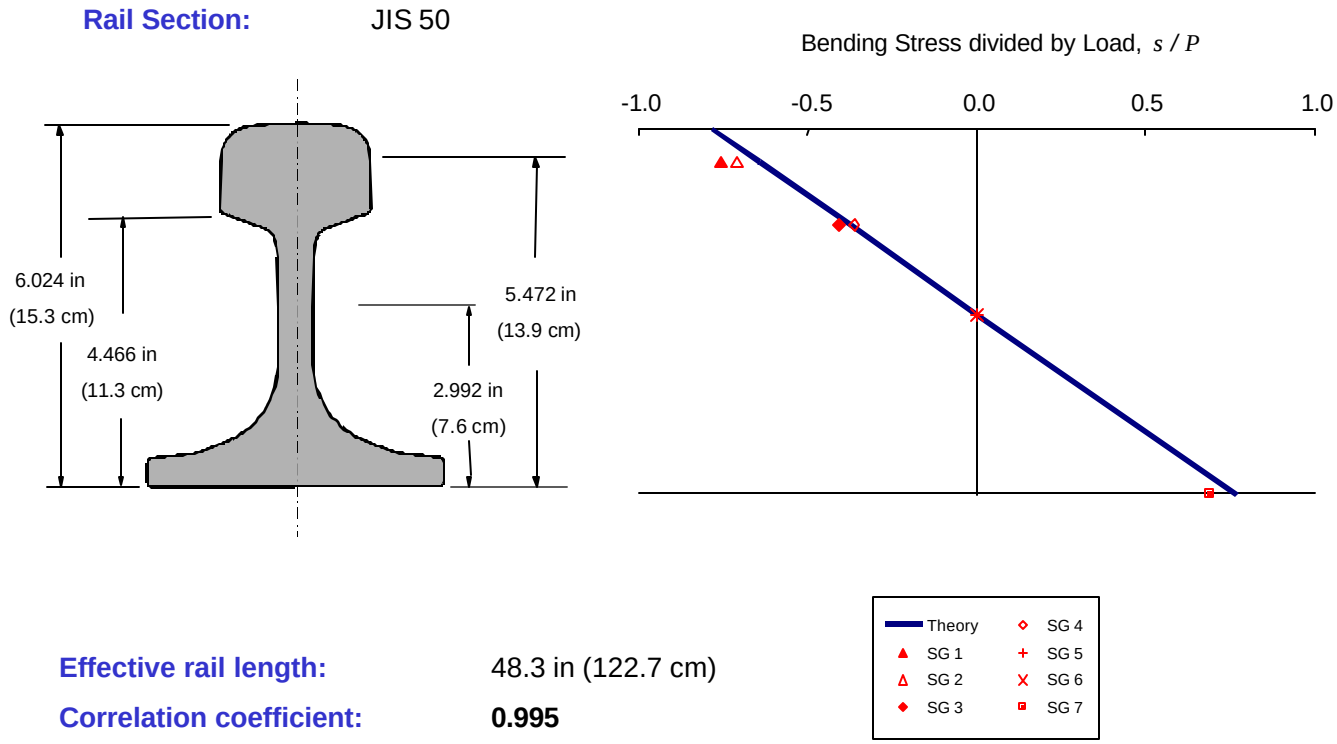

Figure B-10. Vertical bending stress calibration for TL/2001-54.

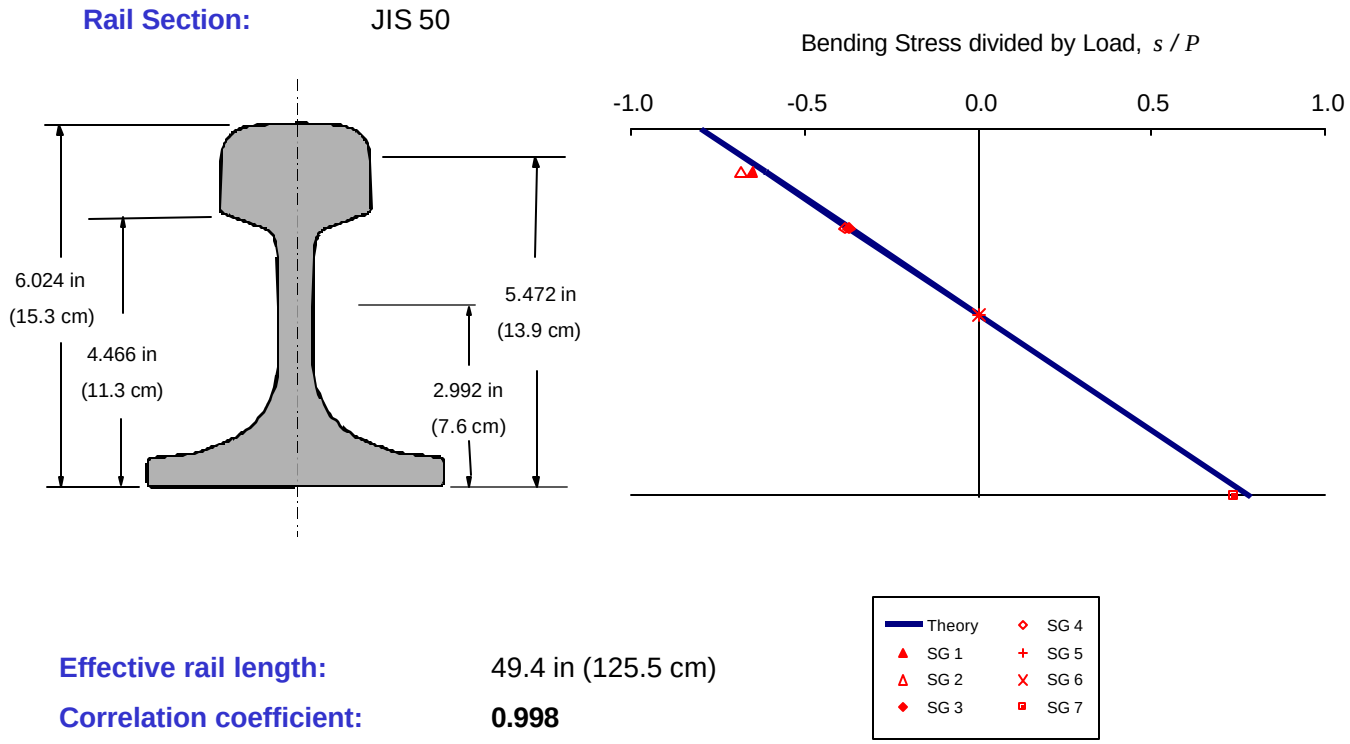

Figure B-11. Vertical bending stress calibration for TL/2001-55.

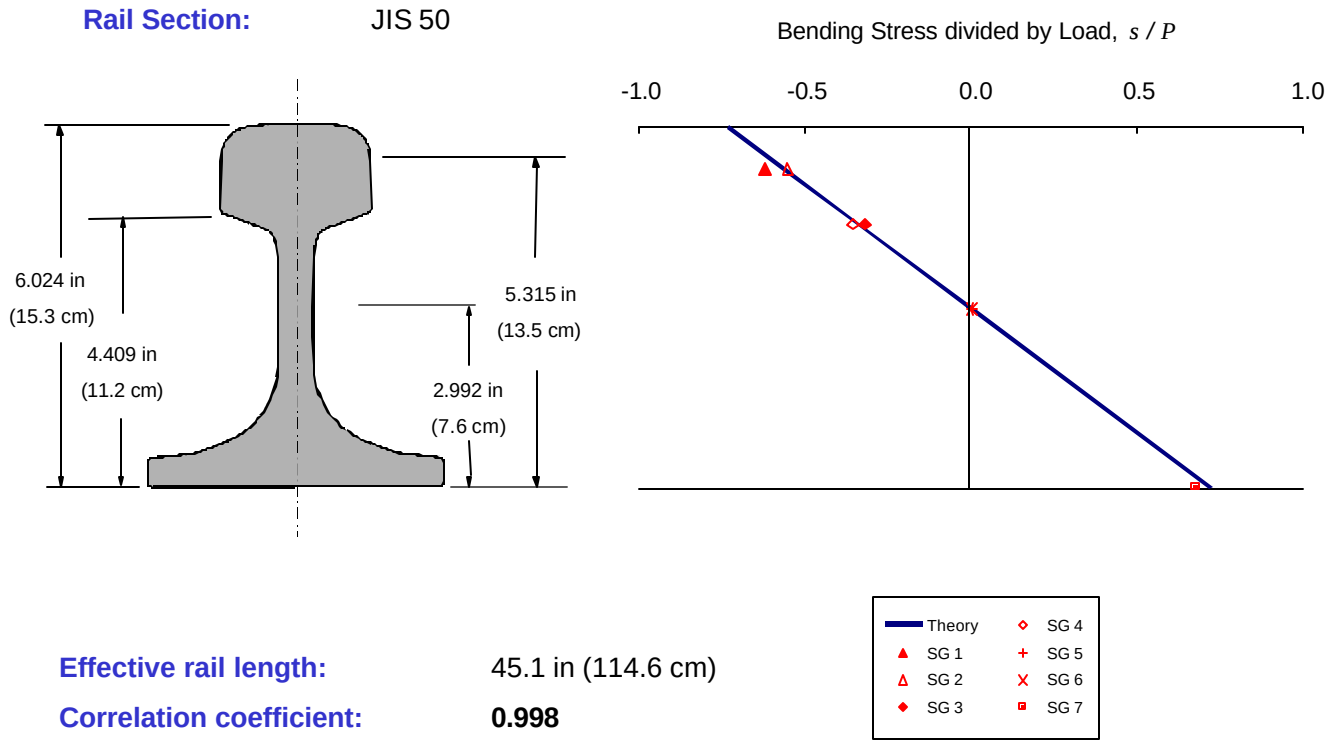

Figure B-12. Vertical bending stress calibration for TL/2001-56.

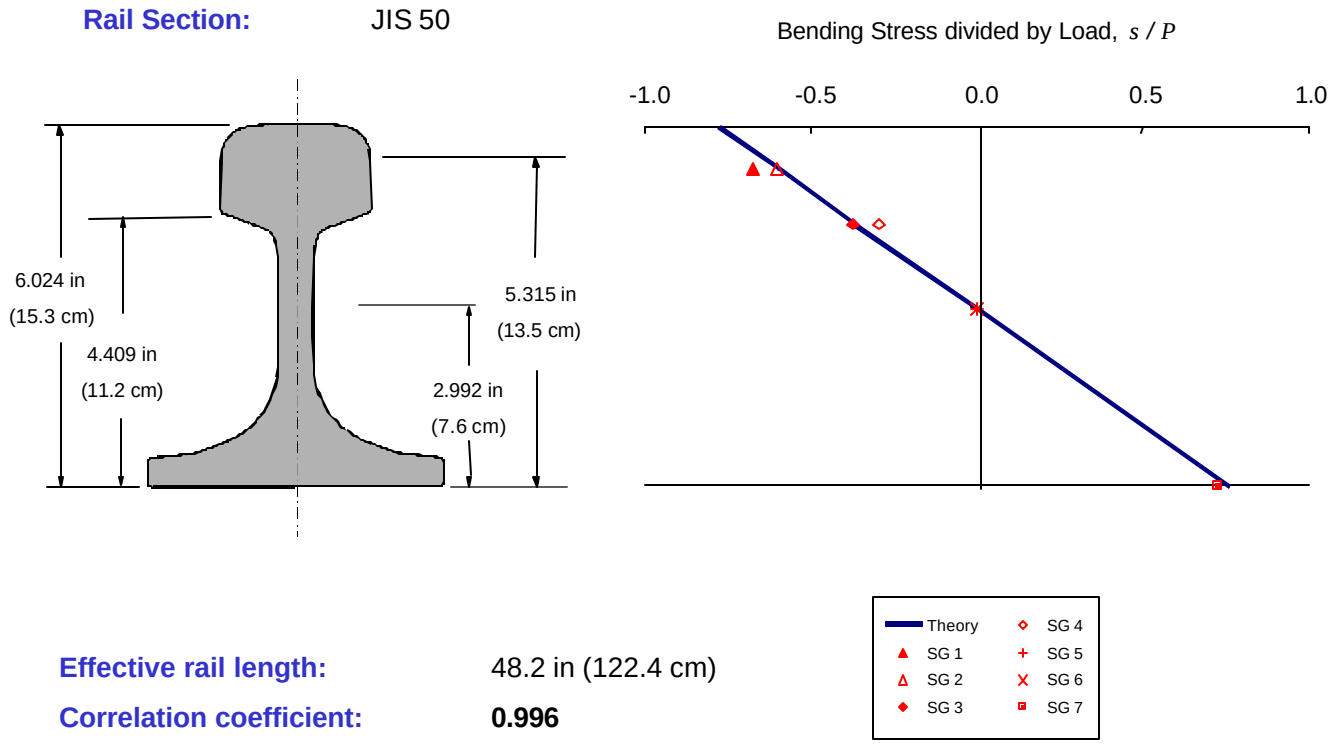

Figure B-13. Vertical bending stress calibration for TL/2001-67.

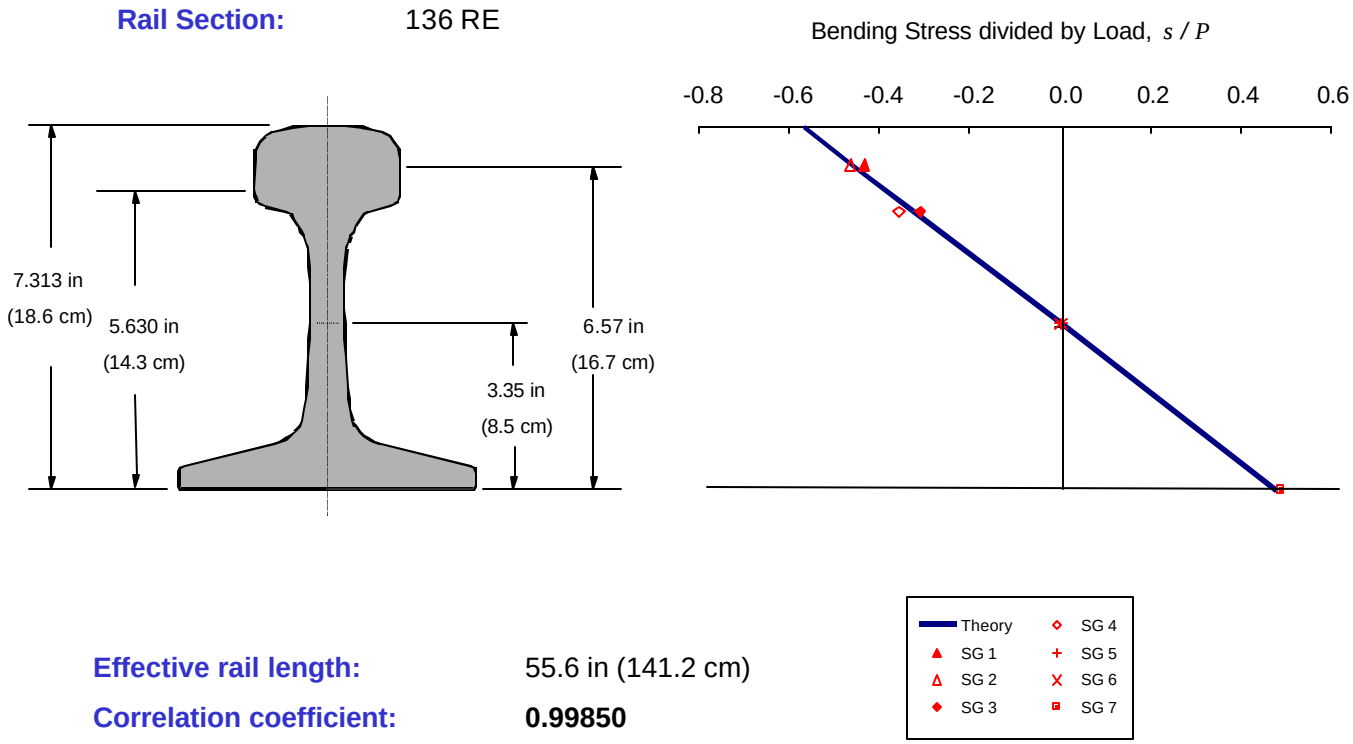

Figure B-14. Vertical bending stress calibration for TL/2001-68.

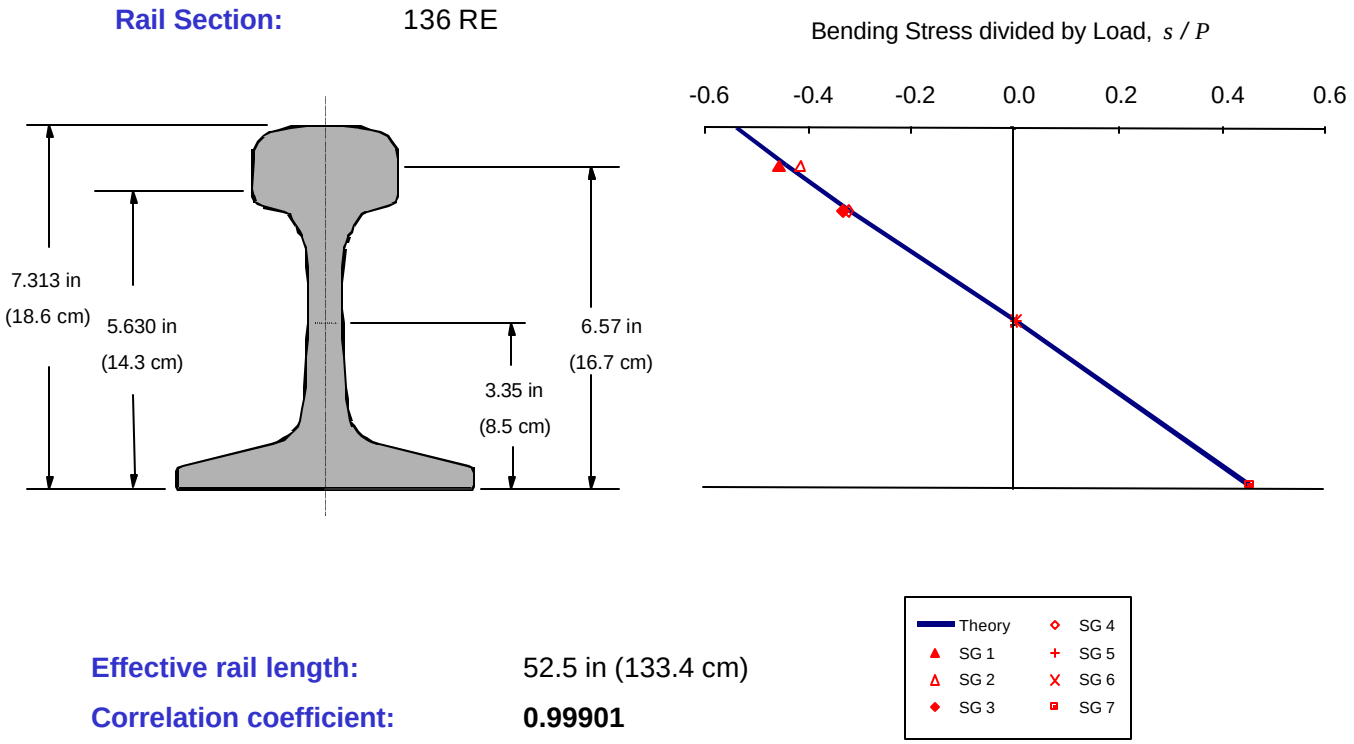

Figure B-15. Vertical bending stress calibration for TL/2001-103.

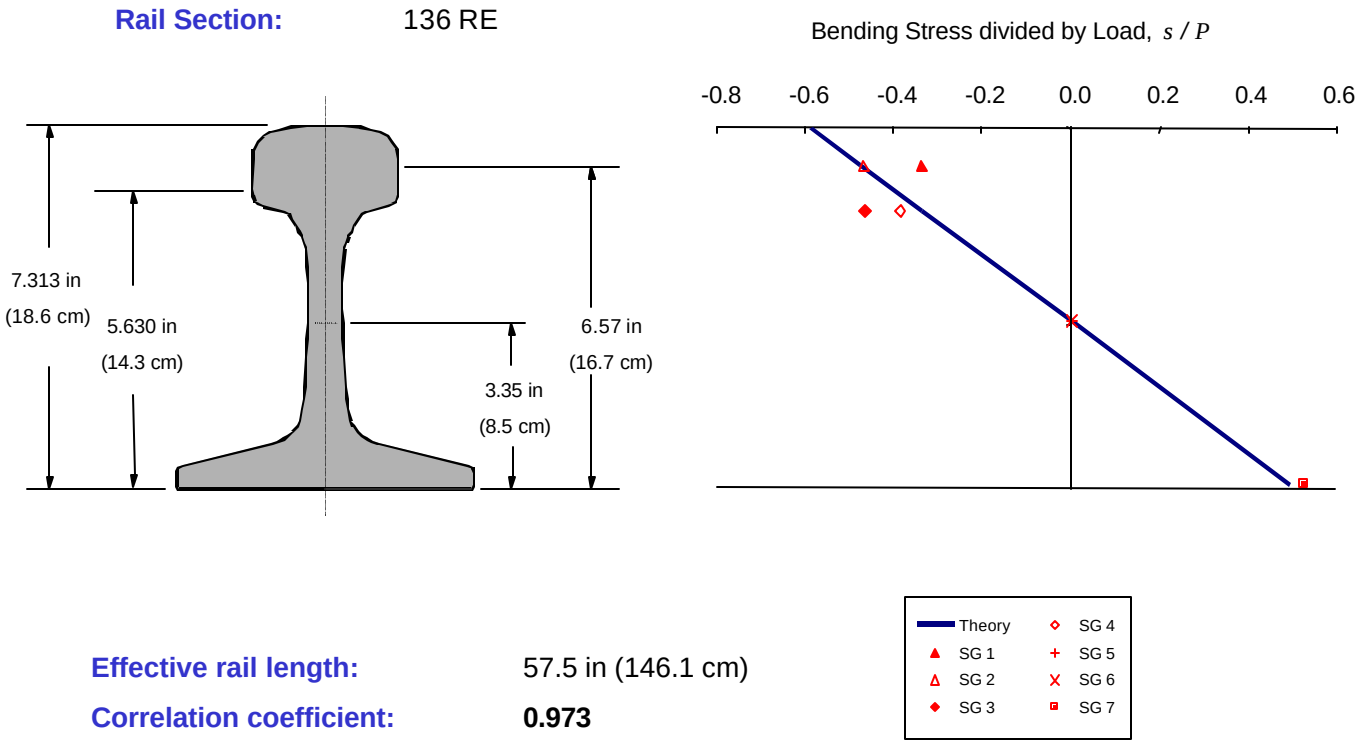

Figure B-16. Vertical bending stress calibration for TL/2001-104.

Rail Section: UIC 60 kg

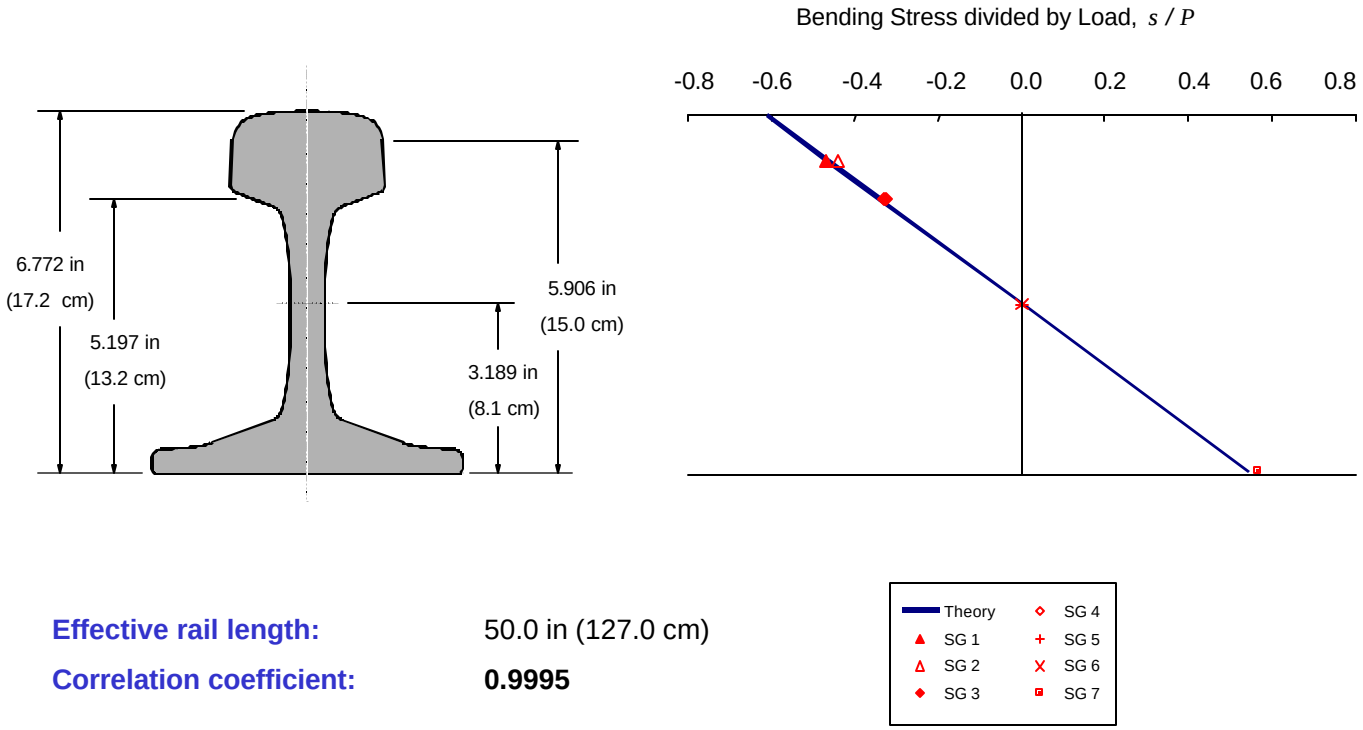

Effective rail length: 50.0 in (127.0 cm)

Correlation coefficient: **0.9995**

Figure B-17. Vertical bending stress calibration for TL/2002-127.

Rail Section: UIC 60 kg

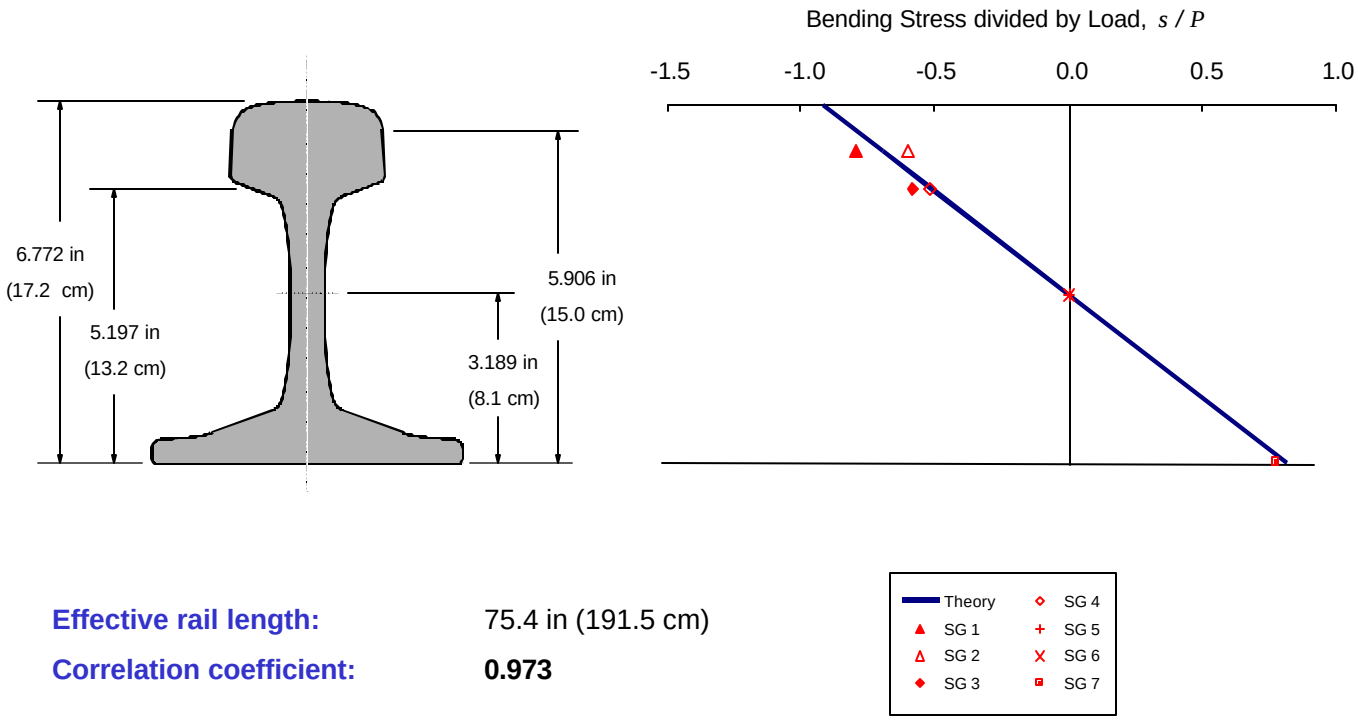

Effective rail length: 75.4 in (191.5 cm)

Correlation coefficient: **0.973**

Figure B-18. Vertical bending stress calibration for TL/2002-128.

Rail Section: UIC 60 kg

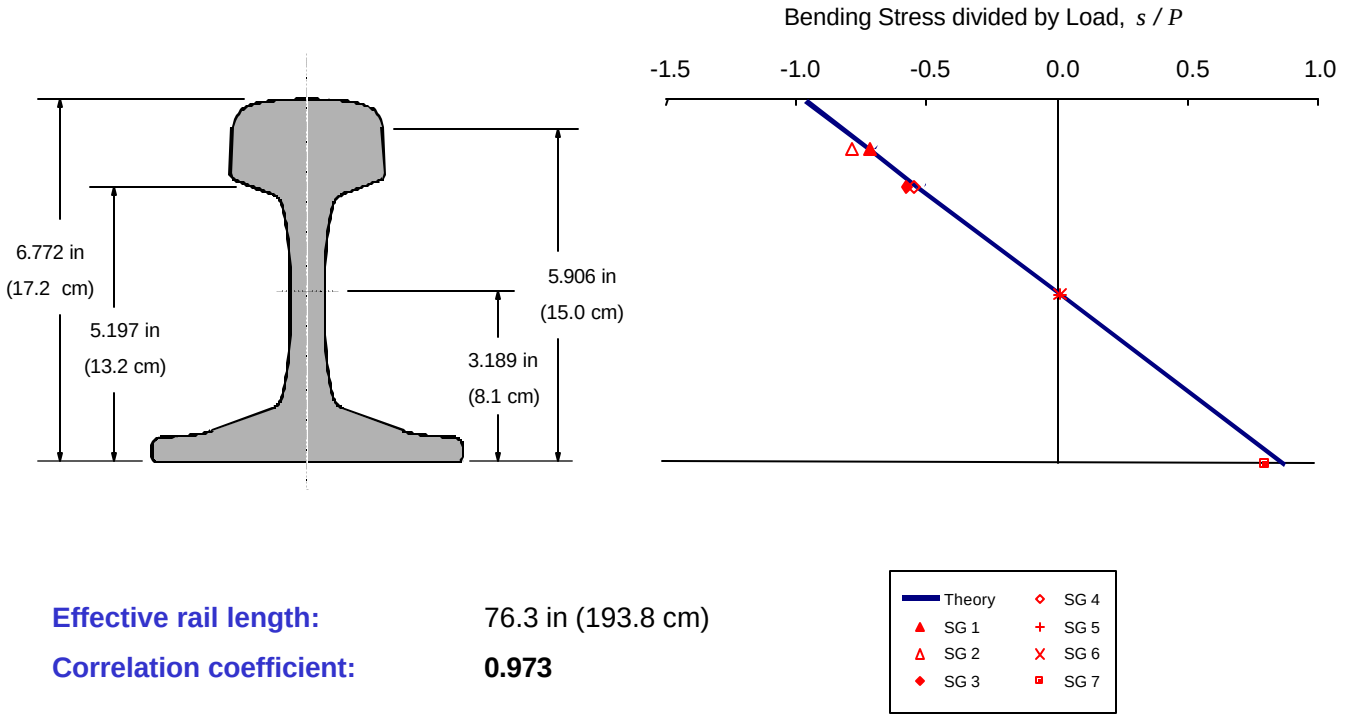

Effective rail length: 76.3 in (193.8 cm)

Correlation coefficient: **0.973**

Figure B-19. Vertical bending stress calibration for TL/2002-129.

Rail Section: UIC 60 kg

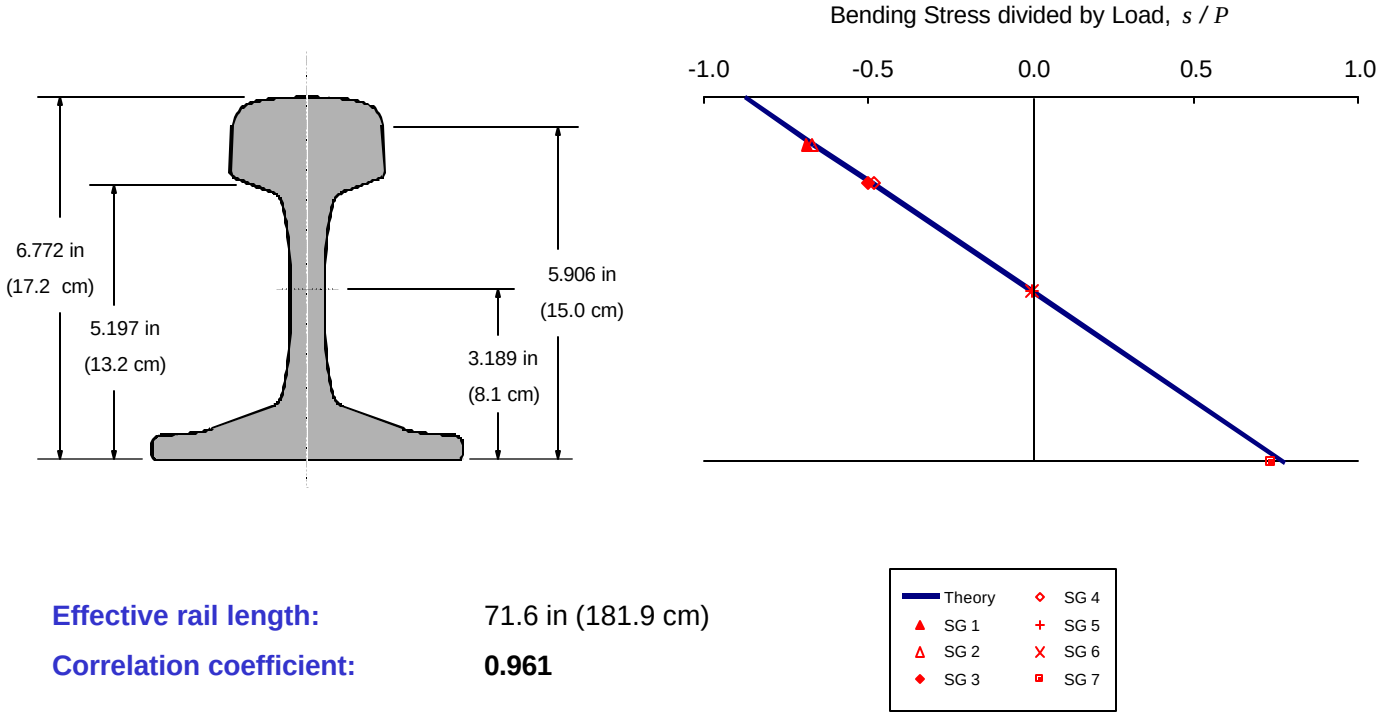

Effective rail length: 71.6 in (181.9 cm)

Correlation coefficient: **0.961**

Figure B-20. Vertical bending stress calibration for TL/2002-138.

APPENDIX C. CORRELATIONS BETWEEN RDSO TEST DATA AND RESULTS FROM ENGINEERING ANALYSES

This appendix contains 19 plots showing the growth of rail defects as measured in the RDSO test program. These plots also show a comparison with calculations from the engineering fracture mechanics based model for rail defect growth. In each plot, solid diamond-shaped symbols represent the RDSO test data and a solid continuous line represents the results from the analysis.

The flaw size in each plot was measured using 70-degree ultrasonic probes. Moreover, the measured flaw size for each defect is defined as the vertical distance from the top to the bottom of the defect (Figure C-1). In the engineering analyses for each defect, detail fractures and tache ovale defects are assumed to have an elliptical shape (aspect ratio of 0.7 is also assumed), and squat defects are assumed to have a semi-circular shape.

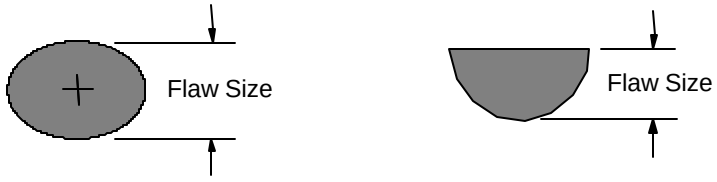

(a) Detail Fracture or Tache Ovale *(b) Squat*

Figure C-1. Definition of flaw size for different defects.

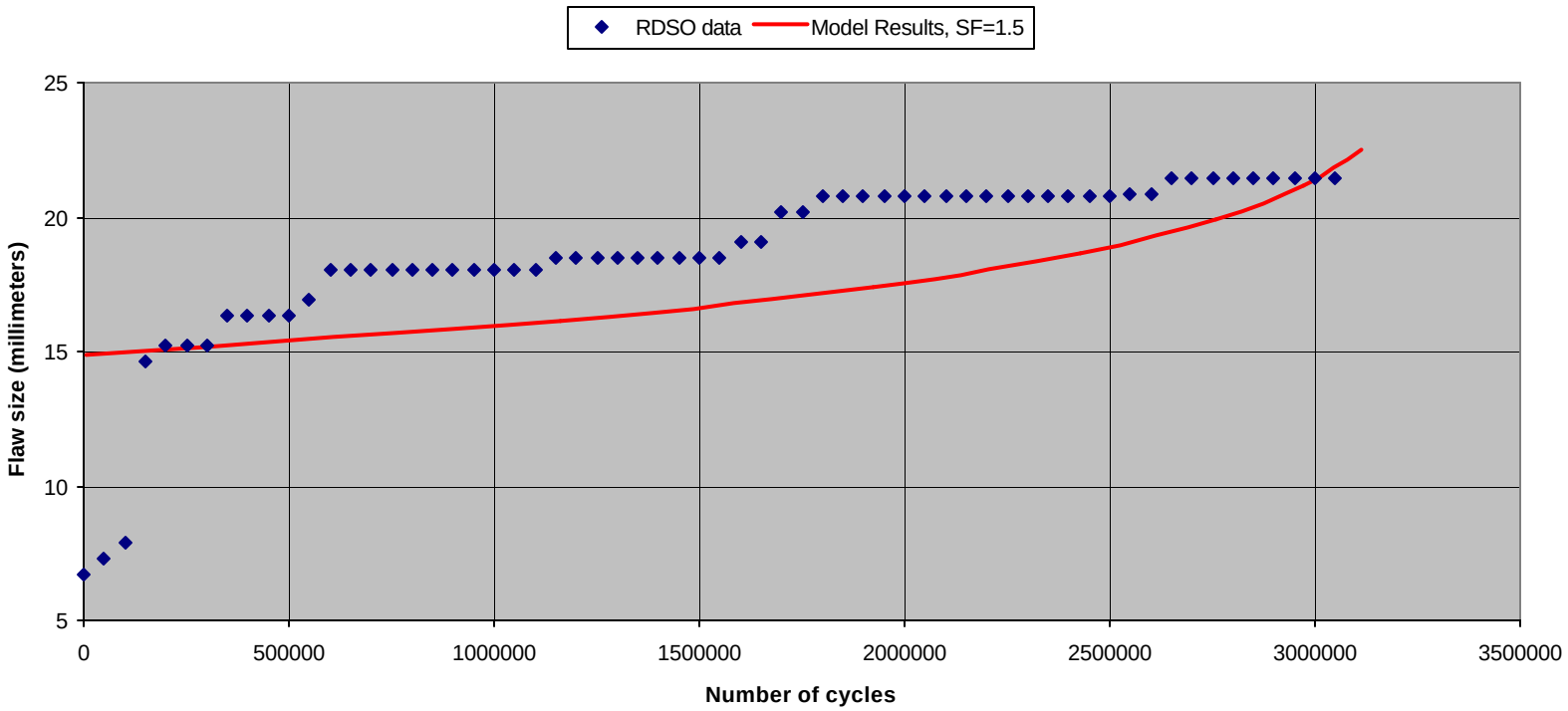

Figure C-2. Correlation between RDSO test data and engineering model results for TL/2000-10 (squat).

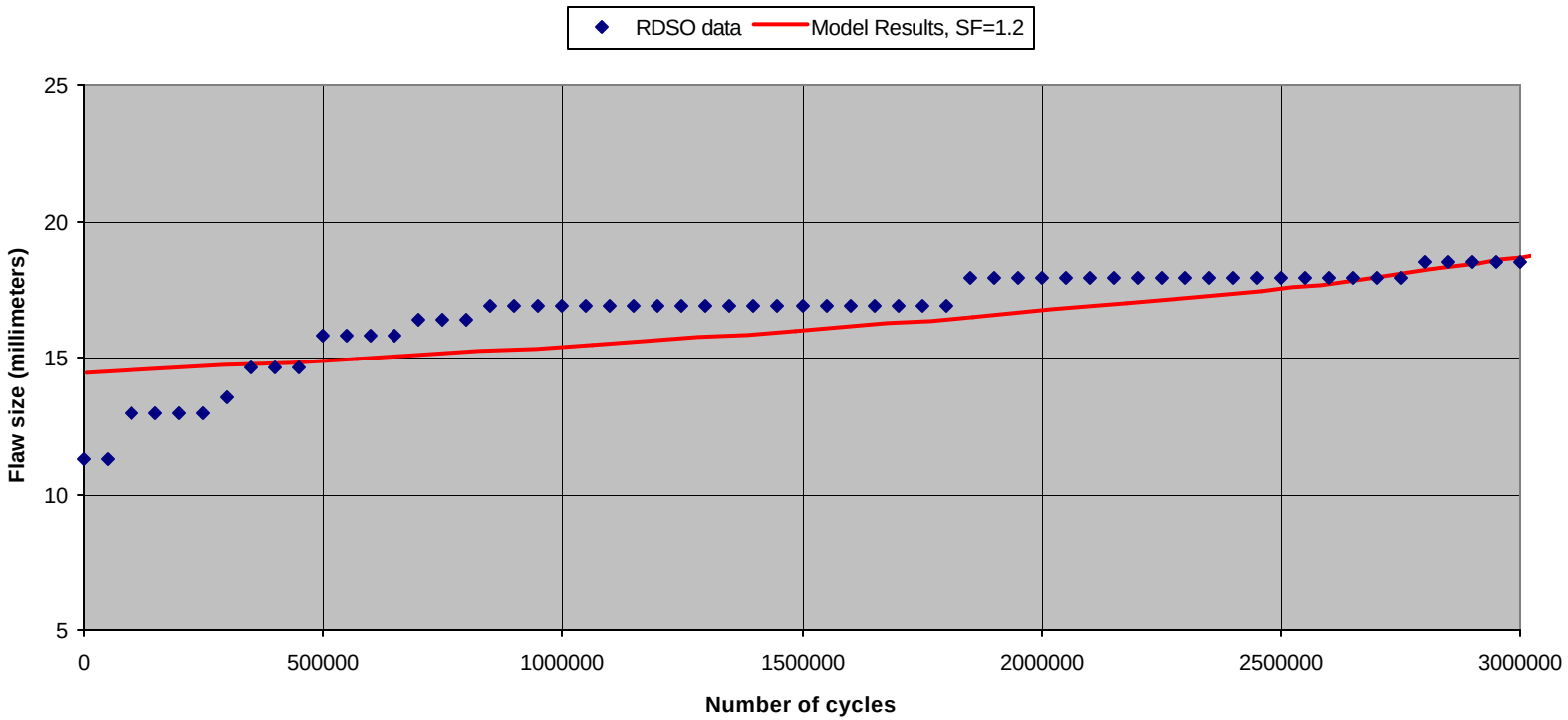

Figure C-3. Correlation between RDSO test data and engineering model results for TL/2000-11 (squat).

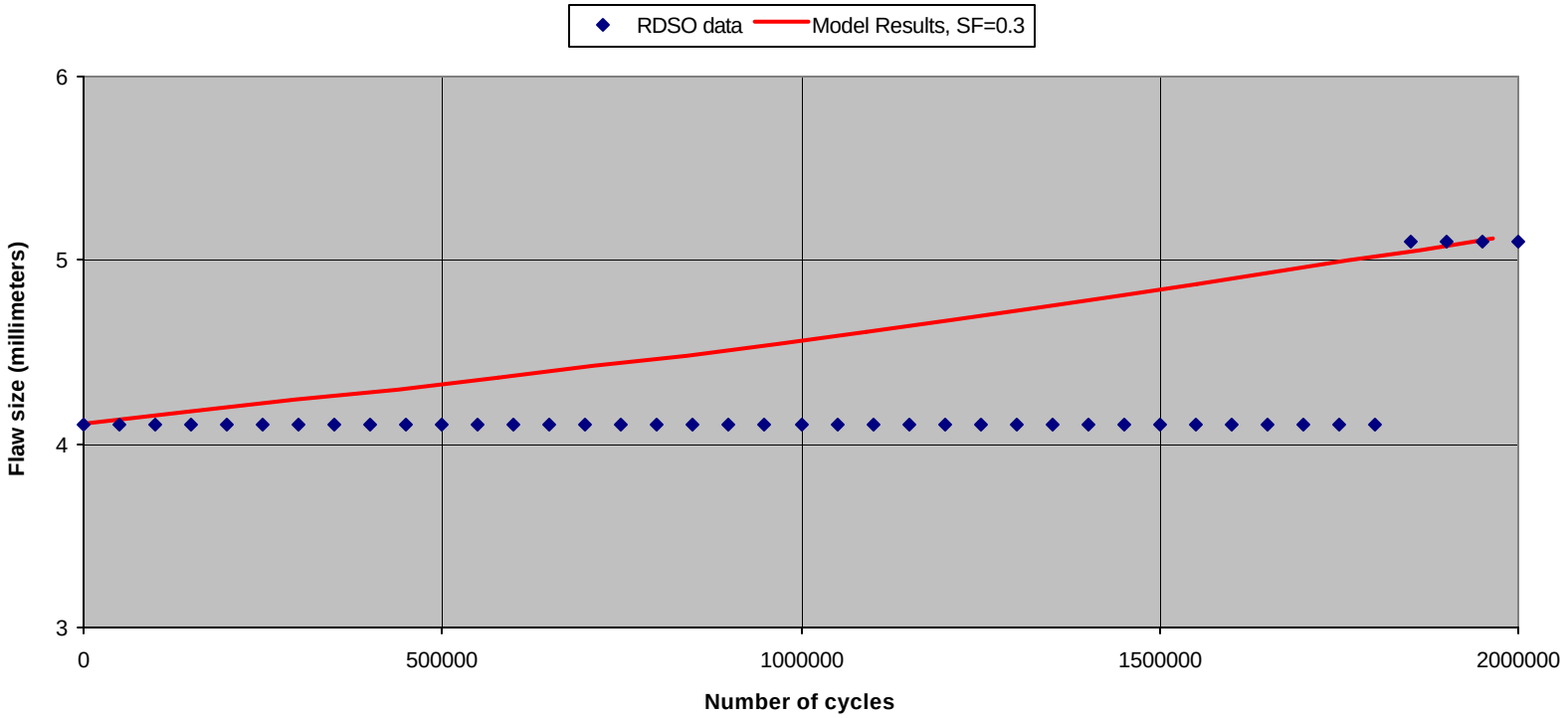

Figure C-4. Correlation between RDSO test data and engineering model results for TL/2000-12 (squat).

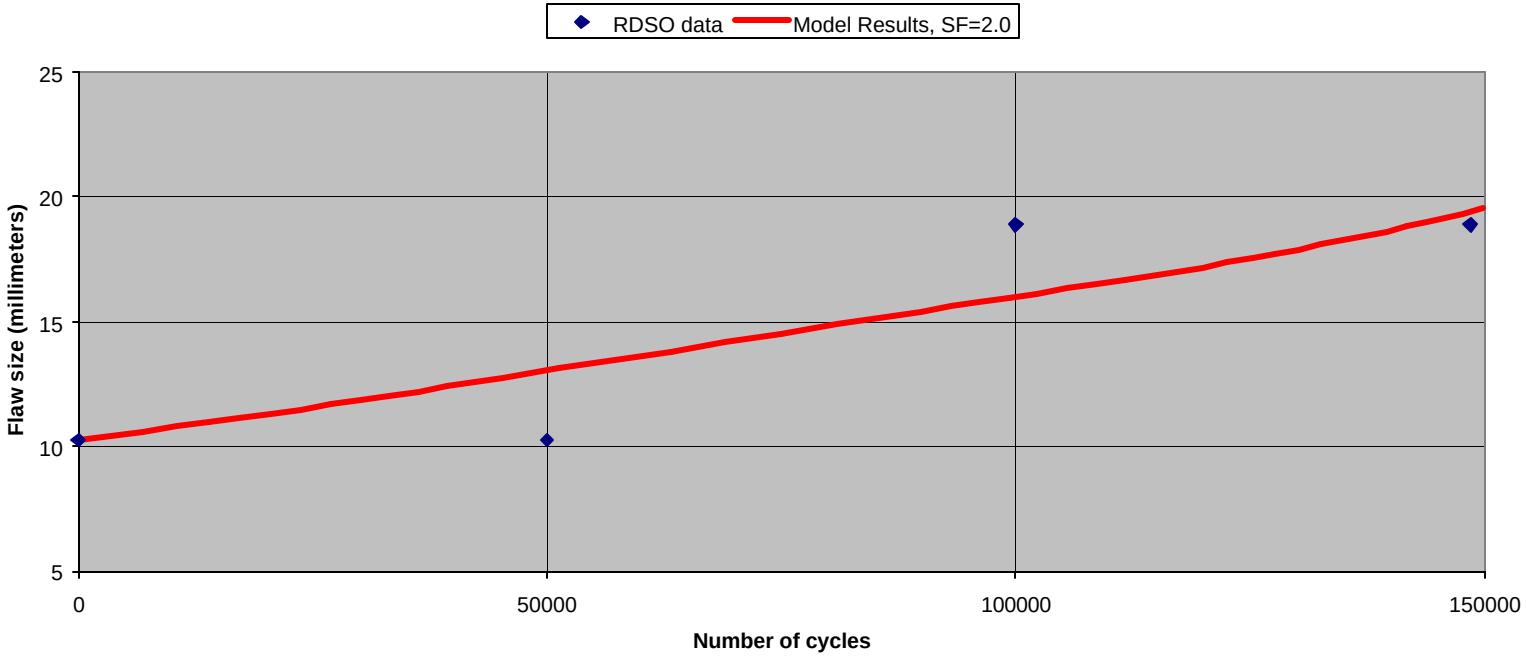

Figure C-5. Correlation between RDSO test data and engineering model results for TL/2000-22 (tache ovale).

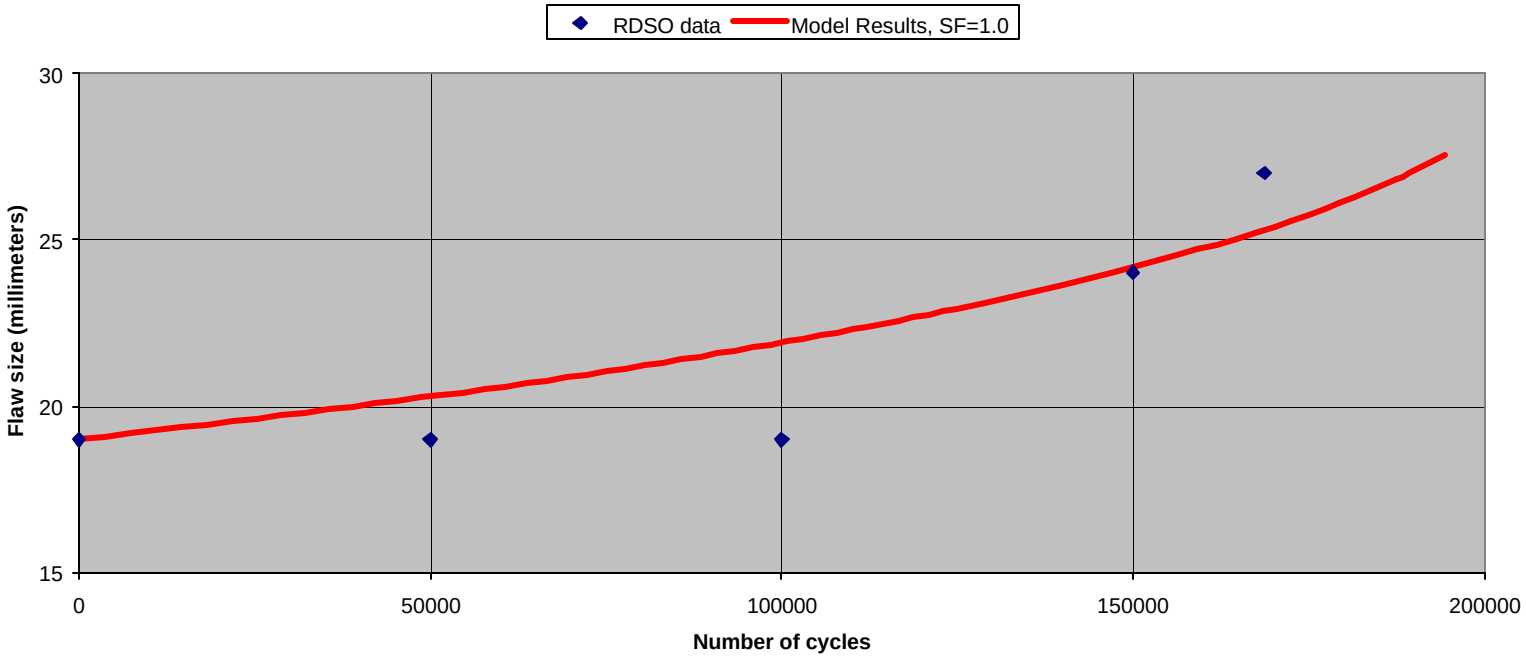

Figure C-6. Correlation between RDSO test data and engineering model results for TL/2001-9 (tache ovale).

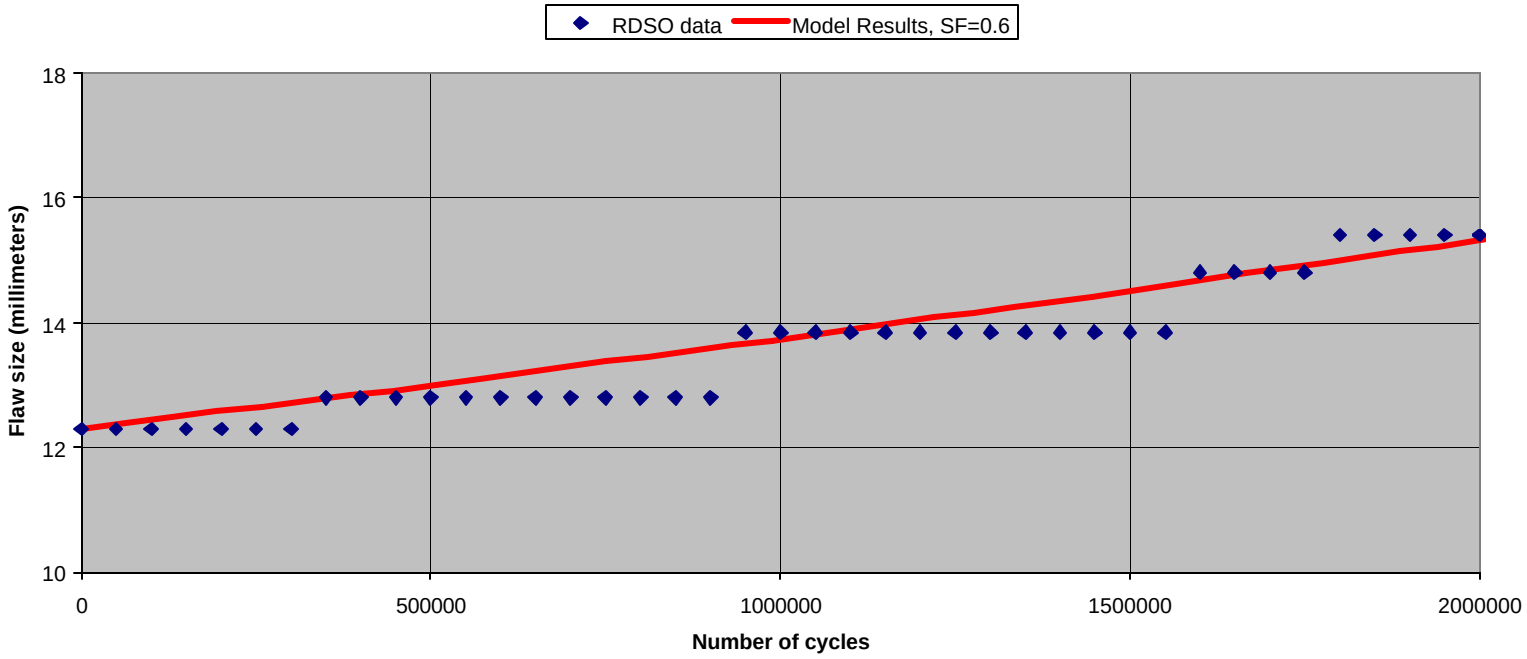

Figure C-7. Correlation between RDSO test data and engineering model results for TL/2001-14 (tache ovale).

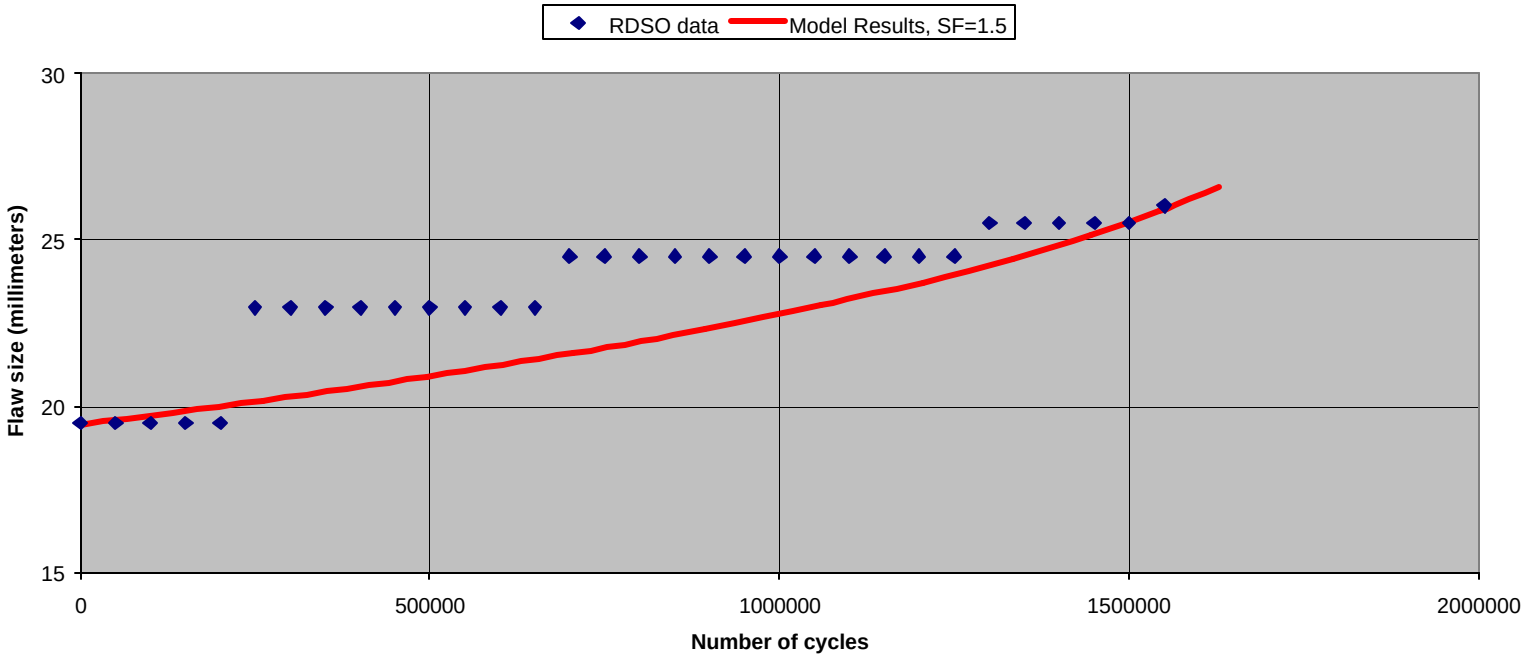

Figure C-8 Correlation between RDSO test data and engineering model results for TL/2001-19 (tache ovale).

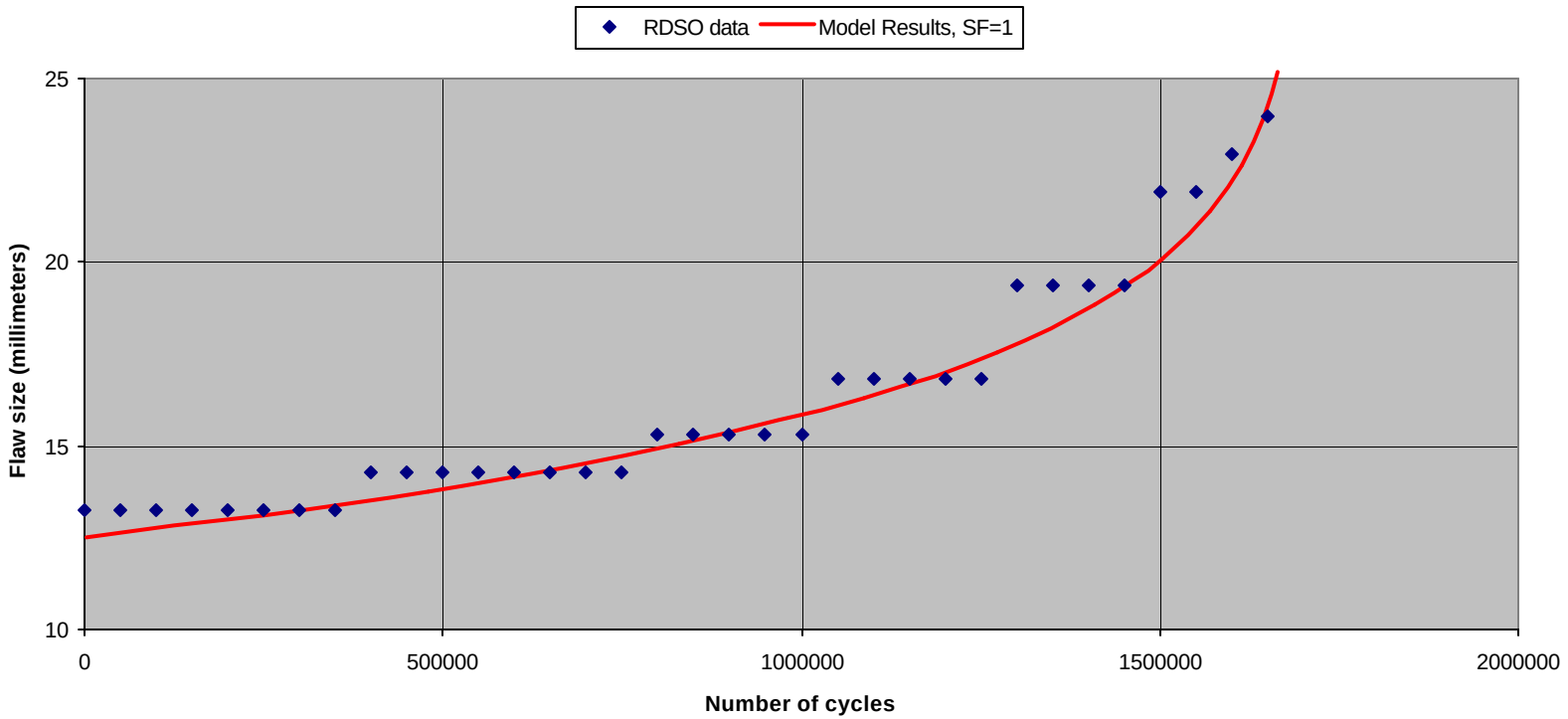

Figure C-9. Correlation between RDSO test data and engineering model results for TL/2001-31 (squat).

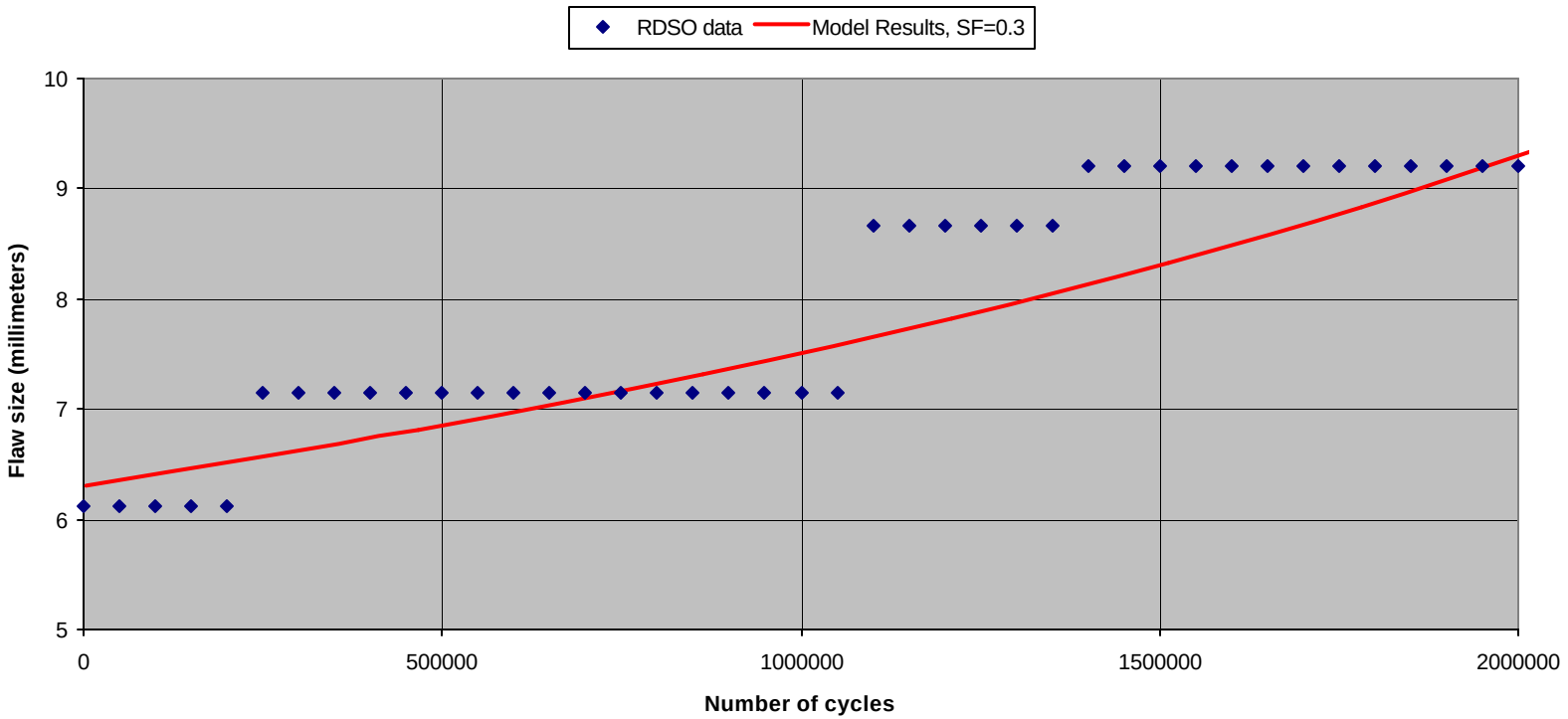

Figure C-10. Correlation between RDSO test data and engineering model results for TL/2001-54 (squat).

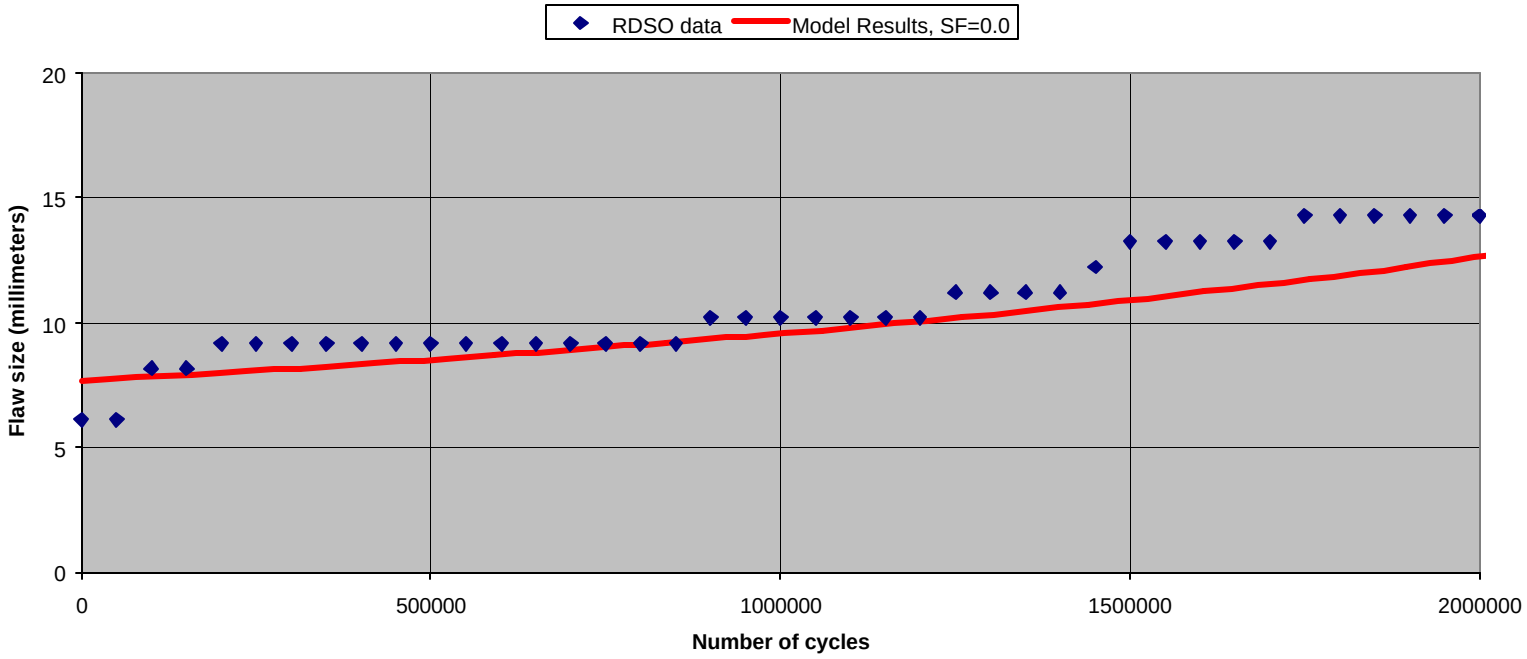

Figure C-11. Correlation between RDSO test data and engineering model results for TL/2001-55 (squat).

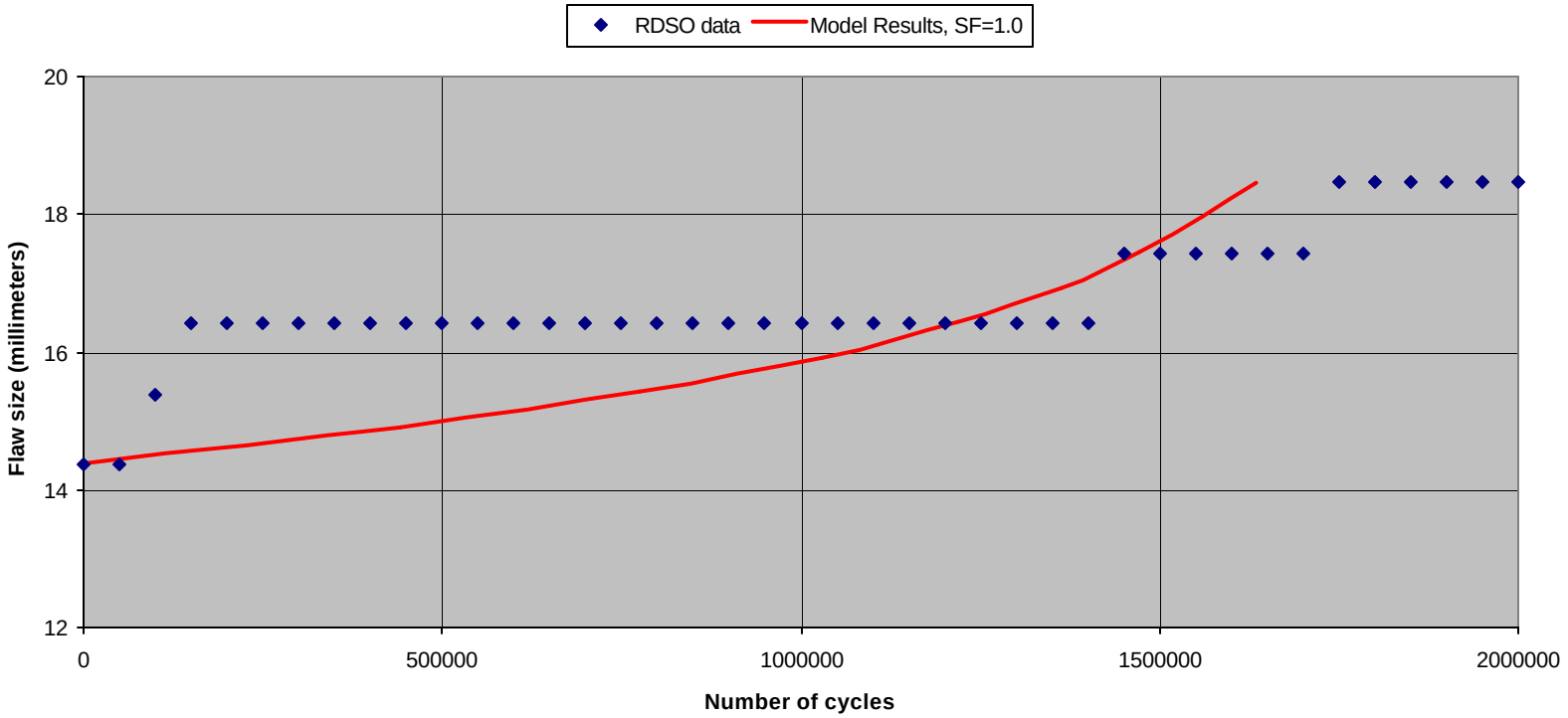

Figure C-12. Correlation between RDSO test data and engineering model results for TL/2001-56 (squat).

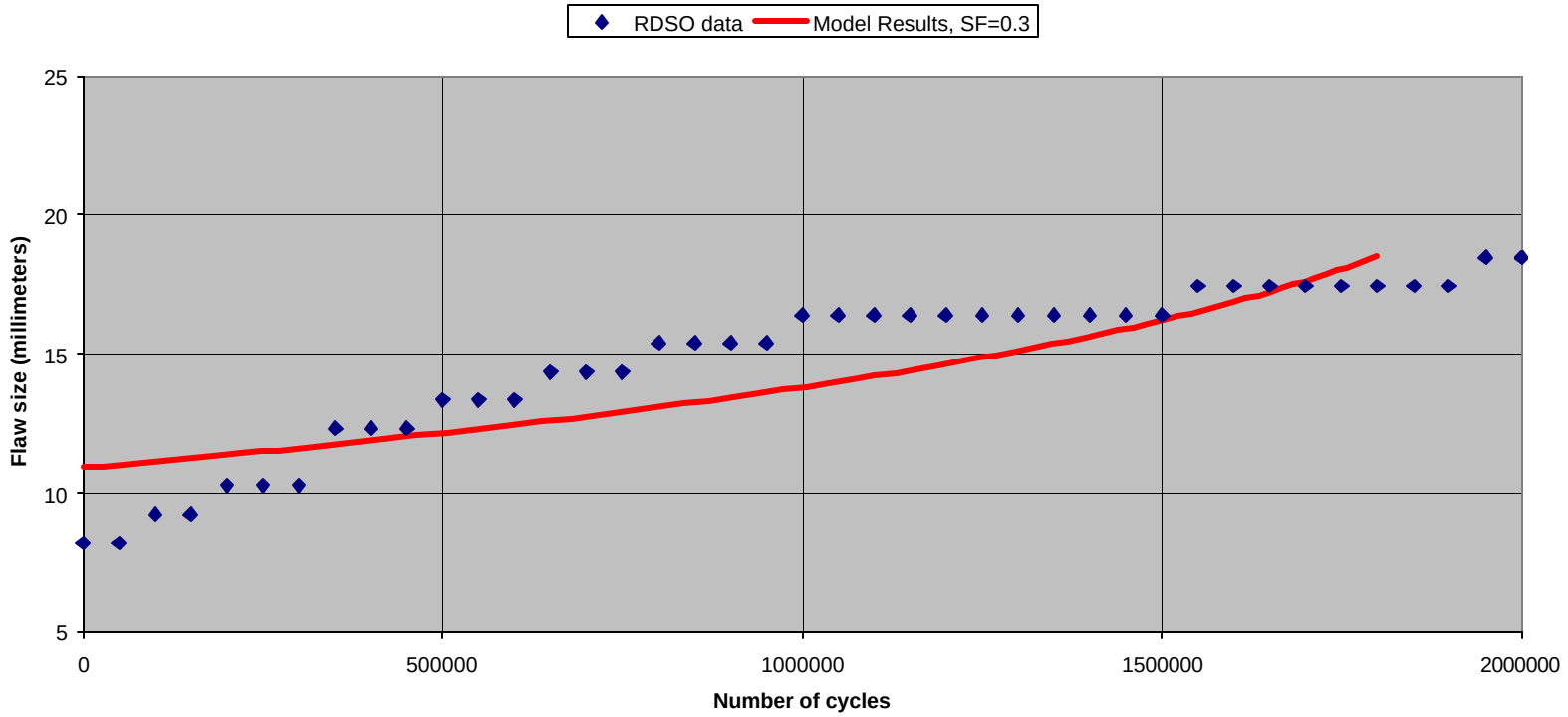

Figure C-13. Correlation between RDSO test data and engineering model results for TL/2001-67 (squat).

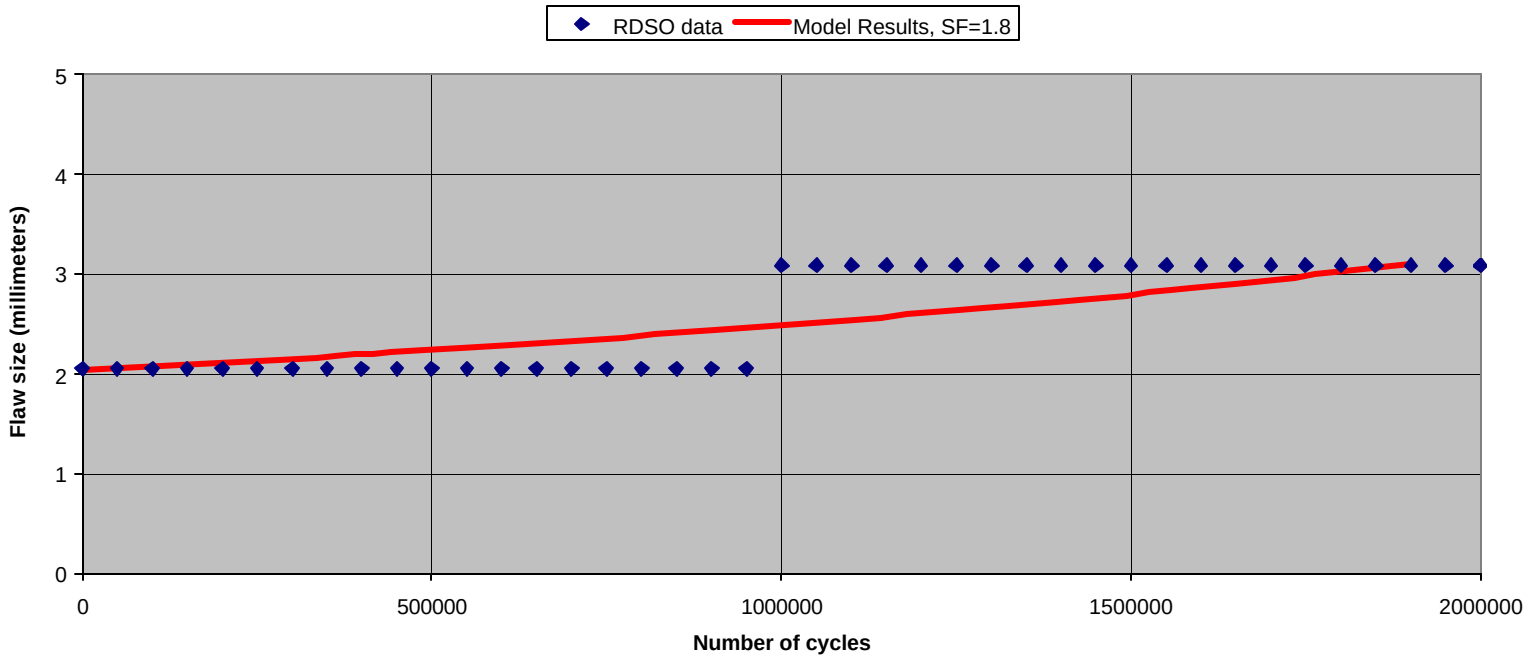

Figure C-14. Correlation between RDSO test data and engineering model results for TL/2001-68 (detail fracture).

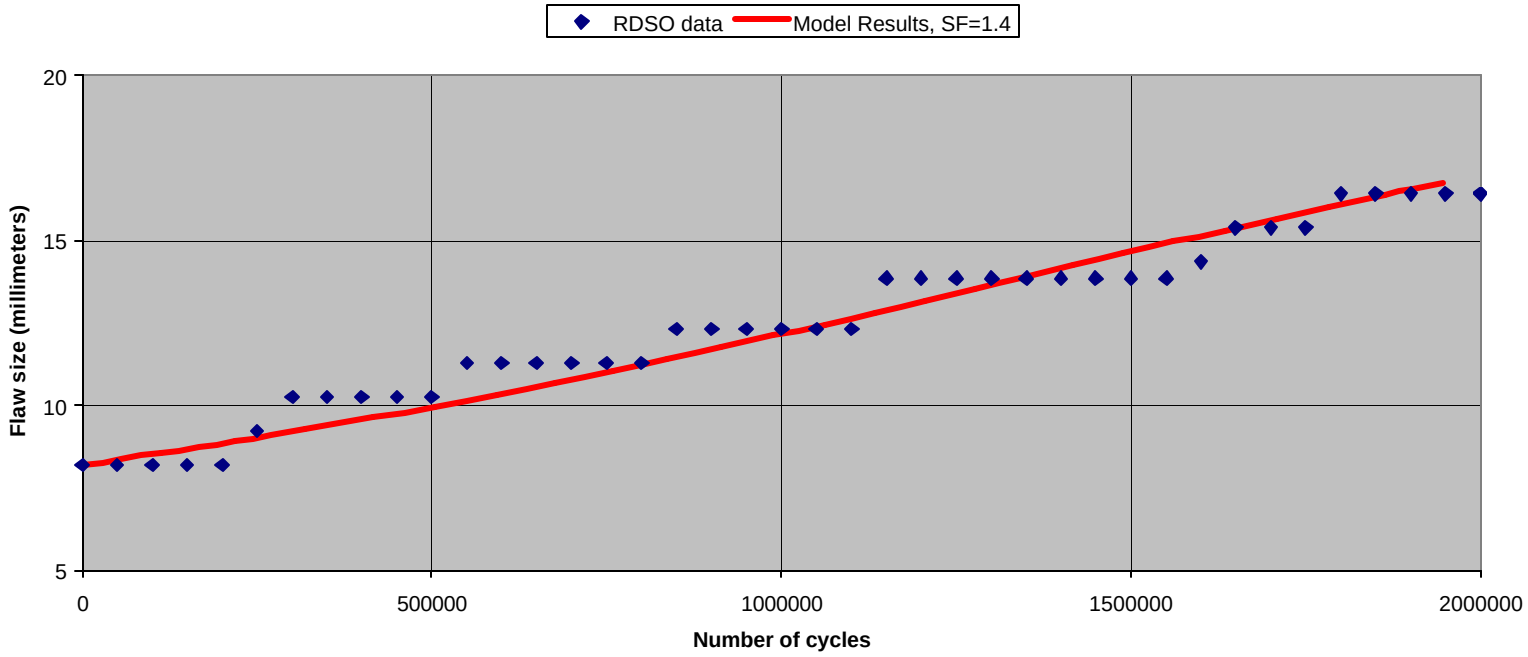

Figure C-15. Correlation between RDSO test data and engineering model results for TL/2001-103 (detail fracture).

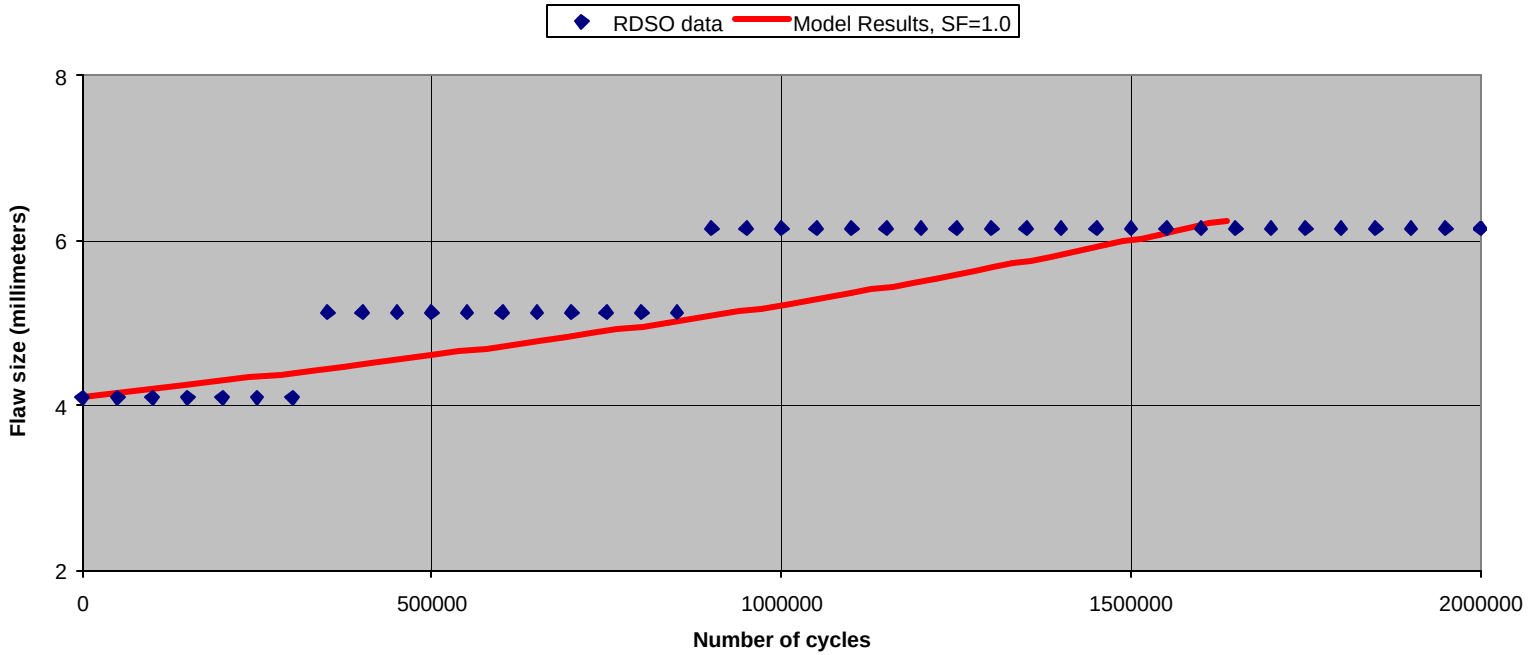

Figure C-16. Correlation between RDSO test data and engineering model results for TL/2001-104 (detail fracture).

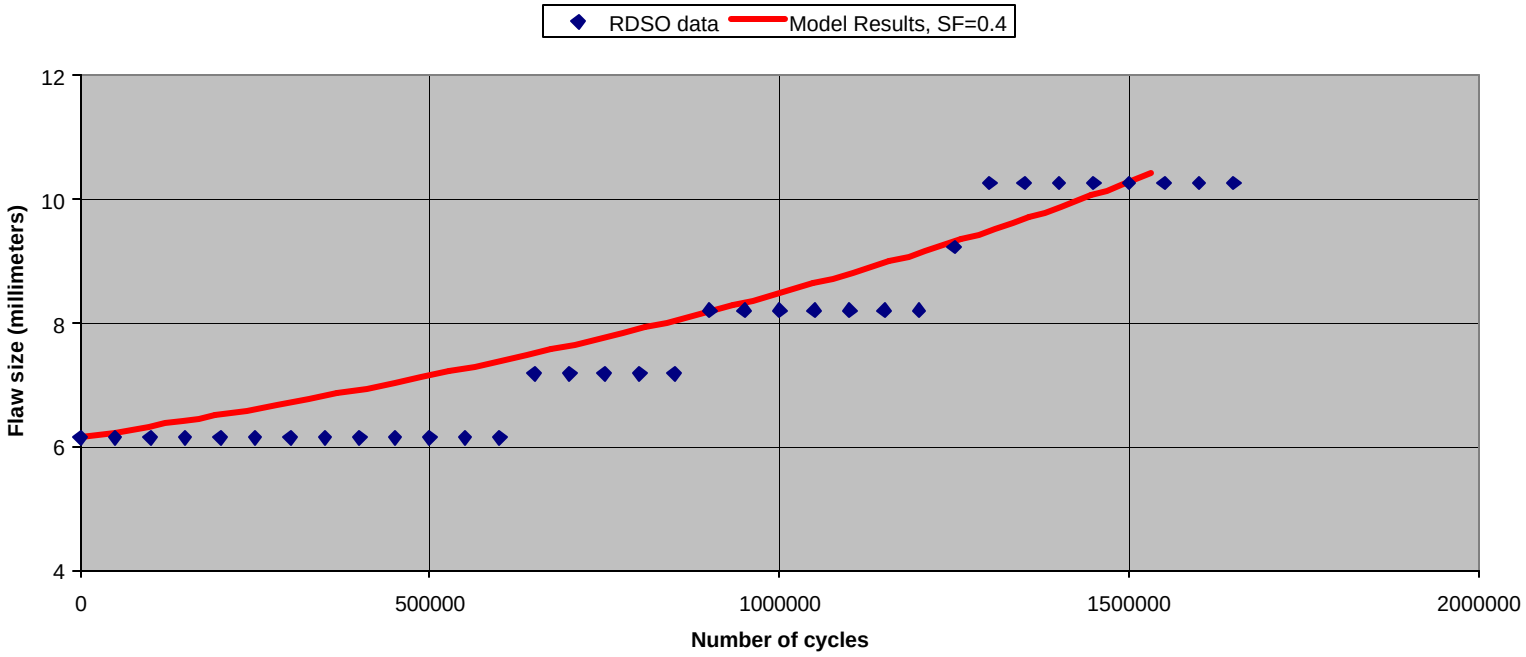

Figure C-17. Correlation between RDSO test data and engineering model results for TL/2002-127 (tache ovale).

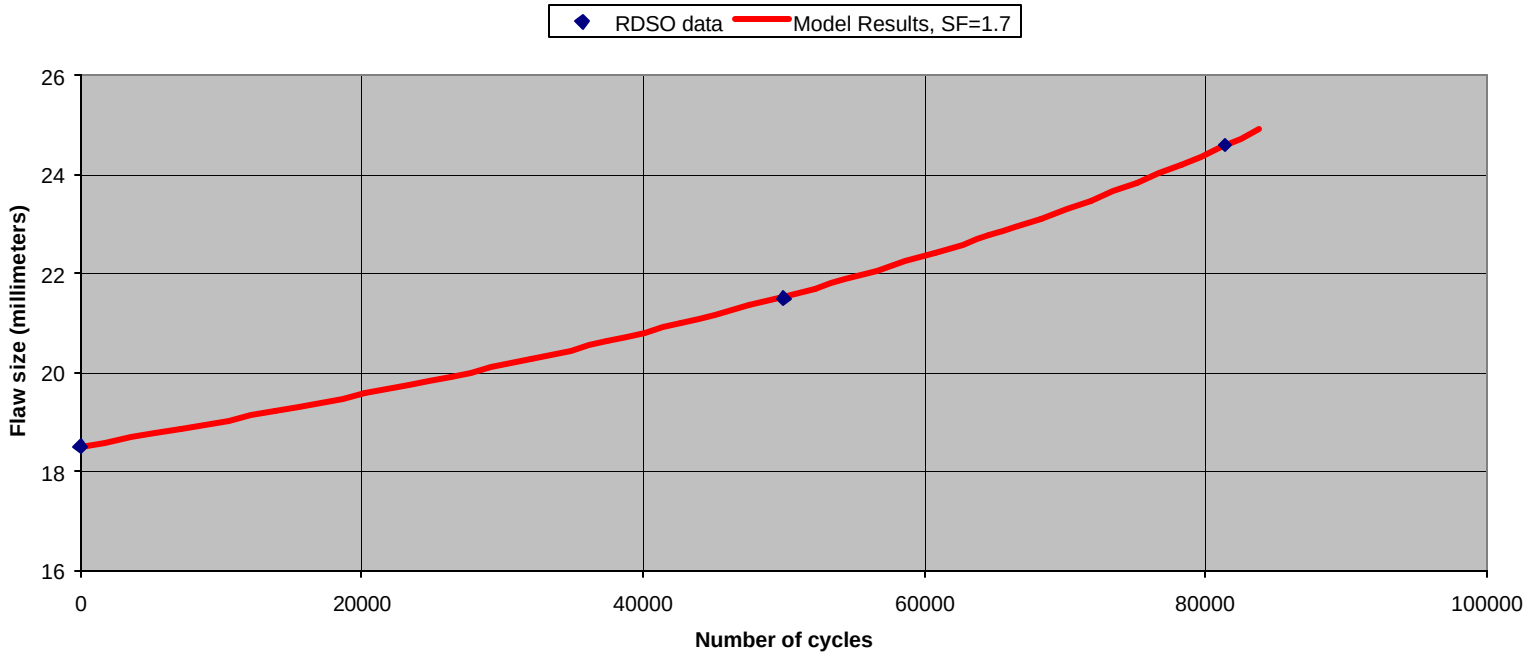

Figure C-18. Correlation between RDSO test data and engineering model results for TL/2002-128 (tache ovale).

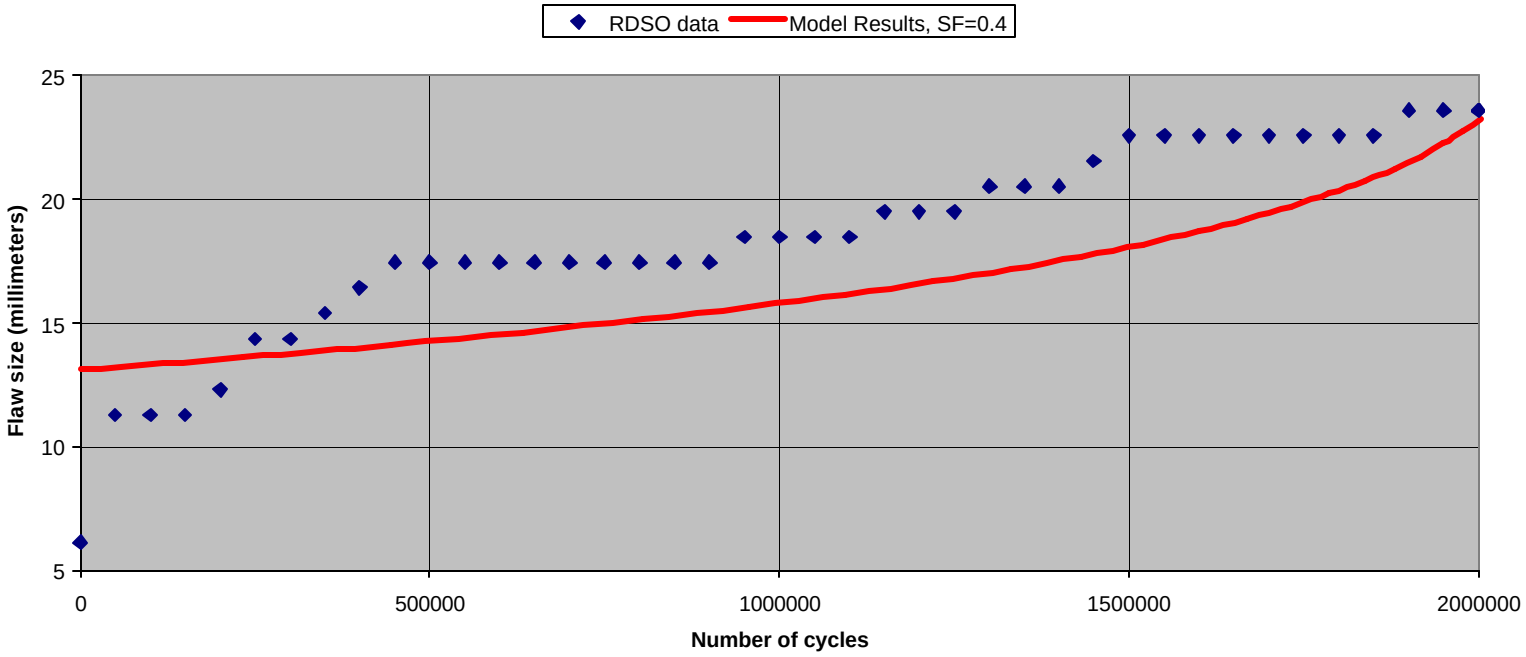

Figure C-19. Correlation between RDSO test data and engineering model results for TL/2002-129 (tache ovale).

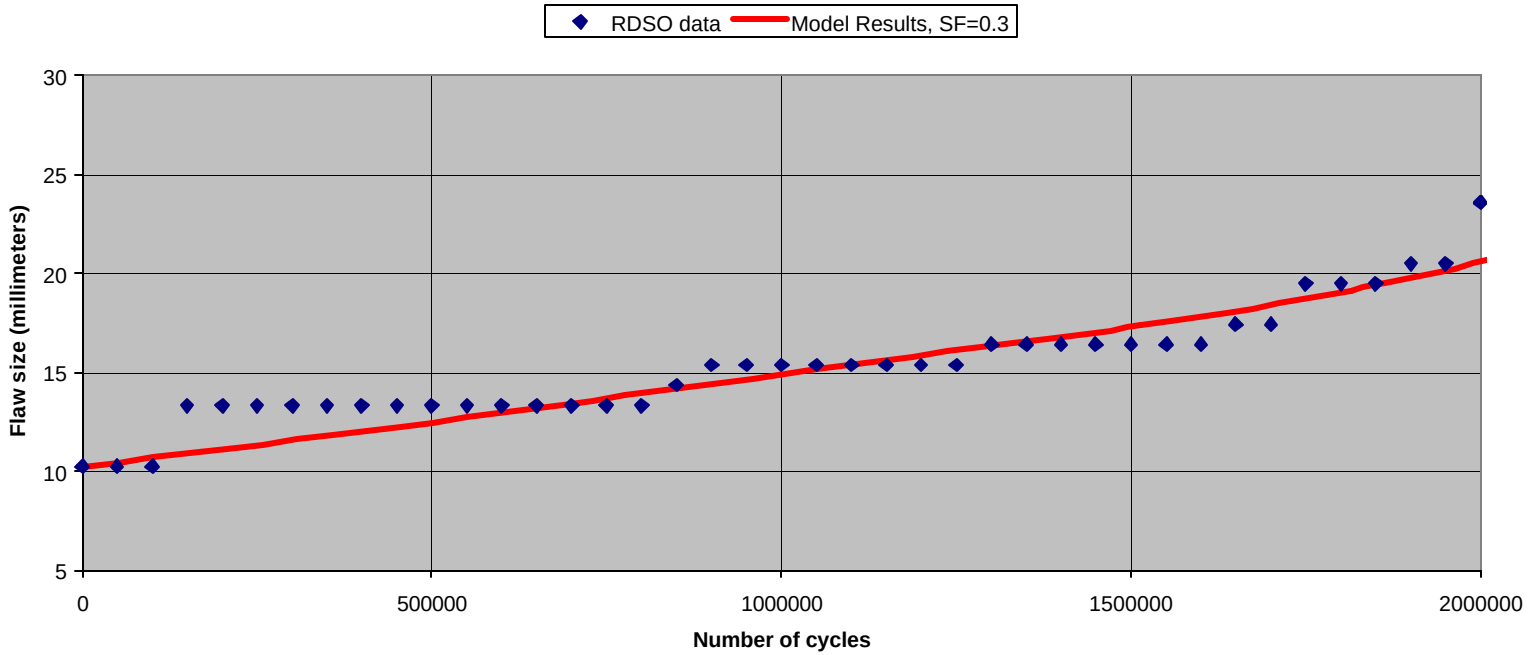

Figure C-20. Correlation between RDSO test data and engineering model results for TL/2002-138 (tache ovale).

APPENDIX D. CORRELATIONS BETWEEN SPOORNET TEST DATA AND RESULTS FROM ENGINEERING ANALYSES

This appendix contains four plots that compare laboratory test data and results from the engineering fracture mechanics analysis model to calculate the growth of internal rail defects. These data were obtained from the Spoornet laboratory test program. In each plot, the solid diamond-shaped symbols represent the laboratory test data and a solid continuous line represents the results from the analysis. In each case, the internal rail defect is assumed to be a tache ovale defect with an aspect ratio of 0.83.

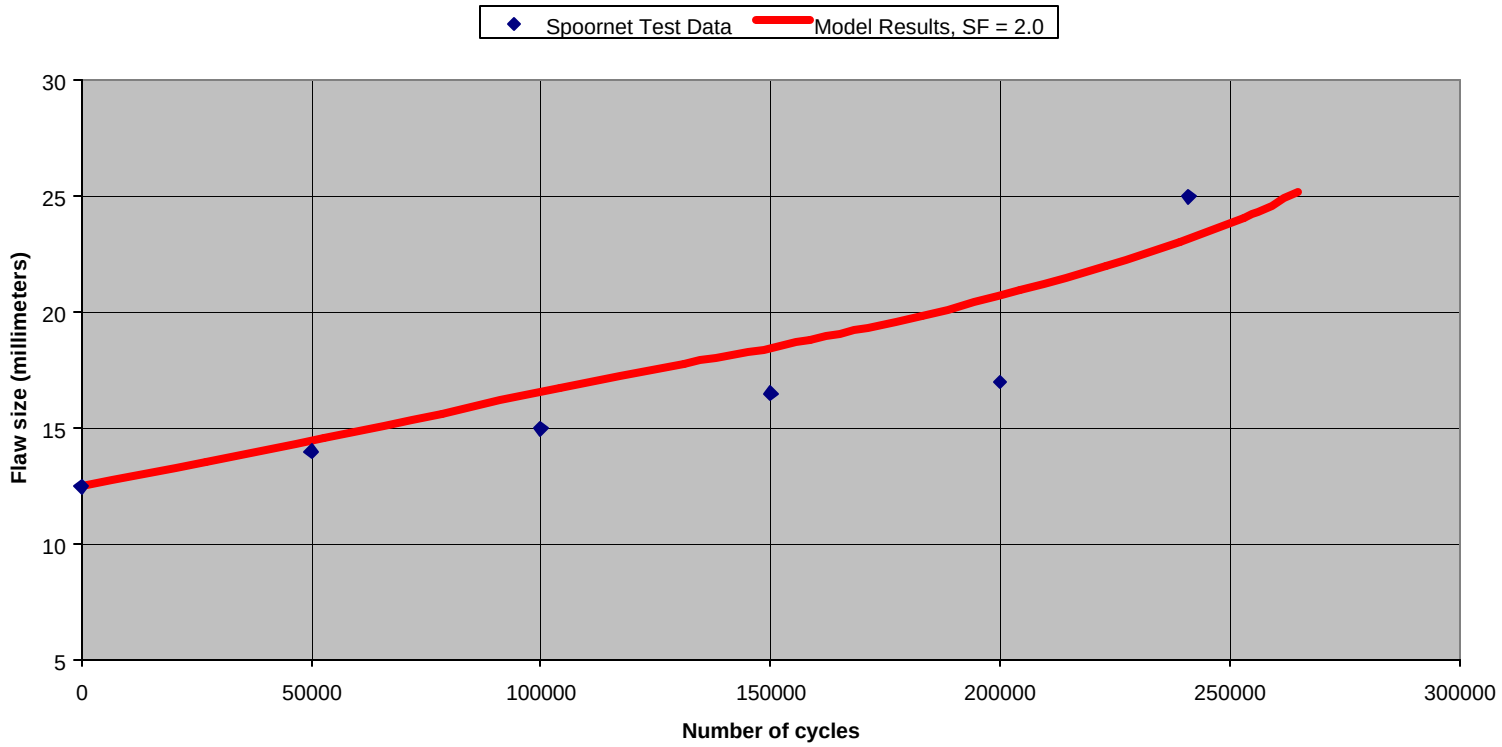

Figure D-1. Correlation between Spoornet test data and engineering model results for Defect Number 1419.

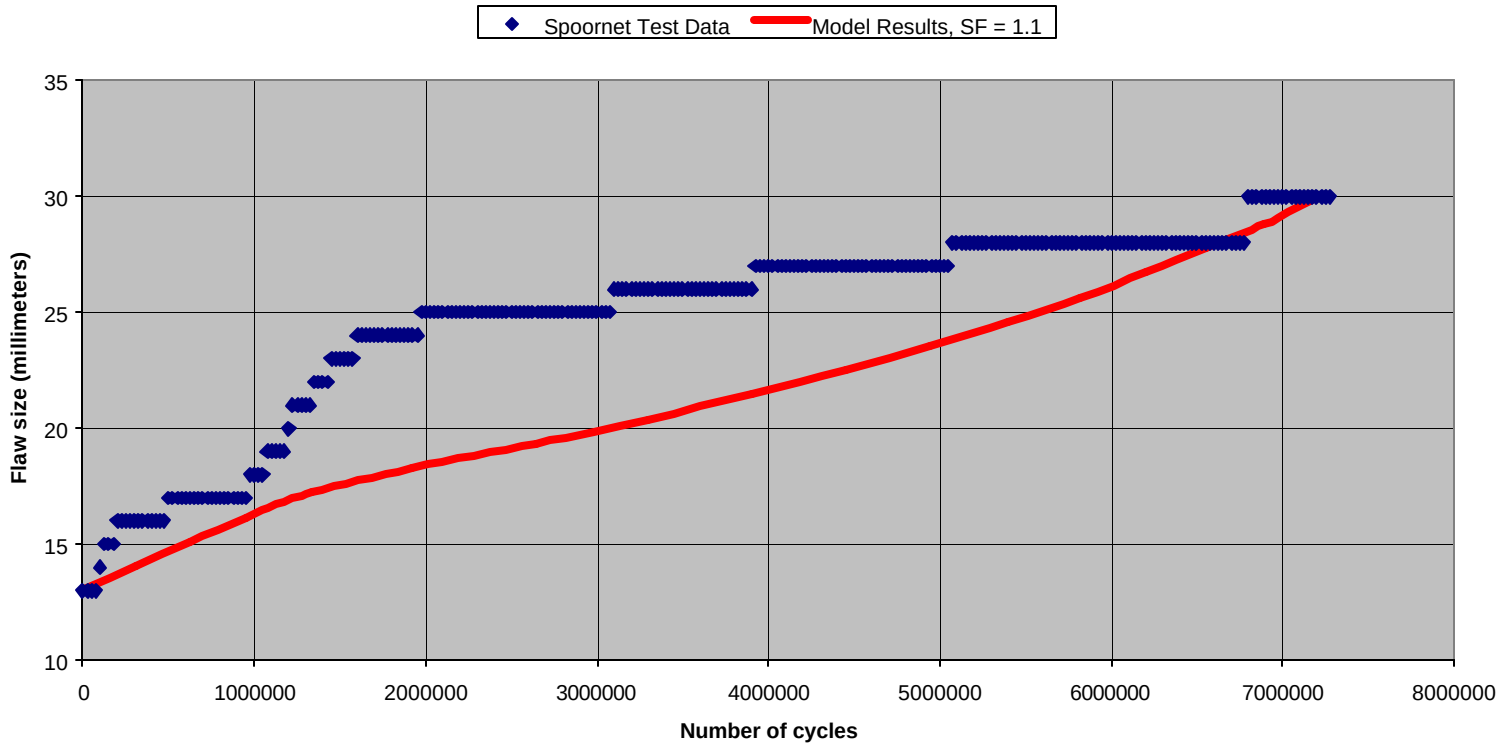

Figure D-2. Correlation between Spoornet test data and engineering model results for Defect Number 1432.

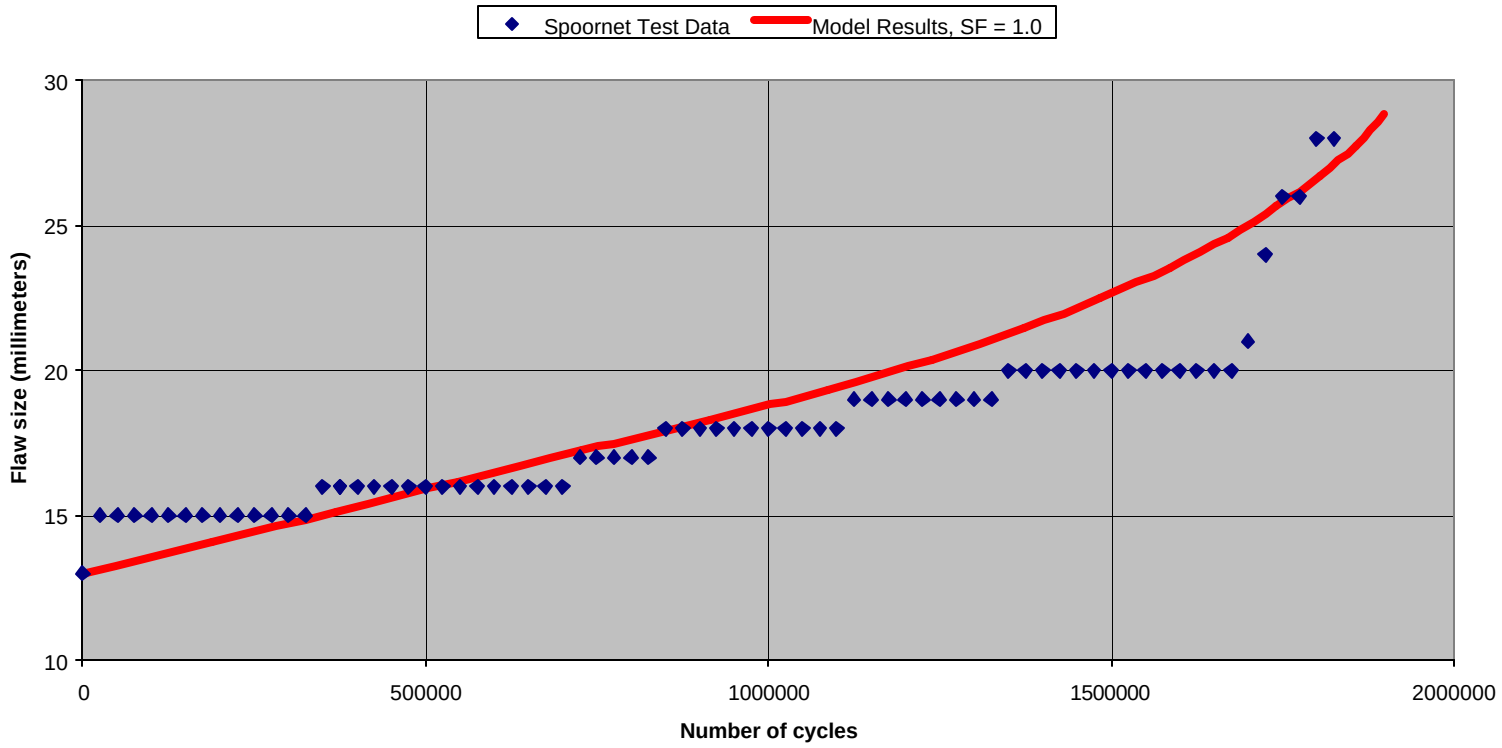

Figure D-3. Correlation between Spoornet test data and engineering model results for Defect Number 1435.

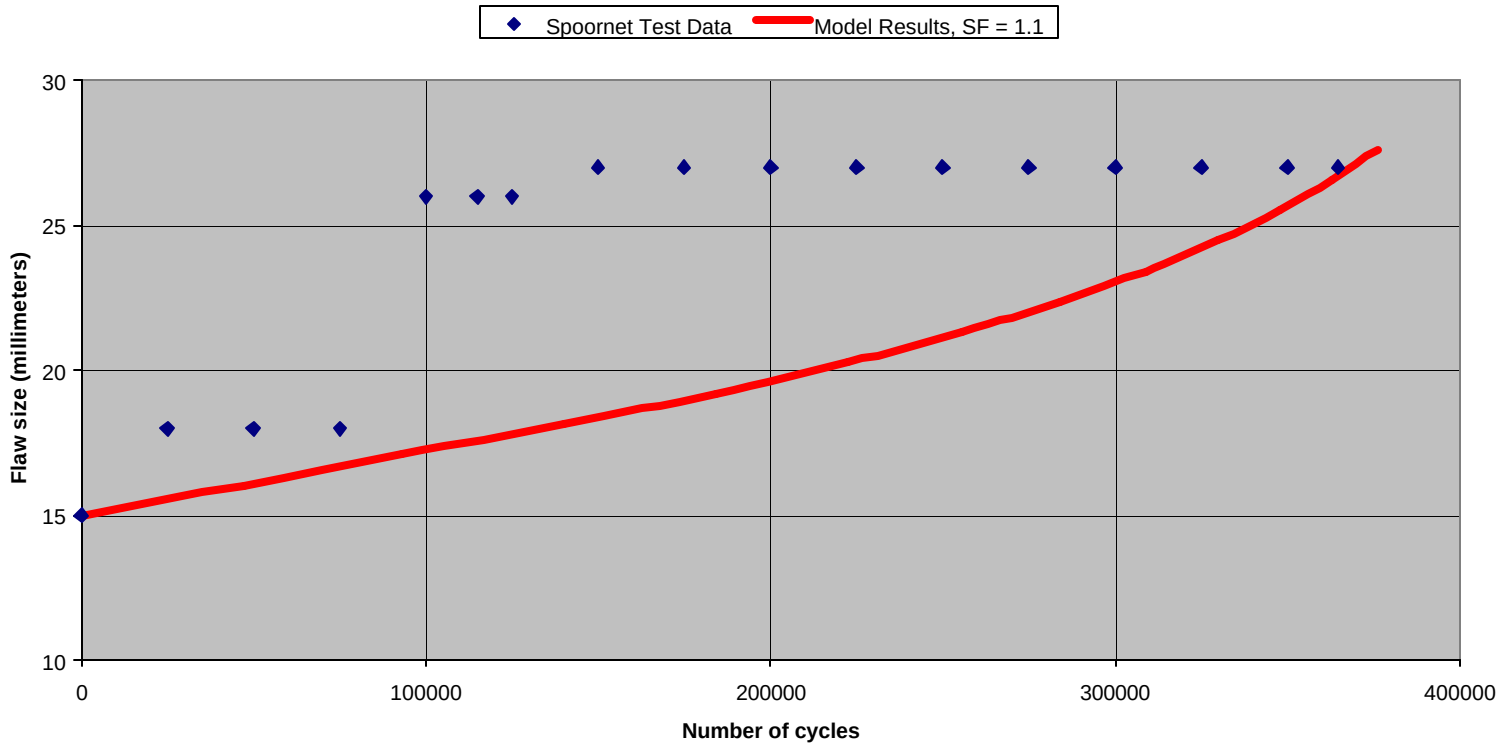

Figure D-4. Correlation between Spoornet test data and engineering model results for Defect Number 1456.

APPENDIX E. MEASUREMENT AND ANALYSIS OF RESIDUAL STRESS

Surface residual stress were measured on 18 rail samples by the Research Designs and Standards Organization (RDSO) of India Railways and on three rail samples by Spoornet in South Africa. Both organizations measured longitudinal residual stresses around the periphery of the rail using an array of strain gauges and a sectioning technique. Each organization used a different number of strain gauges for this purpose. The locations of the strain gauges in the RDSO measurements are shown schematically in Figure E-1, and the strain gauge arrangement used by Spoornet is shown in Figure E-2.

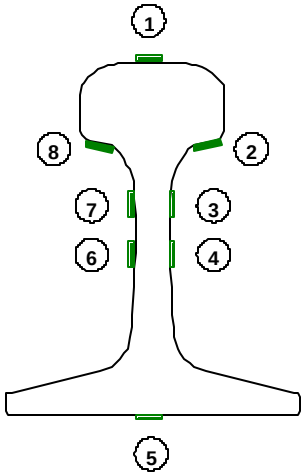

Figure E-1. Strain gauge locations in RDSO residual stress measurements.

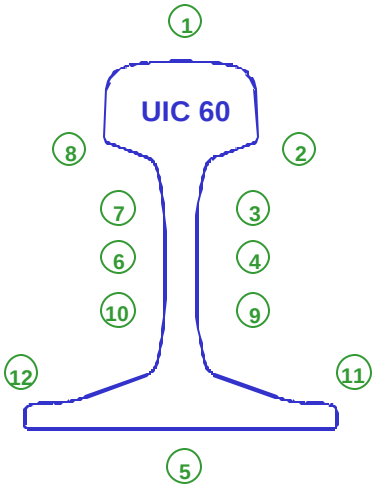

Figure E-2. Strain gauge locations in Spoornet residual stress measurements.

Table E-1 lists the residual stresses at each strain gauge for each rail measured by RDSO. Each of the rail samples listed in the table corresponds to a defect that was monitored for growth during the laboratory testing. The table indicates that the longitudinal residual stress in the base (SG No. 5) of each rail is tensile. In all but four rail samples, the residual stress at the top of the rail (SG No. 1) is compressive.

Table E-2 lists the residual stresses measured at each strain gauge for each rail by Spoornet. The origin of the Spoornet rail samples is unknown. Moreover, these rails do not correspond to any that were tested in either laboratory or revenue service conditions. All rail samples listed in the table were UIC 60 rail sections. Table E-2 indicates that the longitudinal residual stress in the base (also SG No. 5) of each rail is tensile. All three rails in the Spoornet measurements showed compressive residual stress at the top of the rail (SG No. 1).

Engineering analyses were conducted to estimate the distribution of the longitudinal residual stress along the vertical centerline for each rail using the strain gauge measurements on the surface. Mathematically, the residual stress distribution is assumed to be a 3rd – order polynomial or cubic function

$$S_{xx}(z) = b_0 + b_1 z + b_2 z^2 + b_3 z^3 \tag{E.1}$$

where z is the distance from the bottom of the rail. By definition, residual stresses are self-equilibrating so that the resultant force and moment must be zero. Mathematically,

$$F = \int_A S_{xx} dA = 0 \tag{E.2}$$

$$M = \int_A S_{xx} \left(z - z_N \right) dA = 0 \tag{E.3}$$

where z_N is the distance from the bottom of the rail to the location of the neutral axis of the entire rail and A is the cross-sectional area of the entire rail.

Further, the estimated residual stress distribution along the vertical centerline is assumed to be a reasonable representation of the strain gauge data taken from the periphery of the rail. The least squares criterion is applied to find the best-fit curve. Therefore, the sum of the squares of the residuals is expressed mathematically as

$$R = \sum_{i=1}^{N} \left[S_i - S_{xx}(z_i) \right]^2 \tag{E.4}$$

where S_i are the strain gauge measurements for residual stress, z_i are the locations of the strain gauges, and N is the number of strain gauges along the periphery of the rail (8 in the RDSO measurements, 12 in the Spoornet rails).

Table E-1. Summary of RDSO Residual Stress Measurements.

Rail ID	Rail Section	Strain Gauge Measurement for Residual Stress (in ksi)							
		1	2	3	4	5	6	7	8
TL/2000-11	JIS 60	-12.0	-15.4	-10.1	-11.5	43.7	-11.6	-8.6	-11.2
TL/2000-12	JIS 60	-2.3	-4.7	-7.1	-13.8	32.4	-12.8	-5.9	-0.4
TL/2000-22	IRS 52	13.1	-7.7	-7.6	-7.9	23.9	-10.1	-8.4	-10.2
TL/2001-9	IRS 52	-8.7	-0.4	-4.5	-6.2	18.2	-3.6	-4.4	-3.0
TL/2001-14	UIC 60	-7.2	-0.2	-3.7	-6.8	30.9	-5.5	-2.9	0.6
TL/2001-19	IRS 52	-9.4	2.6	-6.4	-7.0	21.3	-5.1	-5.4	-6.4
TL/2001-31	JIS 50	-2.0	-2.0	-9.8	-13.2	22.3	-13.8	-8.8	0.8
TL/2001-54	JIS 50	1.7	-5.4	-6.2	-7.3	16.9	-7.8	-6.7	-4.2
TL/2001-55	JIS 50	1.9	-5.9	-11.0	-15.4	26.3	-14.5	-9.7	-3.1
TL/2001-56	JIS 50	-1.7	-1.6	-8.5	-12.9	24.1	-13.4	-9.7	-4.7
TL/2001-67	JIS 50	-0.5	6.9	-16.4	5.3	24.2	-33.5	-6.3	-16.8
TL/2001-68	136 RE	-7.9	-3.9	-8.3	-21.5	40.3	-21.2	-8.8	-5.2
TL/2001-103	136 RE	5.5	2.8	-1.1	-16.2	28.2	-19.2	-0.8	1.2
TL/2001-104	136 RE	-0.7	-1.4	-6.8	-20.2	34.7	-18.5	-7.9	-4.7
TL/2002-127	UIC 60	-12.6	-0.7	-12.1	-20.6	60.9	-24.7	-14.1	-2.5
TL/2002-128	UIC 60	-12.4	-0.4	-13.4	-27.9	45.1	-25.2	-15.3	-1.3
TL/2002-129	UIC 60	-6.8	3.7	-11.1	-26.1	44.9	-24.5	-17.5	-10.4
TL/2002-138	UIC 60	-16.7	-2.2	-7.1	-16.4	31.9	-15.9	-7.5	-2.2

Table E-2. Summary of Spoornet Residual Stress Measurements.

Rail ID	Strain Gauge Measurement for Residual Stress (in ksi)											
	1	2	3	4	5	6	7	8	9	10	11	12
1	-23.5	-8.1	-13.6	-25.3	48.1	-25.1	-8.3	-2.2	-10.5	-13.7	-17.0	-21.0
2	-31.8	4.0	-7.7	-21.3	35.4	-21.1	-11.6	-2.1	-7.2	-7.7	-24.5	-17.4
3	-36.2	8.3	-8.4	-27.7	48.5	-27.9	-15.1	-3.8	-11.1	-8.2	-26.9	-19.6

+ = Tension – = Compression

Moreover, the coefficients in the residual stress distribution curve; i.e., the b_i's in equation (E.1); are determined by solving a constrained optimization problem where equation (E.4), defined as the objective function, is minimized subject to satisfying the conditions of static equilibrium defined in equations (E.2) and (E.3).

The results of applying the optimization procedure to estimate the longitudinal residual stress distribution for each rail are shown in Figures E-3 to E-20 for the RDSO measurements, and in Figures E-21 to E-23 for the Spoornet measurements.

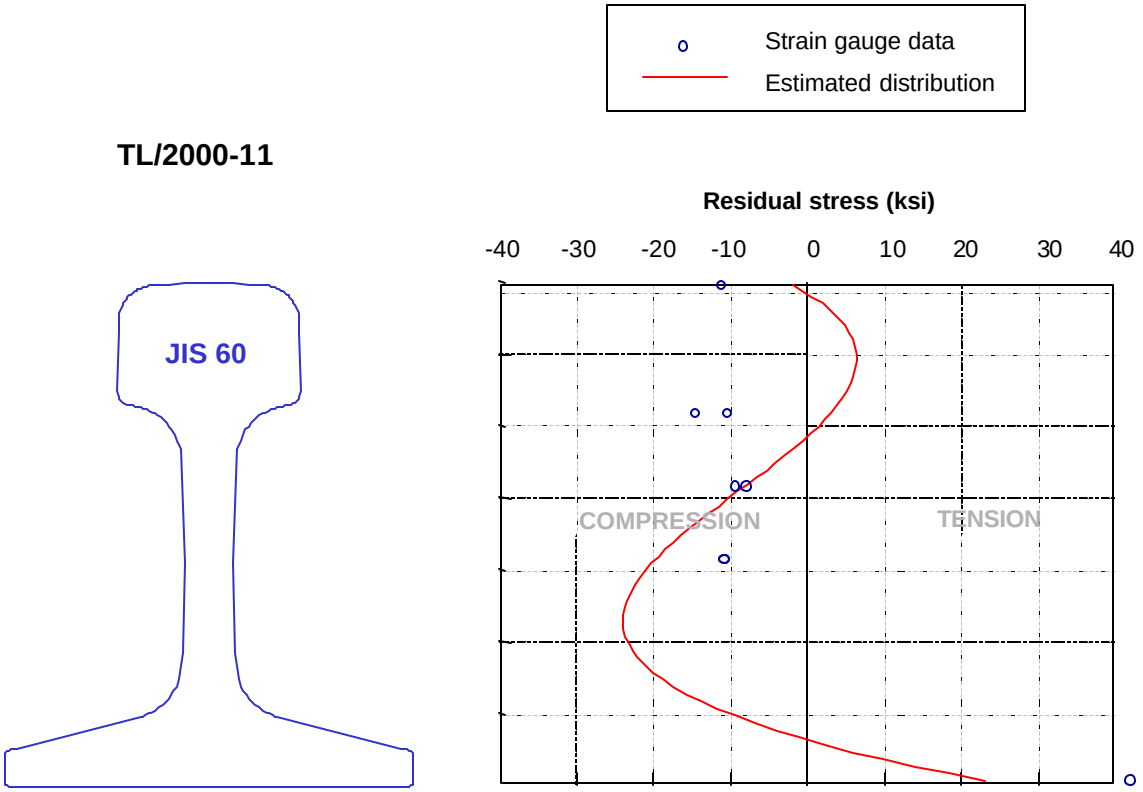

Figure E-3. Reconstruction of longitudinal residual stress distribution for TL/2000-11.

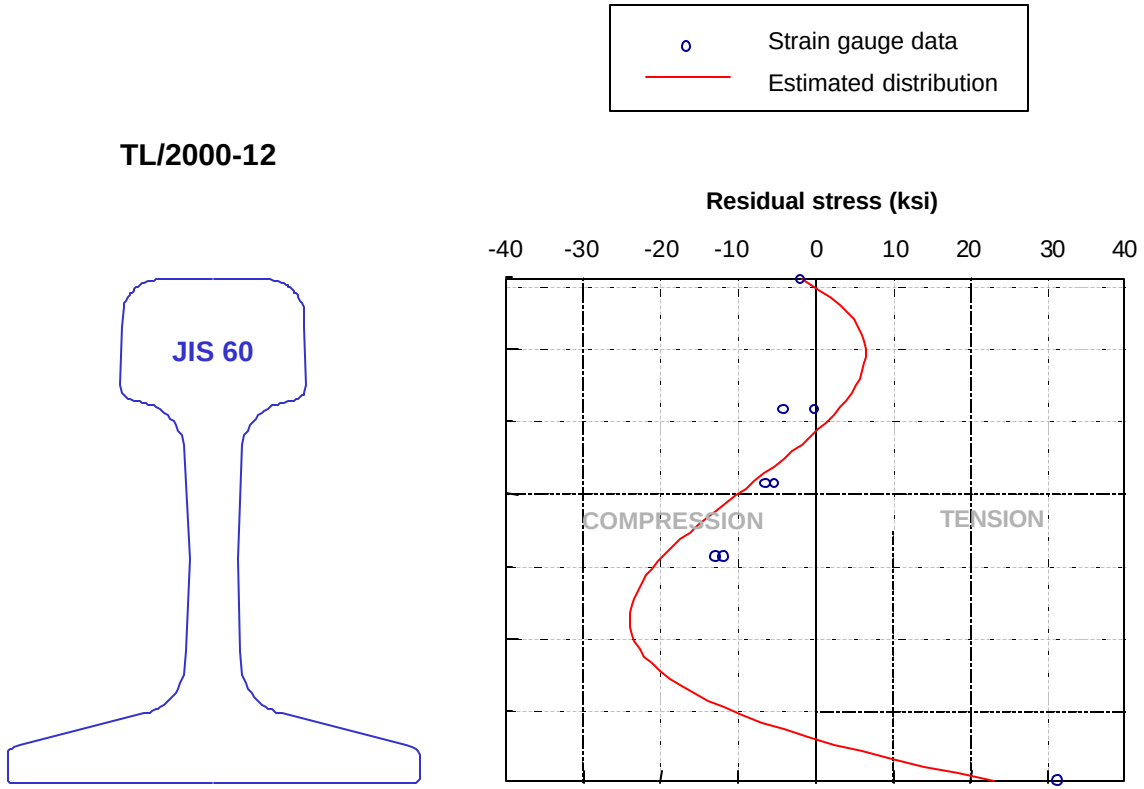

Figure E-4. Reconstruction of longitudinal residual stress distribution for TL/2000-12.

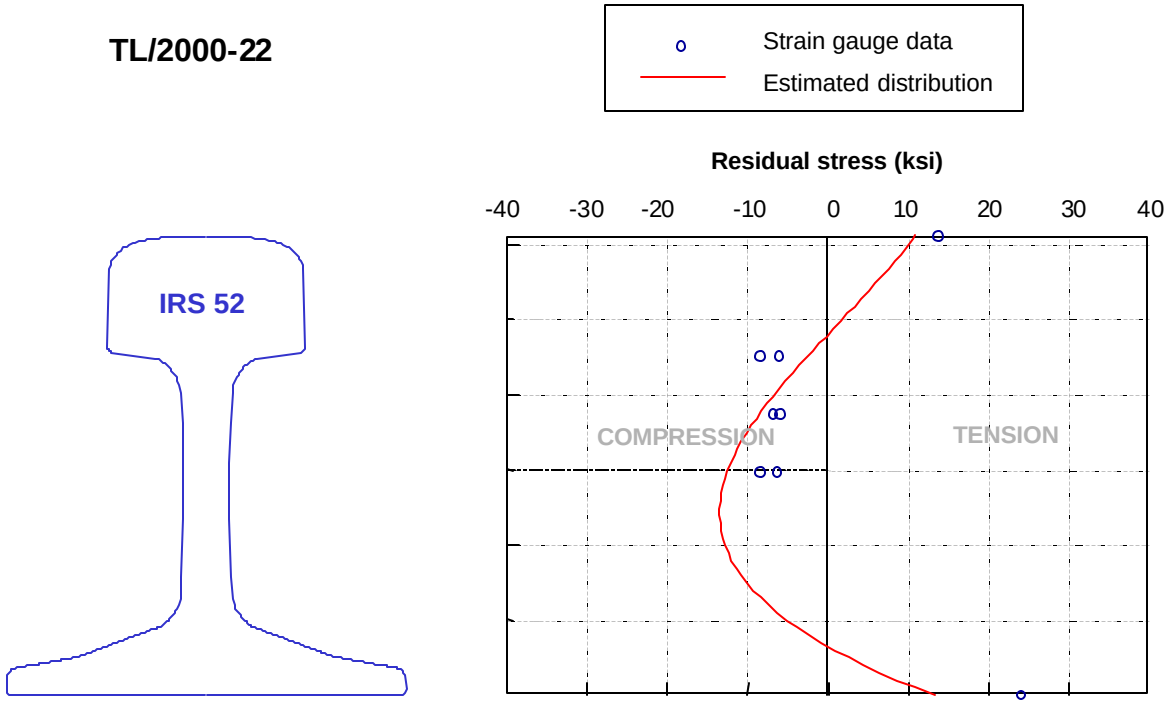

Figure E-5. Reconstruction of longitudinal residual stress distribution for TL/2000-22.

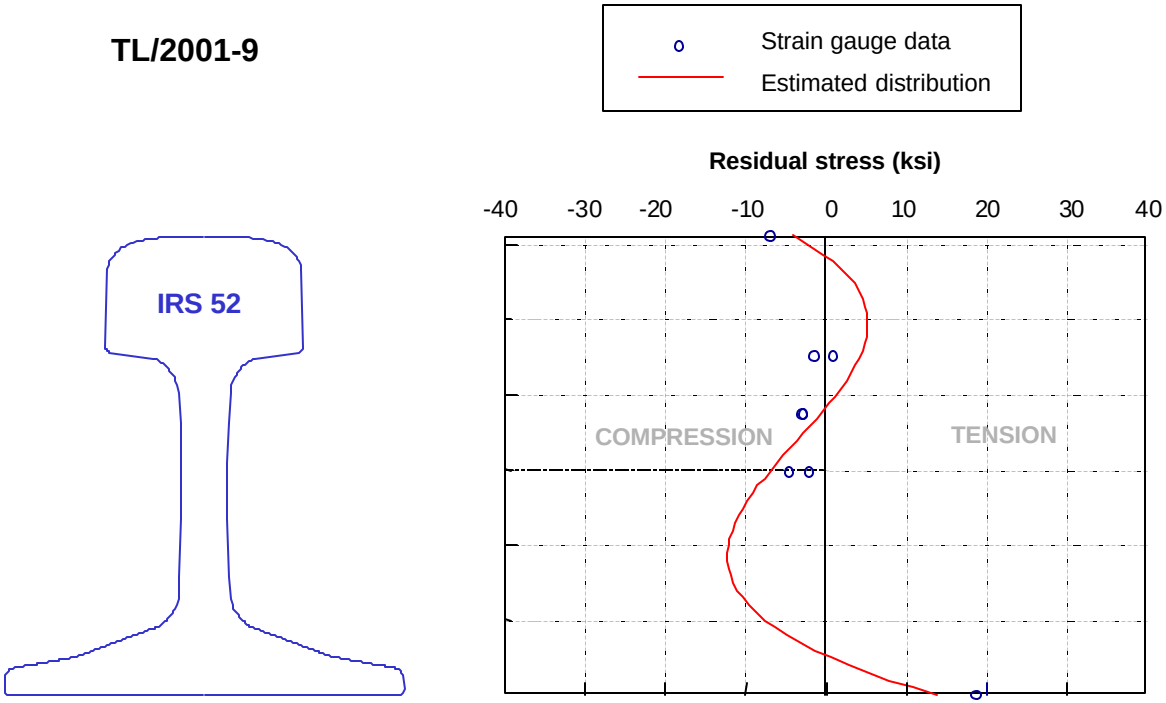

Figure E-6. Reconstruction of longitudinal residual stress distribution for TL/2001-9.

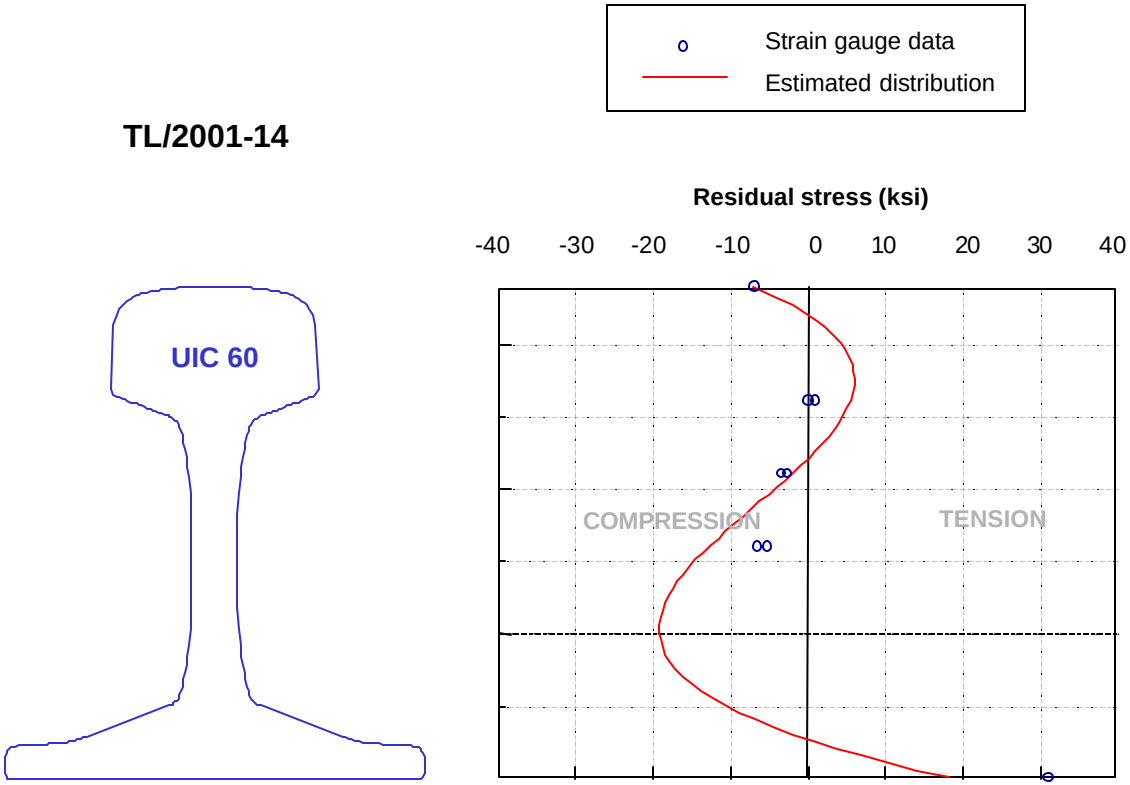

Figure E-7. Reconstruction of longitudinal residual stress distribution for TL/2001-14.

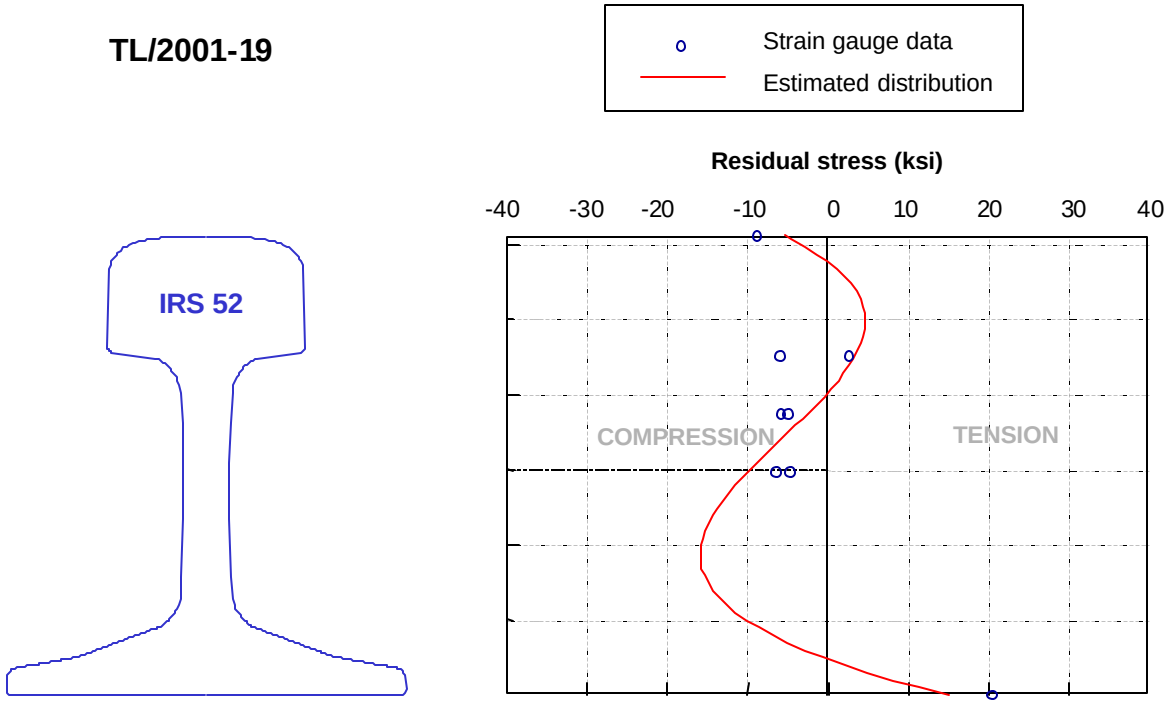

Figure E-8. Reconstruction of longitudinal residual stress distribution for TL/2001-19.

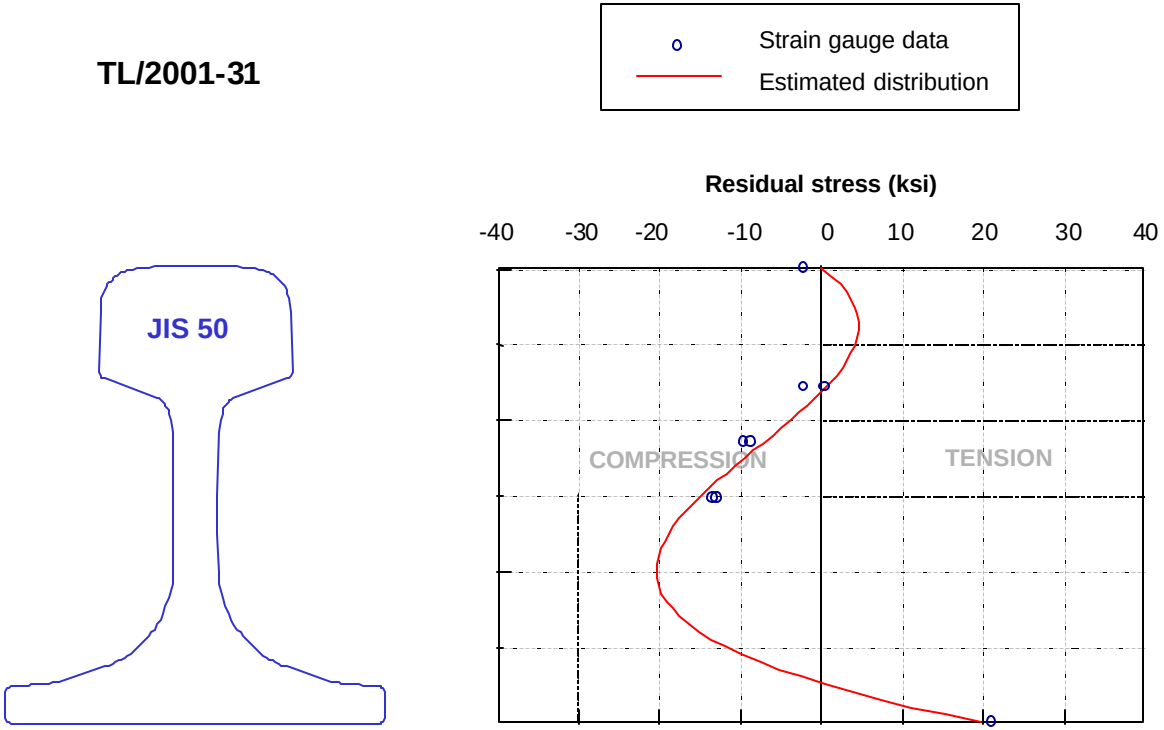

Figure E-9. Reconstruction of longitudinal residual stress distribution for TL/2001-31.

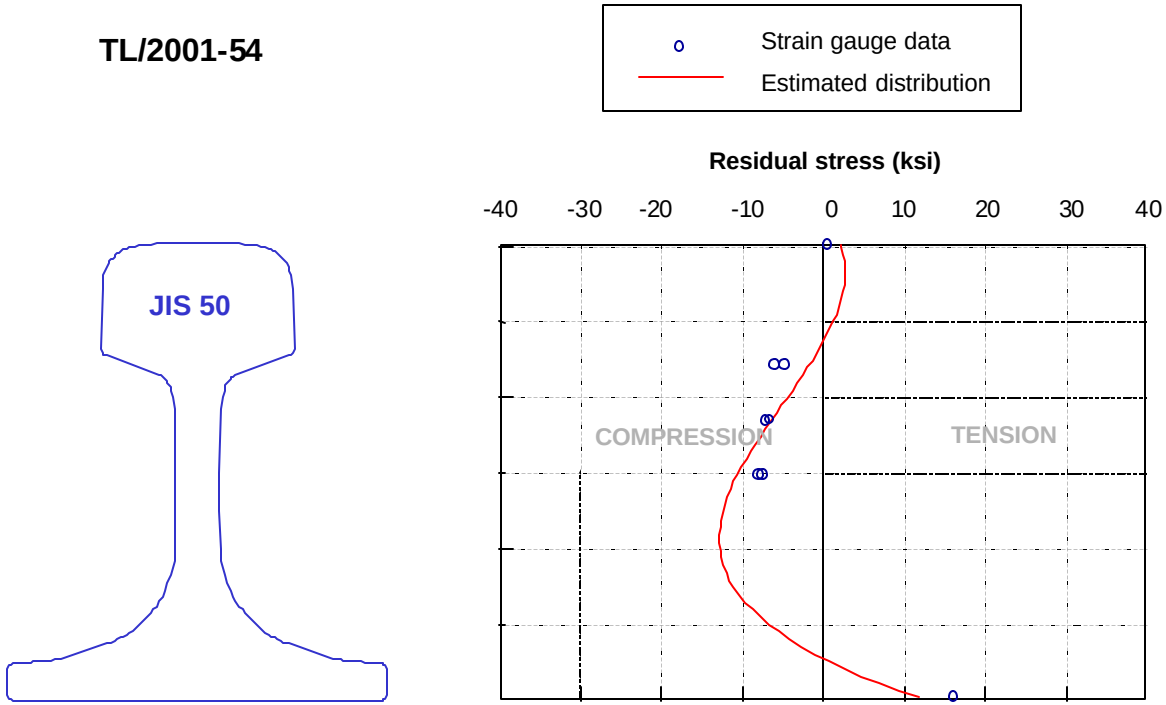

Figure E-10. Reconstruction of longitudinal residual stress distribution for TL/2001-54.

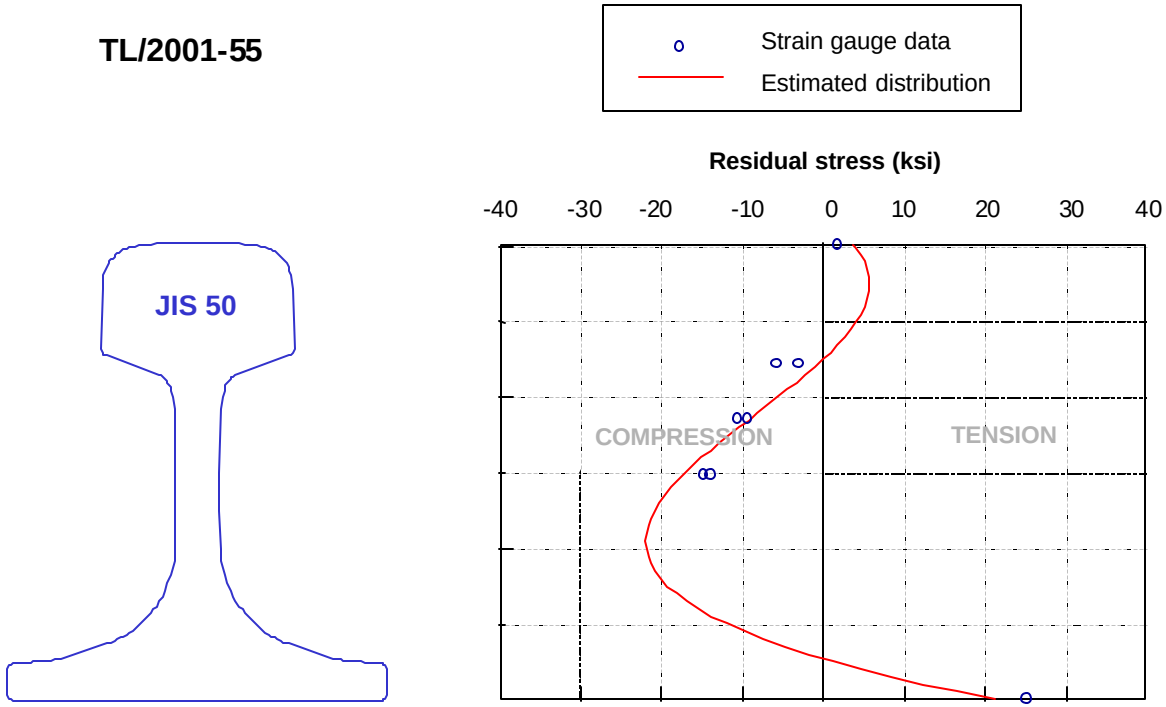

Figure E-11. Reconstruction of longitudinal residual stress distribution for TL/2001-55.

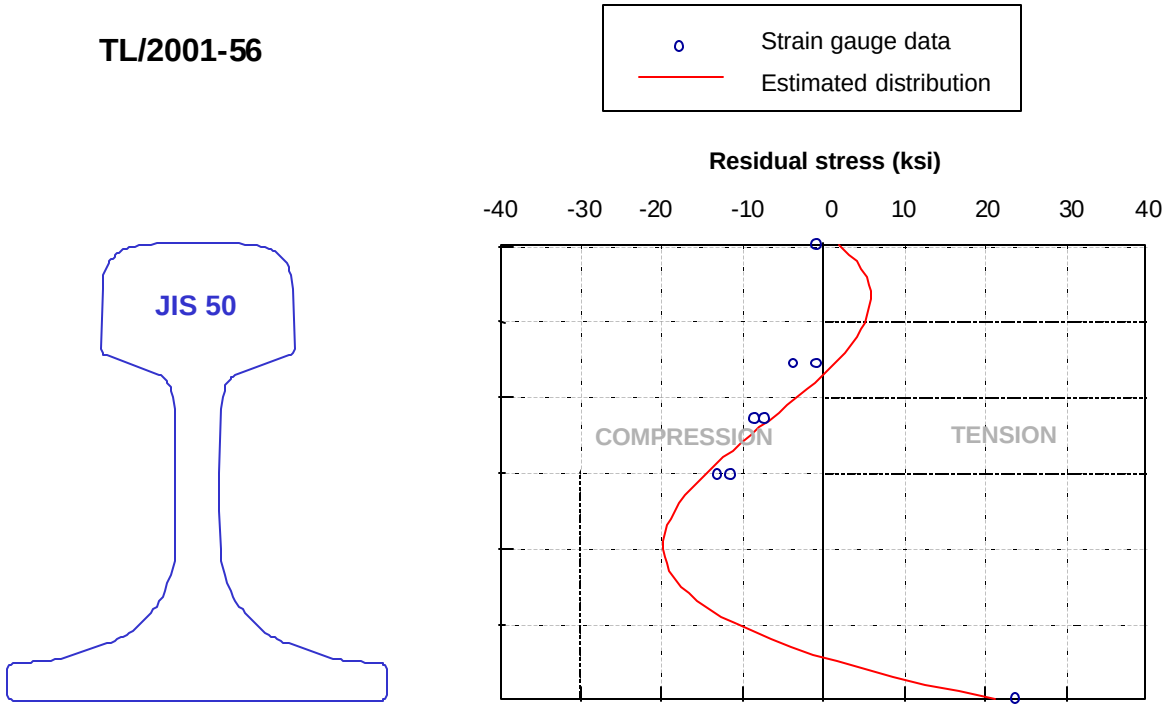

Figure E-12. Reconstruction of longitudinal residual stress distribution for TL/2001-56.

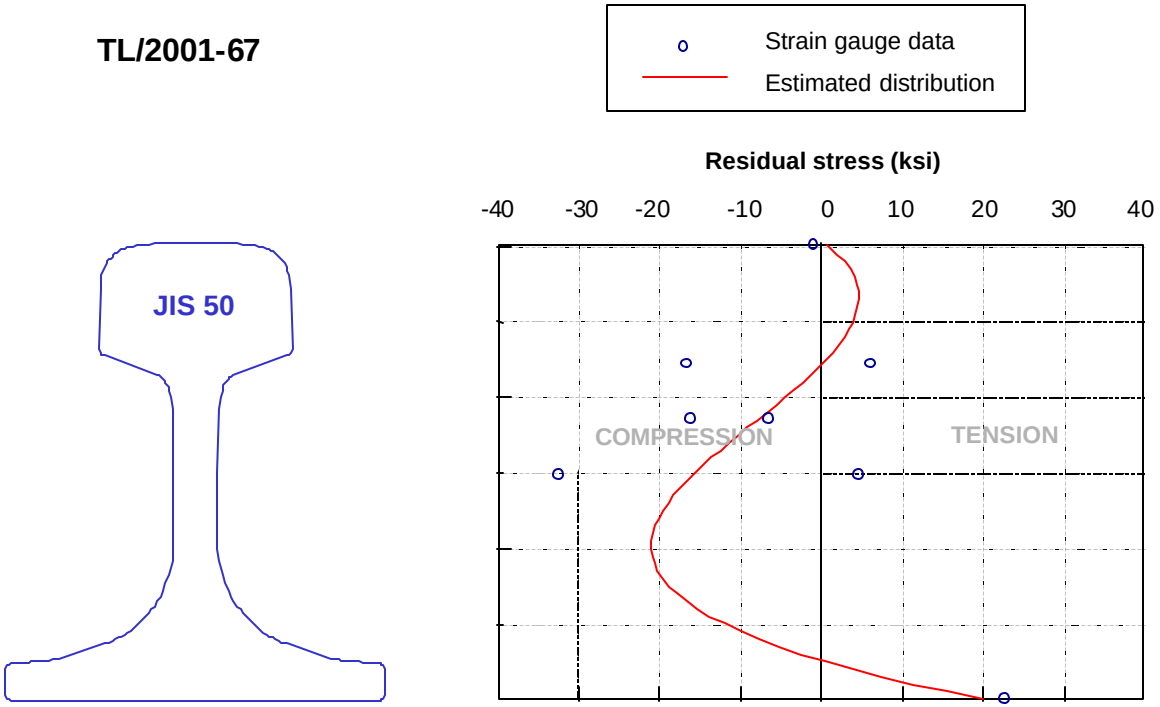

Figure E-13. Reconstruction of longitudinal residual stress distribution for TL/2001-67.

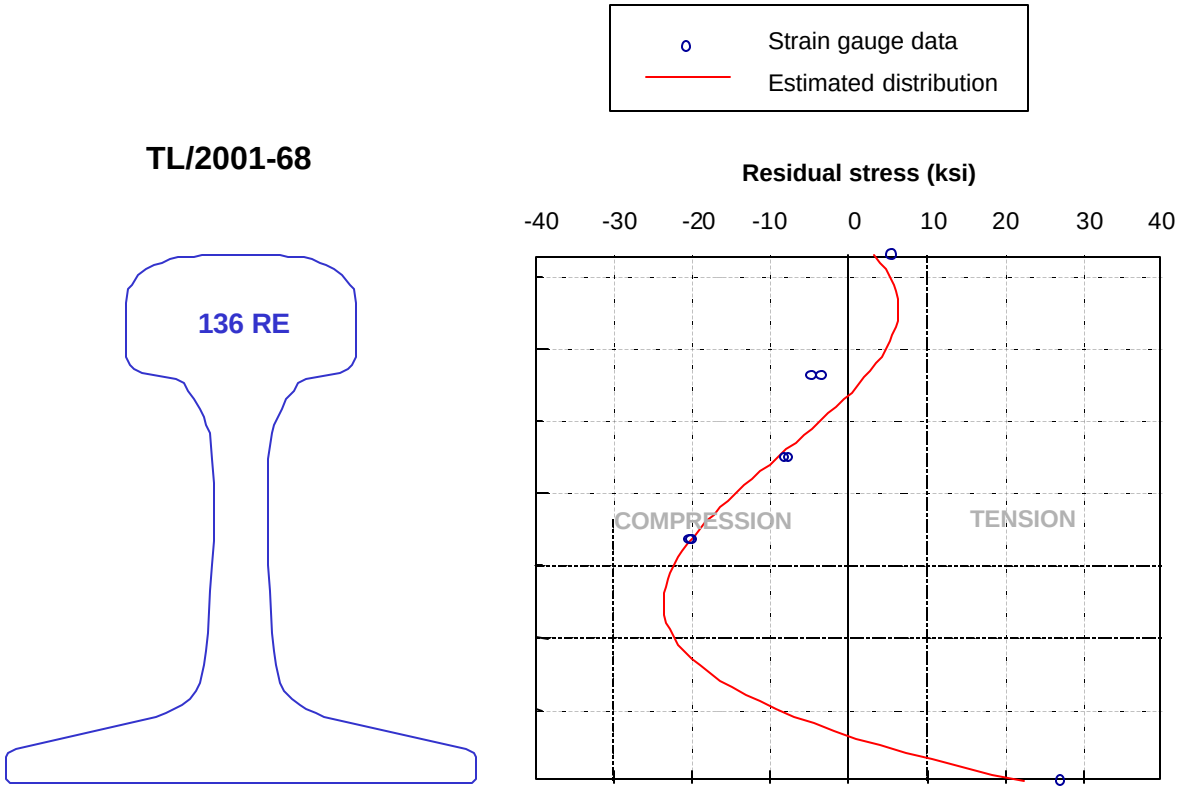

Figure E-14. Reconstruction of longitudinal residual stress distribution for TL/2001-68.

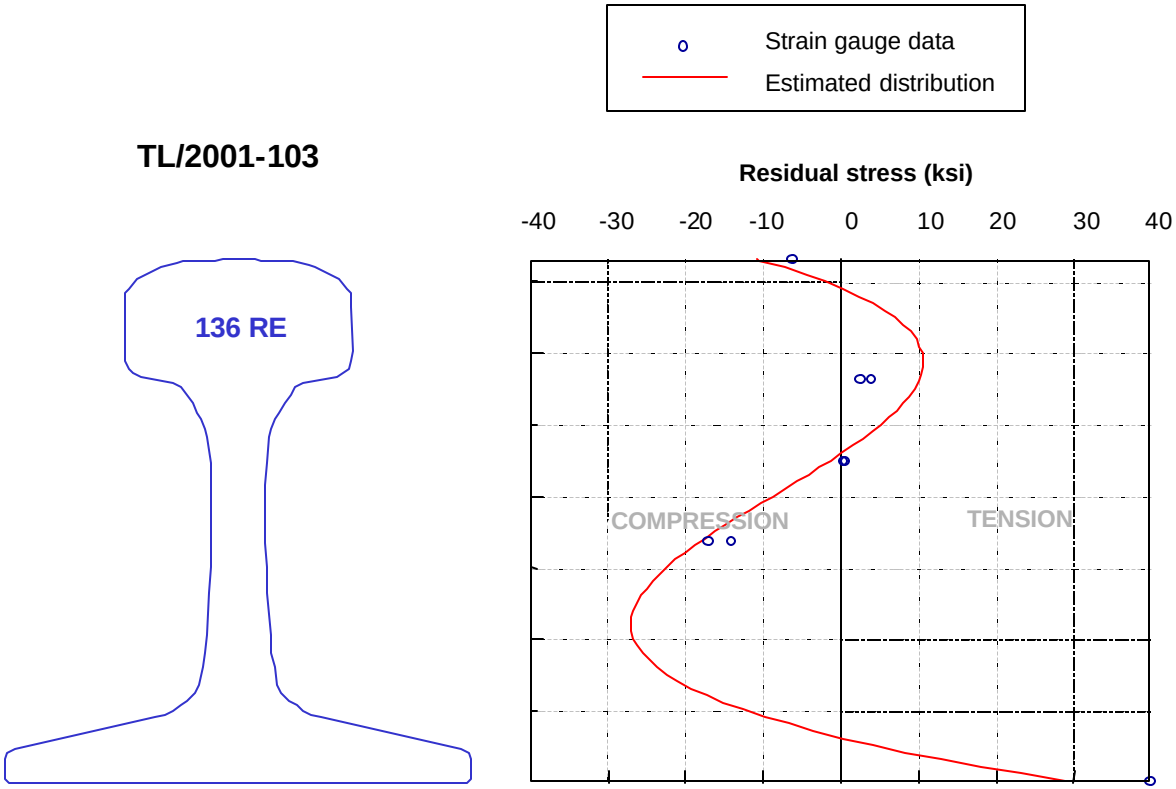

Figure E-15. Reconstruction of longitudinal residual stress distribution for TL/2001-103.

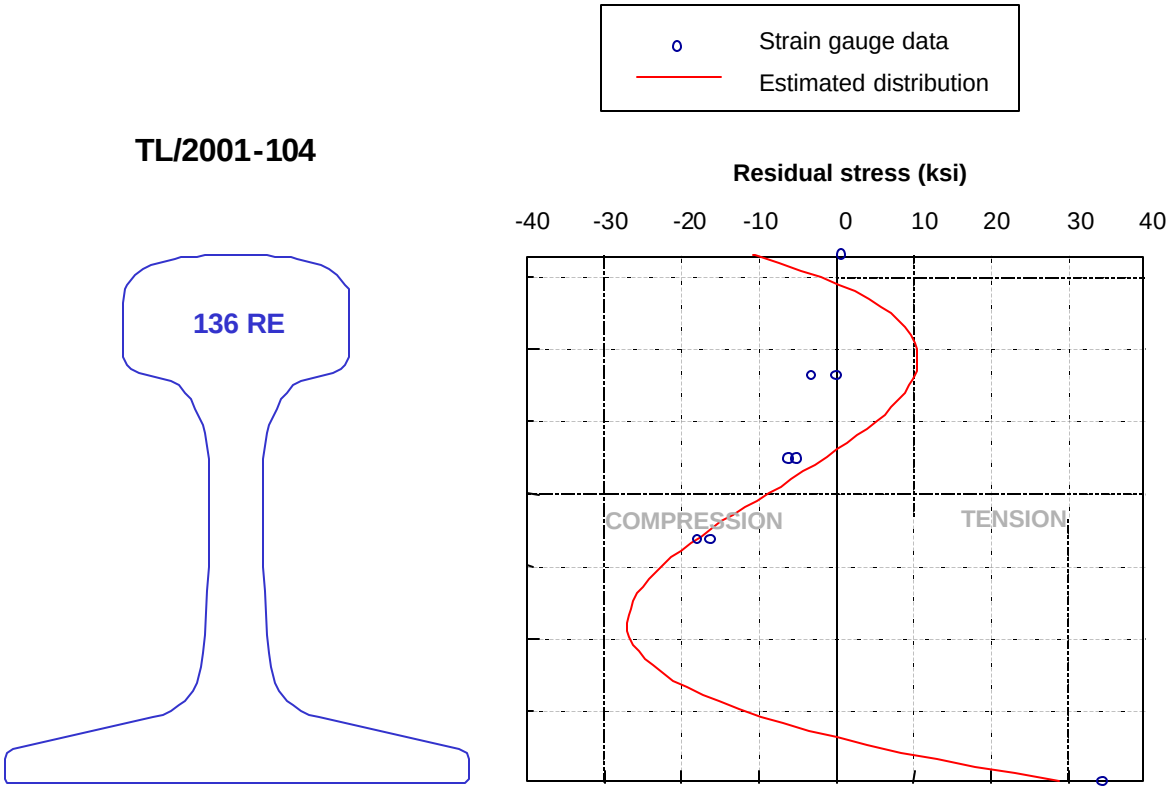

Figure E-16. Reconstruction of longitudinal residual stress distribution for TL/2001-104.

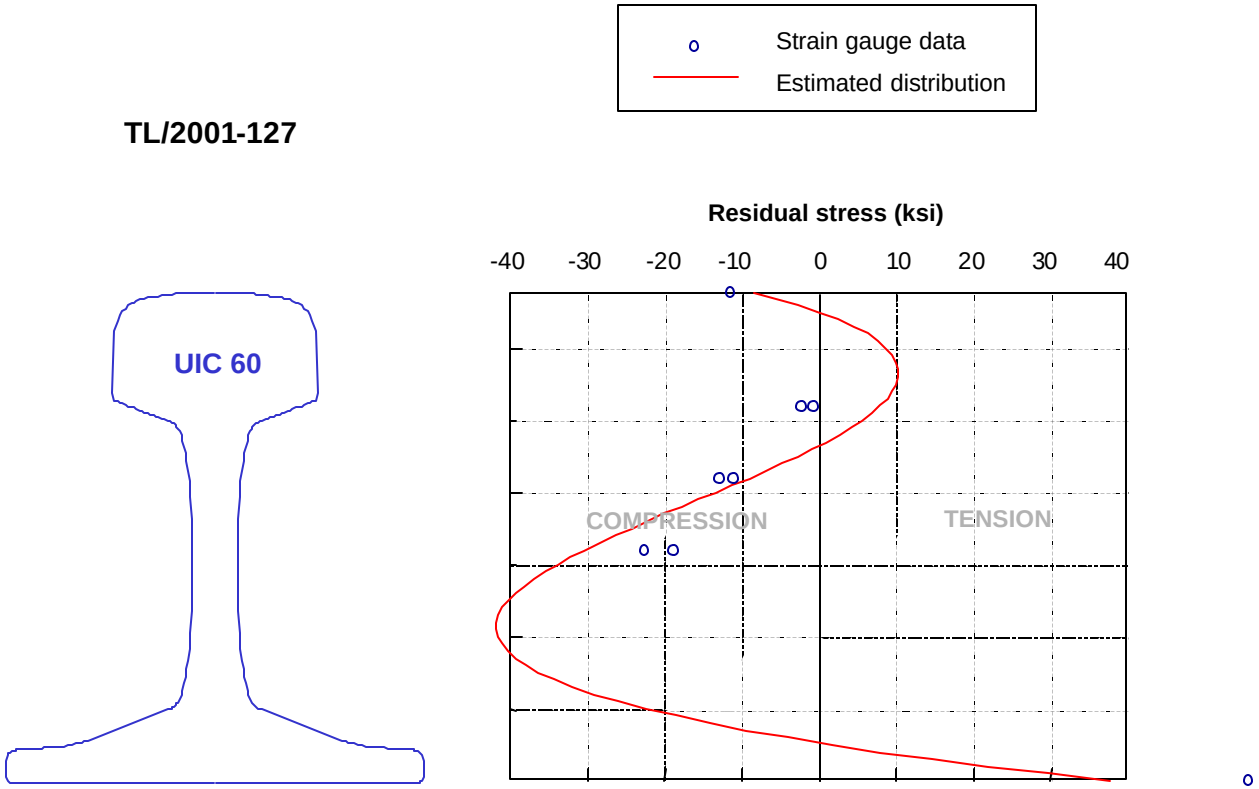

Figure E-17. Reconstruction of longitudinal residual stress distribution for TL/2002-127.

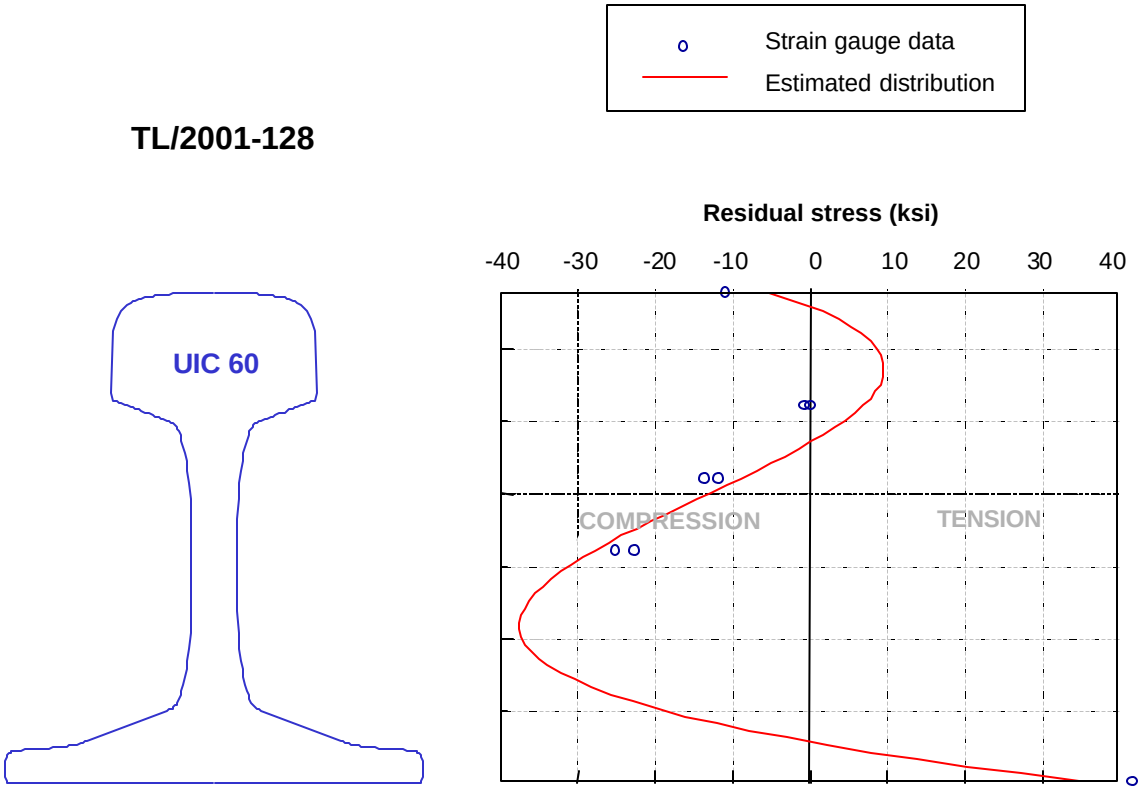

Figure E-18. Reconstruction of longitudinal residual stress distribution for TL/2002-128.

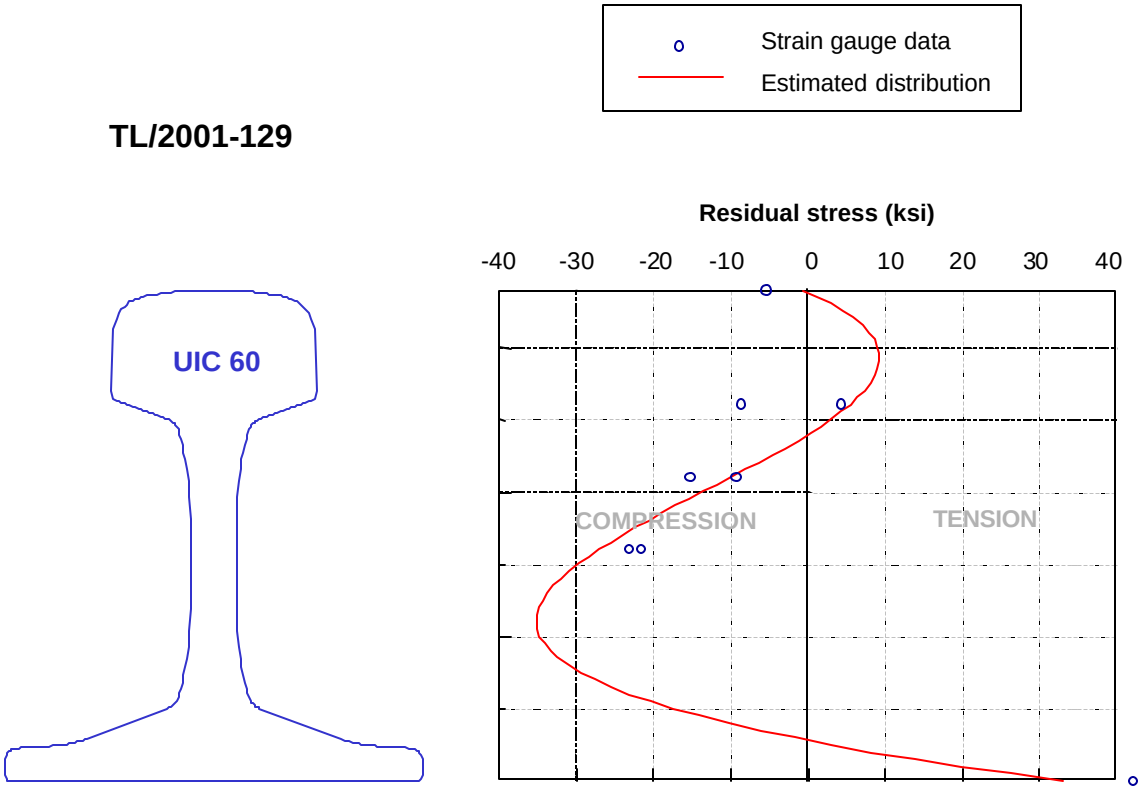

Figure E-19. Reconstruction of longitudinal residual stress distribution for TL/2002-129.

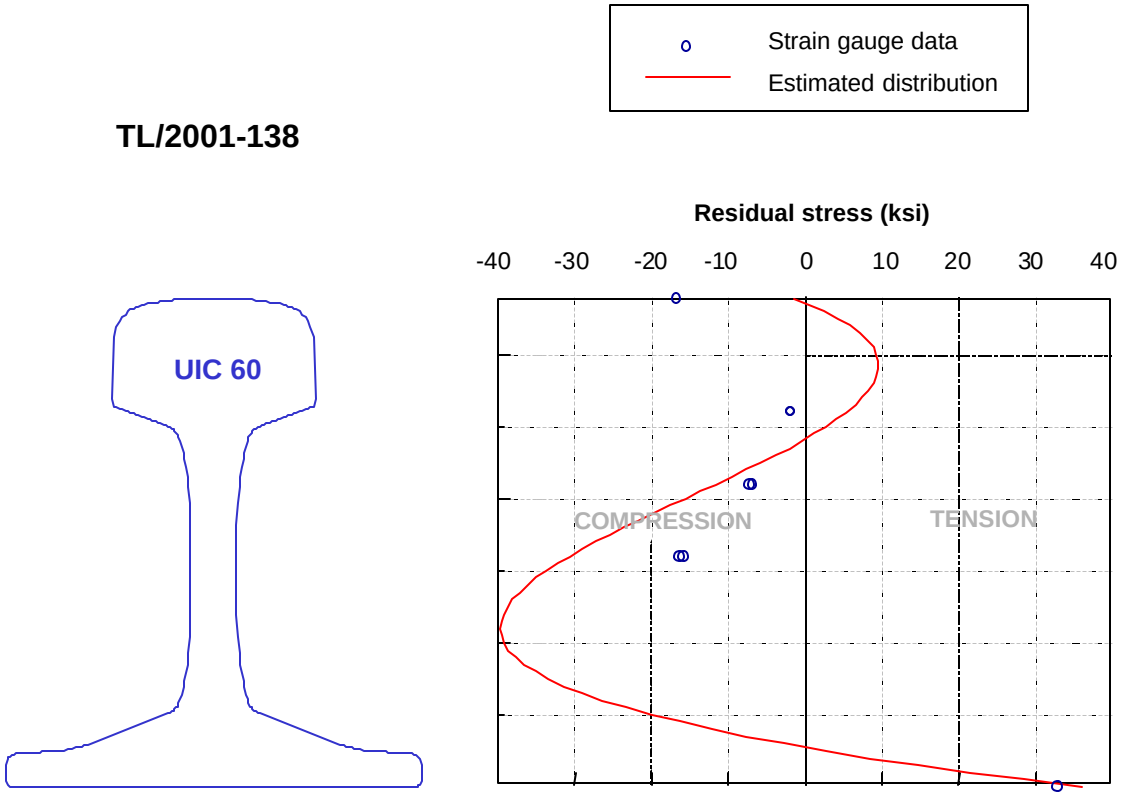

Figure E-20. Reconstruction of longitudinal residual stress distribution for TL/2002-138.

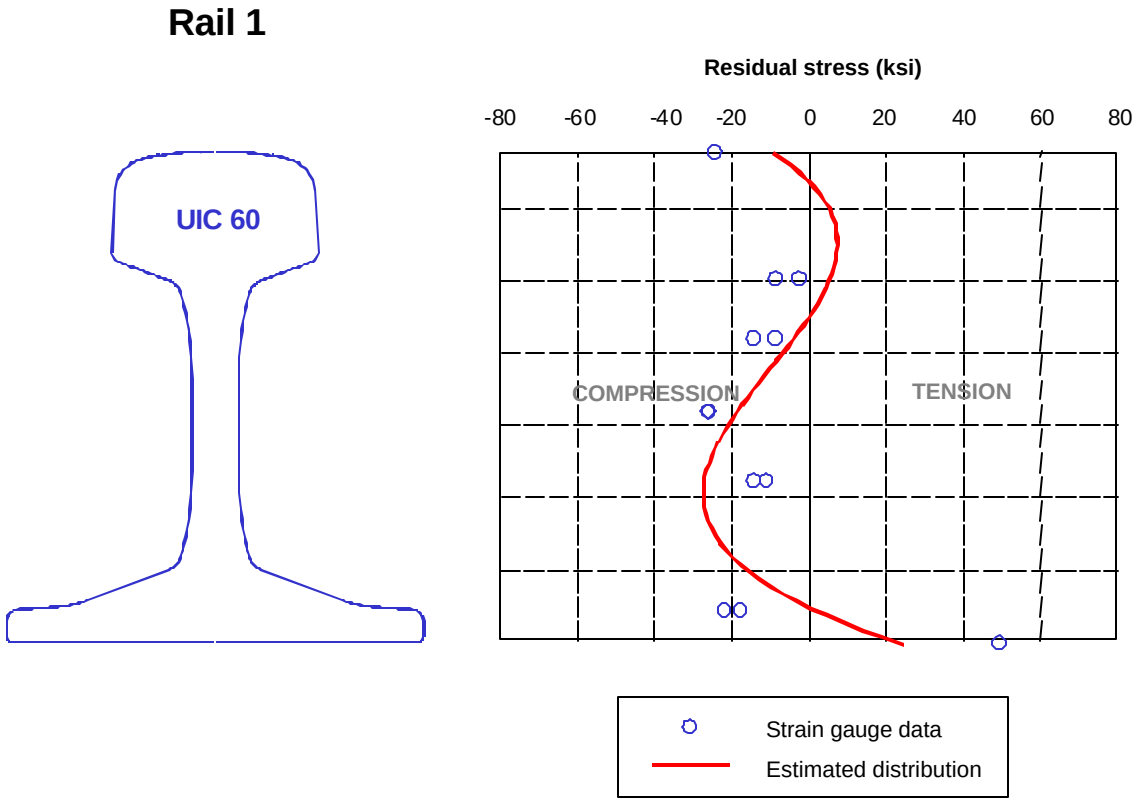

Figure E-21. Reconstruction of longitudinal residual stress distribution for Spoornet Rail 1.

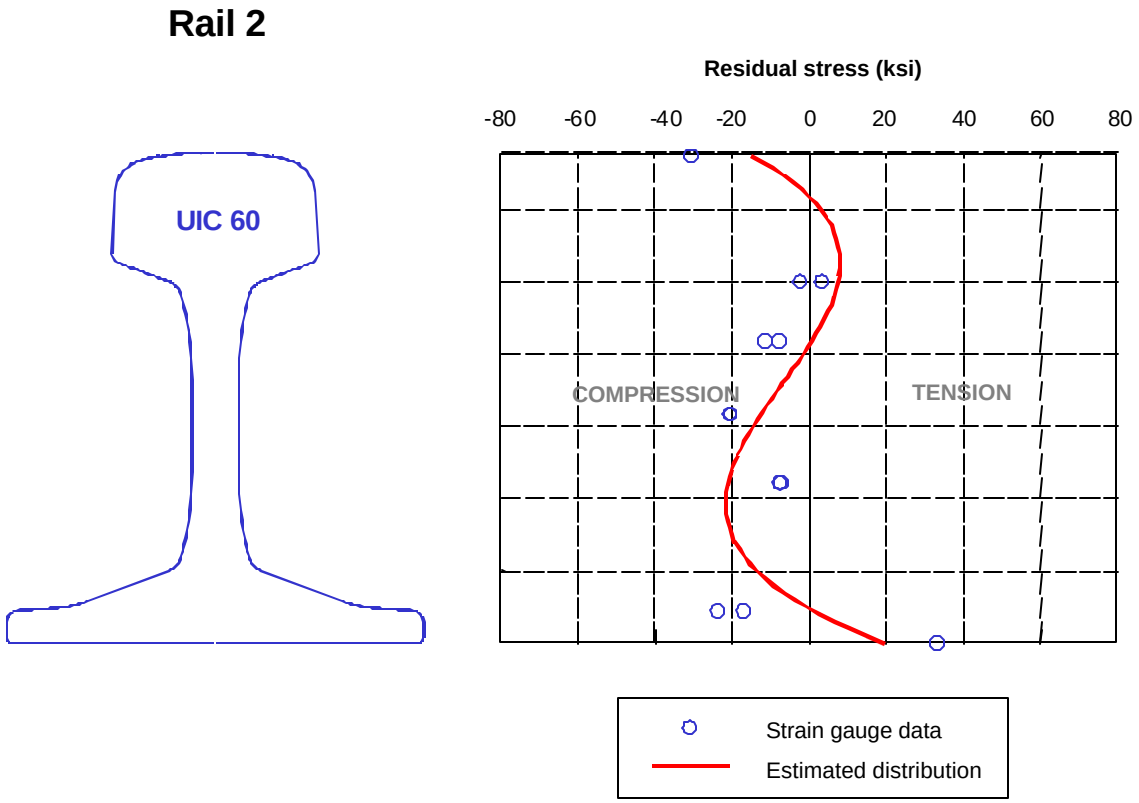

Figure E-22. Reconstruction of longitudinal residual stress distribution for Spoornet Rail 2.

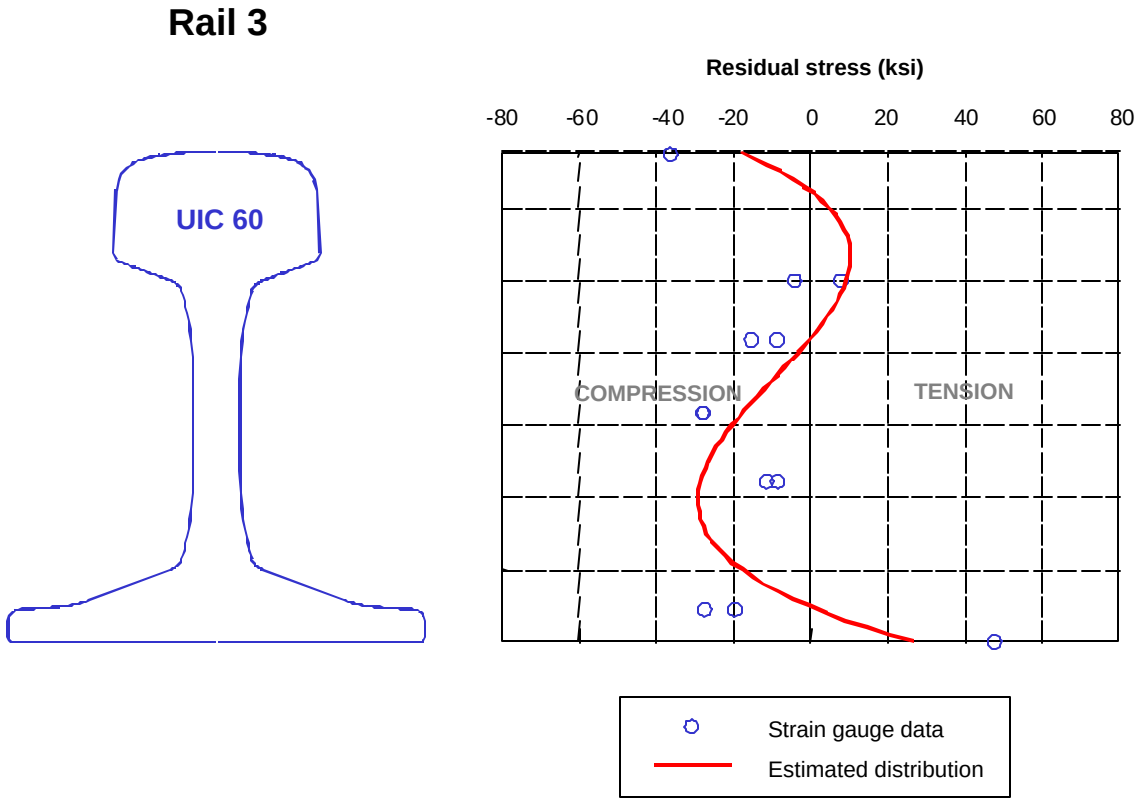

Figure E-23. Reconstruction of longitudinal residual stress distribution for Spoornet Rail 3.